IJBBE International Journal of Biophotonics & Biomedical Engineering Vol. 5, No. 1, Spring- Summer, 2025

Research Article

Computational modeling of M1-BG-Th network firing rate and beta oscillation in brain neurological diseases for treatment with electrical or optogenetic stimulation

Sh. Andalibi Miandoab [a,b*] and N. Ghasemzadeh[c]

a Department of Electrical Engineering, Tabriz Branch, Islamic Azad University, Tabriz, Iran
b Biophotonic Research Center, Tabriz Branch, Islamic Azad University, Tabriz, Iran
c Department of Biomedical Engineering, Tabriz Branch, Islamic Azad University, Tabriz, Iran

***Corresponding Author Email: gnazlar@yahoo.com**

DOI: 10.71498/ijbbe.2025.1191596

ABSTRACT

Received: Nov. 26, 2024, Revised: Feb. 13, 2025, Accepted: Feb. 15, 2025, Available Online: Jul. 14, 2025

The development of computational models is a useful tool for studying the structure and characteristics of brain neurons. By using different modeling methods, the mechanism of neurodegenerative diseases such as Alzheimer's (AD), Epilepsy, and Parkinson's disease (PD) can be understood. Brain disease modeling studies often focus on the Cortex, Thalamus (Th), and Basal Ganglia (BG). The primary motor cortex (M1) has interconnected layers that play an important role in performing movements and treating neurological diseases of the brain. In this paper, we have considered a model of the M1-BG-Th for the neural structure of healthy and Parkinsonian brain neurons. We have investigated excessive oscillations of the beta band and changes in the firing rate of the neurons, which are dynamic characteristics of PD. We have examined characteristics of the firing rate and power spectrum of the neurons of the M1-BG-Th network model, which shows the oscillations of the beta band of neurons of the M1-BG-Th network model, and we have studied healthy and Parkinsonian states. Our aim in presenting the proposed M1-BG-Th model is to investigate optogenetic stimulation for the treatment of neurological diseases of the brain, which is a minimally invasive method and targets specifically selected brain neurons by using opsins.

KEYWORD

M1-BG-Th network model, Parkinson's Disease (PD), Optogenetic, Beta oscillation, Firing Rate (FR).

I. INTRODUCTION

The neurodegenerative disorders of the brain tissue are identified by progressive loss of the set of vulnerable selected neurons. Neurodegenerative diseases can be classified based on their primary clinical features, such as dementia, parkinsonism, or motor neuron disease. Alternatively, they can be categorized according to the anatomical distribution of

neurodegeneration, such as frontotemporal degeneration, extrapyramidal disorders, or spinocerebellar degeneration [1]. Therefore, neurodegenerative disorders can be classified based on their clinical manifestations, among which extrapyramidal movement disorders and cognitive and behavioral disorders are the most common. A small number of patients have pure syndromes, most of them are defined by common features between neurodegenerative diseases, usually by the accumulation of specific proteins and cellular anatomical vulnerability. Neurodegenerative diseases share many of the underlying processes associated with progressive neurological dysfunction and death. The important point is that disorders of the structural proteins are evident even before the onset of the clinical symptoms [1]. Today, diagnostic biomarkers are not available, except in rare cases where a genetic mutation causes the disorder.

Parkinson's disease (PD) is a common neurological disorder marked by a range of motor symptoms, involving bradykinesia, tremor, rigidity, and postural instability [2]. The degeneration of dopaminergic neurons in the substantia nigra pars compacta (SNc) is a key factor in PD, leading to persistent alterations in neuronal firing rates and oscillatory activity among neurons in the Basal Ganglia (BG) [3]. One of the electrophysiological features of PD is the widespread production of synchronized beta band (13-35 Hz) oscillations (β oscillations) in BG [4]. These immoderate and synchronized oscillations affect the ability of the thalamus (Th) to transmit motor information [5]. BG dysfunction is associated with pathogenesis in PD, including changing the firing rate (FR) and excessive synchronized beta-band activity (13–30 Hz). Dopamine loss disrupts the equilibrium between the activation of direct and indirect pathways in the striatum, a critical factor in the progression of PD. These pathways establish the primary connections between the striatum and the deeper structures of the Basal Ganglia (BG). Direct pathway involves the medium spiny neurons (MSNs) in the striatum that express the dopamine D1 receptors (D1 MSNs), along with substantia nigra pars reticulata (SNr) and globus pallidus interna (GPi). In contrast, the indirect pathway consists of MSNs with the dopamine D2 receptors (D2 MSNs), globus pallidus externa (GPe), and the neurons of the subthalamic nucleus (STN).

The primary motor cortex (M1) is a layered structure, with varying morphology, function, and neuronal projections across layers. In healthy conditions, the dynamics of the M1 network are essential for performing complex movements and motor skill acquisition. The neurons that are excitatory in the primary motor cortex (M1) involve the neurons of the intratelencephalic (IT), found in layers 2 through 6, and pyramidal-tract (PT) neurons located in the layer of 5B. These neurons send projections to the striatum and the neurons of the subthalamic nucleus (STN) within the Basal Ganglia (BG), and they also receive feedback from BG and thalamus (Th) [6]. Overall, the primary motor cortex (M1) is essential for movement regulation and plays an important role in the pathophysiology of PD.

Computational network models are valuable tools for investigating pathological brain behaviors and abnormal oscillations. A classical computational model, grounded in the direct/indirect pathway theory, has been developed to explain the mechanisms underlying pathological changes in firing rates. From the perspective of computational modeling, numerous microcircuits within the Basal Ganglia (BG) network are capable of generating beta-band oscillations, which include inhibitory feedback. Among these, the STN-GPe circuit is widely recognized as a key regulator of beta oscillatory activity [7]. Physiological experiments, however, reveal more intricate synaptic connections in the BG, highlighting the complexity of its circuitry. Developing mathematical models provides an effective approach to studying the abnormal synchronized oscillations characteristic of PD [8]. Using these models alongside nonlinear dynamics methods offers insights into the pathogenic mechanisms behind these oscillations [9]. Recent studies on PD modeling have predominantly focused on the cortex, thalamus, and BG. Notably, Terman and Rubin

introduced a computational network model based on BG and thalamocortical (TC) connectivity. So et al. [10] have enhanced this model to offer more precise discharge characteristics for both Parkinsonian and healthy states. This model is frequently used to explore the mechanisms and treatments of Parkinson's disease (PD), although it does not account for the role of the intrinsic network of the striatum. Numerous biophysical studies have shown that the striatum plays a crucial role in Parkinsonian movement and that prolonged dopamine depletion results in significant changes to striatal synaptic plasticity.

Despite its importance in PD, the role of the striatum is often underestimated. Yu and Wang Meaning that most individuals with PD are not candidates for the treatment. So, there is an urgent need to develop more effective and accessible treatments for PD. In this study, we have considered the M1-BG-Th model for the neural structure of healthy and diseased (PD) brain neurons, which has BG neurons including STN, GPe, GPi, Th and M1 neurons including E23, E5A, E5P, and E5B. For the network model of the M1-BG-Th, we have examined characteristics of the firing rate of the neurons and the neurons' power spectrum (PS) indicating the oscillations of the beta band of neurons.

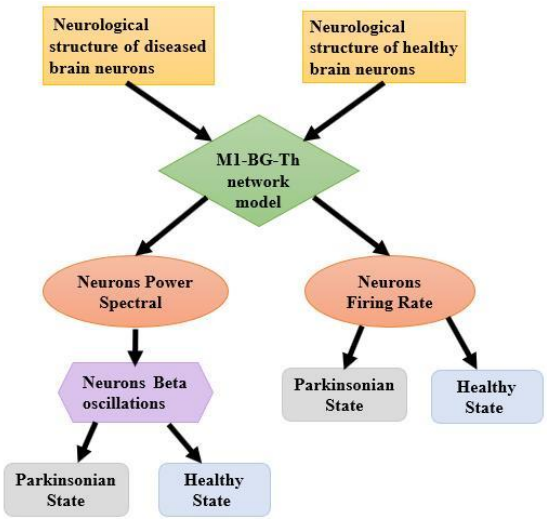

Fig. **1** The block diagram of the research method.

In each of the mentioned characteristics, we have studied healthy and Parkinsonian states. in 2019 [5], investigated the increase of the beta band oscillations in the BGTC model. Yu et al. in 2022 [4], have investigated beta activity in a computational model for GPe circuits. Wang et al. in 2023 [3], studied the dynamic mechanism of the Parkinsonian beta oscillations in the STN-GPe network. The main treatments for PD involve dopaminergic medications and deep brain stimulation (DBS). However, the effectiveness of these drugs tends to diminish over time, often accompanied by a range of side effects. In contrast, DBS is an invasive procedure that requires electrodes implanted to stimulate the deep brain regions. This option is reserved for patients who meet specific criteria,

The block diagram of the research method is shown in Fig.1.We have depicted firing rates of the STN, the GPe, the GPi, the E23, the E5A, and the E5P neurons for healthy and Parkinsonian modes, which based on the obtained results, in healthy the STN, GPe and GPi cells show an irregular discharge pattern. In the healthy state, M1 neurons fire in a random and sparse discharge pattern. In the Parkinsonian state, the GPi fires in a spiking firing pattern, GPe fires with a regular firing pattern, and an increase in STN, E23, E5A, and E5P firing rates is observed. Based on the results of the PS of the cells that show the beta oscillations, for all neurons, the healthy state has lower beta band oscillations and is at the bottom of the graph, while for the Parkinsonian state, the beta band oscillations are higher and there are significant peaks. Finally, we have calculated the average firing rate (AFR) of neurons in the M1-BG-Th network model for both healthy and Parkinsonian modes. In the Parkinsonian state, the AFR is elevated for all neurons, except for those in the GPi. This study effectively illustrates the characteristics and differences between healthy and Parkinsonian conditions using the M1-BG-Th network model.

Ⅱ. METHODS

A. *M1-BG-Th model*

This model is based on the work of Neymotin et al., developed in 2023 [11]. It describes the dynamics of the membrane potential of the Basal Ganglia (BG) and M1 neurons using the Hodgkin-Huxley (HH) framework. The model includes BG neurons such as the subthalamic nucleus (STN), globus pallidus externa (GPe), globus pallidus interna (GPi), and thalamus (Th), as well as M1 neurons like the E23 (the neurons of the intratelencephalic (IT) in the layer of 2), the E5A (the neurons of the IT in the layer of 5A), the E5B (the neurons of the IT in the layer of 5B), and the E5P (the neurons of the pyramidal tract (PT) in the layer of 5B). Additionally, the model incorporates two types of striatal neurons: The D1 medium spiny neurons (MSNs), and the D2 MSNs. Figures 2a and b depict the M1-BG-Th network model, and its connections, with excitatory Equation (1) and for E5P neurons by equation (2):

$$C_m \frac{dV}{dt} = -I_L - I_{Na} - I_K - I_M \quad (1)$$

$$C_m \frac{dV}{dt} = -I_L - I_{Na} - I_K - I_M - I_{Ca} \quad (2)$$

BG-Th model includes STN, GPe, Gpi, Th, and two types of MSN neurons D1 and D2 MSN. For D1 and D2 membrane potential dynamics, the current of the fast potassium (I_k), the current of the sodium (I_{Na}), the current of the leakage (I_L), the current of the M (I_M), and synaptic currents are considered. The membrane potential is described by equation (3) [12].

$$C_m \frac{dV_{MSN}}{dt} = -I_L - I_{Na} - I_K - I_M - I_{E5A\,/\,E5P-MSN} - I_{MSN-MSN} \quad (3)$$

Membrane dynamics of the STN, GPe, and GPi cells have been modeled using the framework presented by Terman and Rubin [13]. The equations of the specific dynamic are outlined in relations (4), (5), and (6)

$$C_m \frac{dV_{STN}}{dt} = -I_L - I_{Na} - I_K - I_T - I_{Ca} - I_{AHP} - I_{GPe-STN} - I_{ESP-STN} \quad (4)$$

$$C_m \frac{dV_{GPe}}{dt} = -I_L - I_{Na} - I_K - I_T - I_{Ca} - I_{AHP} - I_{STN-GPe} - I_{GPe-GPe} - I_{D2-GPe} \quad (5)$$

connections shown by, and inhibitory connections represented by .⊣. Based on Fig. 2b, each Th neuron inhibits one of the M1 neurons (E23, E5A, E5P, and E5B). Each E5P neuron excites three D2 MSN neurons and three STN neurons, and each E5A neuron excites three D1 MSN neurons. Each D1 MSN neuron inhibits two of its neurons and three of the GPi neurons, and each D2 MSN neuron inhibits two of its neurons and four of the GPe neurons. Each of the STN neurons excites two of the GPe neurons and two of the GPi neurons. Each of the neurons of the GPe inhibits two of its neurons, two of the neurons of the STN, and two of the neurons of the GPi. Finally, each GPi neuron sends an inhibitory input to each of the Th neurons. The membrane potential dynamics for E23, E5A, and E5B neurons are modeled by

$$C_m \frac{dV_{GPi}}{dt} = -I_L - I_{Na} - I_K - I_T - I_{Ca} - I_{AHP} - I_{STN-GPi} - I_{GPe-GPi} - I_{D1-GPi} \quad (6)$$

For Th neurons, membrane potentials are expressed by equation (7):

$$C_m \frac{dV_{Th}}{dt} = -I_L - I_{Na} - I_K - I_T - I_{CPi-Th} \quad (7)$$

B. *Different states of M1-BG-Th model healthy and PD states*

Neurological brain diseases lead to an imbalance between the activity of neurons in the direct and indirect paths. Disturbance and change in the mechanism of neurons in the direct and indirect paths lead to abnormal function in the network model of the M1-BG-Th due to the creation of pathological activities of neurological brain diseases. One of the characteristics of pathological activities is the change in the firing rate of the M1-BG-Th model neurons. The firing rate of neurons, which indicates how neurons work, will be different in healthy and PD states. In this way, M1-BGTh model neurons in a healthy state can show an irregular and random firing pattern, while in a PD state, their firing can be regular, increasing, or decreasing [2, 3].

C. *Evaluation of the M1-BG-Th network model function*

In this section, to evaluate the performance of the M1-BG-Th network model, we have calculated the AFR of the neuron population and beta oscillations by calculating the PS of the neurons. AFR is defined as the average firing rate of all the neurons within a population. We have calculated AFR in the form of equation (8) [14] and used it for the network model of the M1-BG-Th neurons, which is a suitable concept for statistical explanation and measurement of nerve spike activity.

$$AFR(t) = \frac{1}{\Delta t} \frac{n_{act}(t;t+\Delta t)}{N} \quad (8)$$

Where N is the population size of the $n_{act}(t; t + \Delta t)$is number of the spikes occurring between t nd $+\Delta t$, and ΔtIs a small-time interval. A high level of AFR indicates a faster firing rate and neural excitation, and a low level of AFR indicates a slower firing rate and inhibition of neural activity. The power spectrum of a train of spikes is a key measure for investigating neural variability, and its calculation is a key challenge for investigating neural firing variability. In practice, the power spectrum is calculated from an averaging process [15]. The power spectrum of neurons reveals key characteristics of their activity. Neurons exhibit various peaks in their responses, with the shape and location of these peaks being influenced by factors like the applied stimuli and the intrinsic biophysical properties, like the input current density and the channel noise. Estimating the power spectrum of neuronal activity is a useful approach for analyzing neural outputs, commonly applied in neurophysiological recordings like the multiunit activity (MUA), the single spike trains, and potentials of the cell membrane. It is also utilized in the outputs of

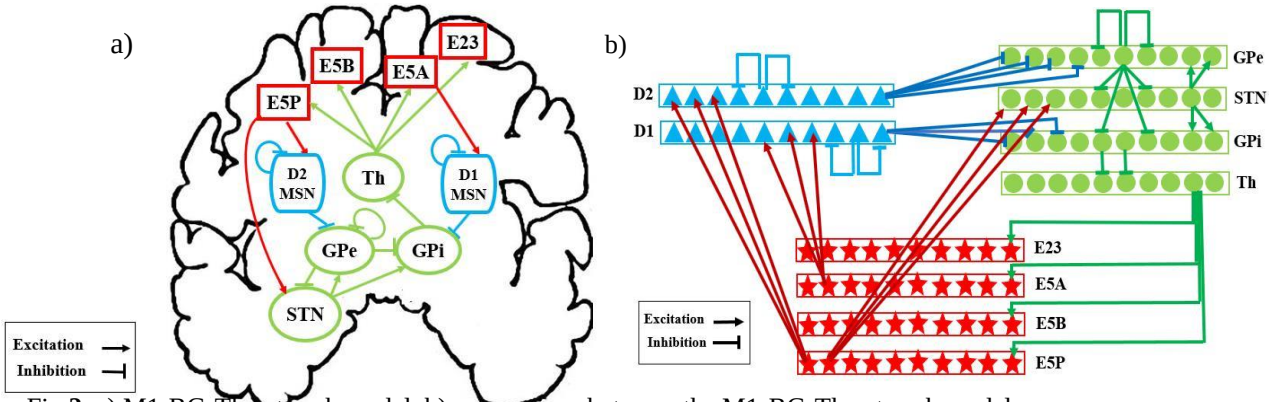

Fig.**2** a) M1-BG-Th network model. b) connections between the M1-BG-Th network model neurons.

Various neural models to assess the neuron's response to input stimuli and for spectral analysis of the experimental recordings from the neurons of the GP in PD patients [16]. In this study, we have calculated the power spectrum to investigate the beta oscillations of the neurons of the M1-BG-Th network model, which is another characteristic of Parkinson's disease. Neurological brain diseases such as PD lead to an increase in beta oscillations and neuron synchrony caused by changes in the strength of synaptic connections of neurons and input currents from different parts of the brain to the neurons of the network model of the M1-BG-Th. Beta oscillations and synchrony of neurons are another characteristic of Parkinson's disease, which shows different physiological and pathological conditions. Synchronized and excessive oscillations of M1-BG-Th network model neurons disrupt the performance of network model neurons in the ability to transmit motor information [4, 5]. In this study, we have obtained the power spectrum to examine the beta oscillations of the M1- BG-Th, which is another feature of the PD.

Ⅲ.Results

Since excitatory input is applied to M1 neurons in the direct and indirect brain path through Th neurons, in this paper, unlike Yu et al. (2023), we have examined the complete model of the M1-BG-Th while considering the connections between Th and M1 neurons. On the other hand, since inhibitory and excitatory connections between neurons and the number of connections between them are important in the function of the M1-BG-Th network model and play an important role in examining characteristics of healthy and parkinsonian states, we have also applied them in M1-BG - Th model. To investigate the treatment of PD with electrical and optogenetic stimulations, we have studied the firing rate of neurons and the beta oscillations of the neurons without applying stimulation for the M1-BG-Th network model. Yu et al., have done the simulation in Neuron software, whereas, we have implemented all the simulation steps with MATLAB software to access the parameters and data of neurons of the M1-BG-Th network model.

A. Firing characteristics of the neurons of the M1-BG-Th model in healthy and PD states

Neuronal firing characteristics play a crucial role in understanding neurological disorders, especially Parkinson's disease (PD). The M1-BG-Th network model consists of neurons of the STN, GPe, GPi, E23, E5A and E5P. The changes in firing rates and patterns between the healthy and PD states significantly impact motor control and are key indicators of dysfunction in the motor circuitry. In the healthy state (Fig. 3a), the M1 neurons (E23, E5A, and E5P) exhibit a random and sparse discharge pattern, while BG neurons (STN, GPe, and GPi) fire irregularly and asynchronously. This firing behavior ensures a balanced inhibitory-excitatory interaction in the M1-BG-Th network, leading to normal motor function. GPi neurons provide appropriate inhibitory input to Th neurons, preventing.

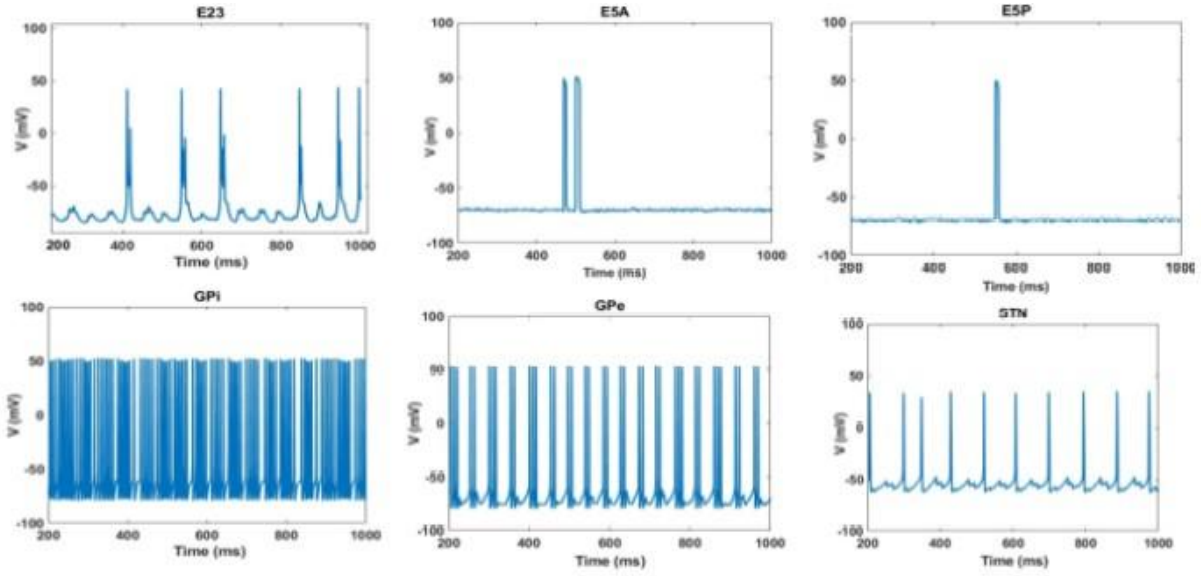

a)

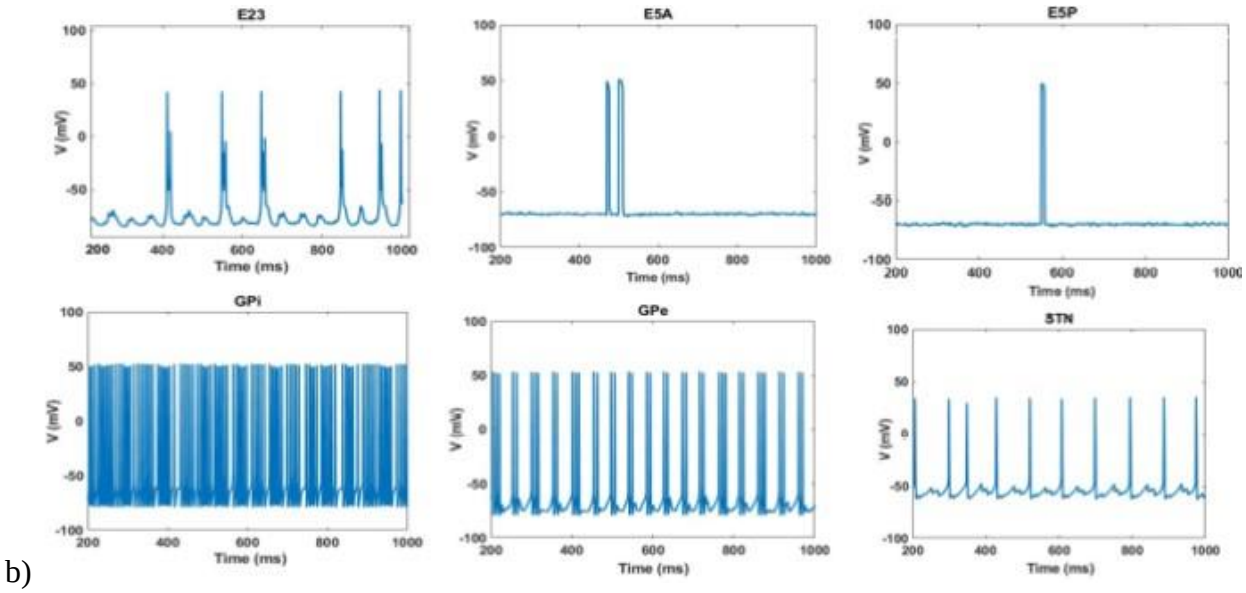

b)

Fig.**3** Firing rate of the M1-BG-Th network model neurons. a) healthy state. b) PD state.

Excessive excitation. The neurons relay proper excitatory input to M1 neurons, maintaining normal motor activity. STN and GPe maintain irregular and asynchronous firing, ensuring a dynamic and adaptive motor control system. This normal firing pattern allows the network to function efficiently, preventing abnormal oscillatory activity and motor dysfunction.

In PD (Fig. 3b), there are significant alterations in neuronal firing rates and patterns, leading to pathological activity in the M1-BG-Th network. M1 neurons (E23, E5A, and E5P) show increased firing rates and synchrony. This excessive excitatory activity contributes to the generation of pathological motor commands, Beta oscillations (13–30 Hz) play a crucial role in motor control, and their abnormal enhancement is a hallmark of Parkinson's disease (PD). These oscillations are linked to motor impairments such as rigidity and bradykinesia. To analyze beta oscillatory activity in both healthy and PD states, the Power Spectrum (PS) of key neurons in the M1-BG-Th network (STN, GPe, GPi, and E23) was calculated, with results presented in (Fig. 4). In leading to symptoms like rigidity and tremors. GPi neurons fire in a bursting pattern. This abnormal burst activity results in excessive inhibition of the Th neurons, disrupting the normal relay of excitatory signals to M1. GPe neurons fire more regularly, reducing their ability to regulate STN activity. This change weakens the indirect pathway, leading to excessive excitatory input from STN to GPi. STN neurons show increased discharge frequency, leading to stronger excitatory input to GPi, which further exacerbates the excessive inhibition of Th.

B. Beta oscillations of the M1-BG-Th model in healthy and PD states

the healthy state, beta oscillations in the M1-BG-Th network exhibit a broad and unstructured spectral distribution without distinct peaks. This absence of prominent beta activity suggests that: STN, GPe, and GPi neurons do not show excessive synchronization, allowing smooth motor execution. E23 neurons in M1 display low amplitude beta activity (PS range: 0–30), which is within normal physiological limits. The lack

of dominant beta rhythms reflects the ability of the network to flexibly modulate motor commands without excessive inhibition or excitation.

In the Parkinsonian state, the M1-BG-Th network exhibits abnormally strong and synchronized beta oscillations, characterized by distinct peaks in the PS of STN, GPe, GPi, and E23 neurons (Fig. 4). The key changes include: STN, GPe, and GPi neurons show enhanced beta peaks, indicating increased synchronization within the basal ganglia. GPi neurons exhibit strong beta-band activity, leading to excessive inhibition of the thalamus, which disrupts normal motor output. E23 neurons in M1 also show increased beta oscillations, though within a lower PS range (0–30). This suggests that cortical activity is influenced by abnormal basal ganglia rhythms, contributing to impaired voluntary movement. The increase in beta oscillations in PD is primarily due to the dysfunction of the cortico-basal ganglia-thalamic loop, which results in excessive excitation of the STN due to reduced GPe inhibition, leading to enhanced beta-band activity in STN and GPi. Overactive GPi neurons impose excessive inhibition on the thalamus, reducing excitatory output to M1. M1 neurons (E23) adopt the abnormal beta rhythm, reinforcing pathological oscillations and contributing to motor deficits such as bradykinesia and rigidity. Clinical Implications of Beta Oscillations in PD Increased beta synchronization is associated with movement difficulties, as excessive beta oscillations reduce the flexibility of motor control.

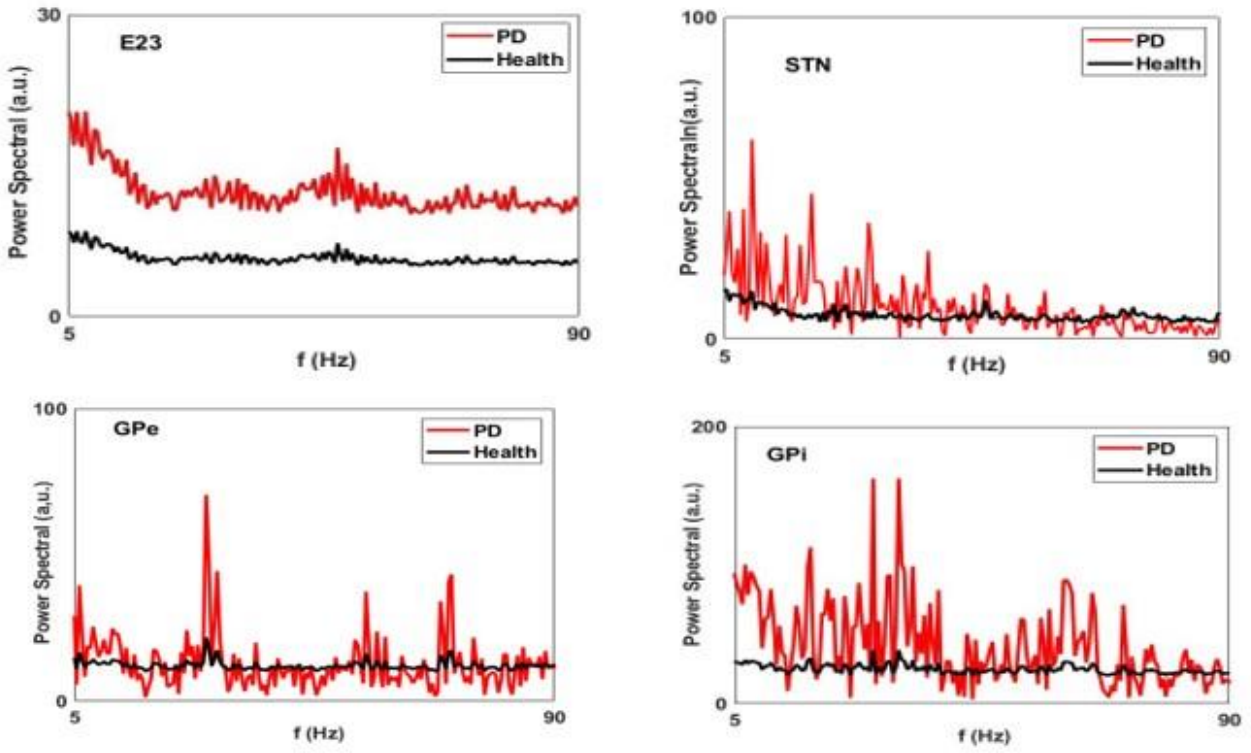

Fig.4 Beta oscillations of the E23, STN, GPe, and GPi for healthy and PD states.

C. AFR of the M1-BG-Th model in healthy and PD states

The Average Firing Rate (AFR) represents the number of spikes generated by neurons in a given period, providing insights into network activity in both healthy and Parkinsonian (PD) states. By analyzing AFR in different neurons of the M1-BG-Th network model, we can understand how PD alters neural dynamics. The

results of this analysis are presented in Table 1. In the healthy state, the AFR of neurons in the M1-BG-Th network follows a balanced pattern, ensuring proper motor function. M1 neurons (E23, E5A, E5P) fire at a moderate rate, supporting controlled and flexible movement.BG neurons (STN, GPe, GPi) maintain normal activity, contributing to the proper regulation of thalamic output. GPi neurons provide appropriate inhibitory control over Th neurons, allowing the thalamus to deliver proper excitatory input to M1. This balanced AFR distribution ensures smooth motor control, preventing excessive or deficient neural excitation.

Table. 1 AFR of the M1-BG-Th network model neurons in healthy and PD states

M1-BG-Th network model neurons	AFR of the healthy state	AFR of the PD state
STN	100	180
GPe	390	490
GPi	1030	980
E23	60	230
E5A	20	80
E5P	10	40

In PD, AFR increases for all neurons except GPi, leading to network dysfunction. STN neurons show increased AFR, resulting in excessive excitatory input to GPi, disrupting normal inhibitory control. GPe neurons fire at a higher rate, reducing their ability to regulate STN activity, and further amplifying STN overactivity. M1 neurons (E23, E5A, E5P) exhibit increased AFR, contributing to abnormal motor commands and pathological activity. GPi neurons exhibit reduced AFR (inhibitory state), impairing their ability to suppress Th neurons effectively. The neurons receive insufficient inhibition from GPi, leading to a failure in delivering appropriate excitatory input to M1. This abnormal AFR distribution disrupts motor signal processing, resulting in increased beta oscillations, excessive synchronization, and the hallmark motor symptoms of PD (tremors, rigidity, and bradykinesia).

Ⅳ. CONCLUSION

Neurological brain diseases lead to disturbances in the function of the brain's neural network. In this study, the M1-BG-Th network model including BG neurons (STN, GPe, and GPi), Th neurons, and M1 neurons (E23, E5A, E5P, and E5B) for healthy and diseased (PD) brain neurons is considered. Since the firing rate of network neurons and beta oscillations are important parameters for network model of the M1-BG-Th network model, we have examined both parameters for healthy and Parkinsonian states and finally, we have obtained AFR for the neurons of the network model of the M1-BG-Th. Based on the obtained results, in the healthy state, BG neurons fire irregularly and M1 neurons fire randomly and sparsely. In the PD state, the firing of BG neurons is bursting, regular, and incremental. Also, this fire increase is observed for M1 neurons. Fewer beta oscillations are seen in the healthy state, but for the PD state, these oscillations have been increased and have distinct peaks. On the other hand, the AFR in the Parkinsonian state is raised for all the neurons except GPi, which leads to disruption in the performance of the M1-BG-Th network and creates pathological activities. Therefore, our proposed model has been able to show the abnormal characteristics of neurodegenerative diseases. Which paves the way for the treatment of neurological brain diseases with electrical and optogenetic stimulations.

REFERENCES

[1] Dugger BN, Dickson DW. Pathology of Neurodegenerative Diseases. Cold Spring Harb Perspect Biol. 2017 Jul 5;9(7): a028035. doi: 10.1101/cshperspect. a028035. PMID: 28062563; PMCID: PMC5495060.

[2] Yu Y, Fan Y, Hou S, Wang Q. Optogenetic stimulation of primary motor cortex regulates beta oscillations in the basal ganglia: A Computational study. Communications in Nonlinear Science and Numerical Simulation. 2023 Feb 1; 117:106918.

[3] Wang X, Yu Y, Han F, Wang Q. Dynamical mechanism of parkinsonian beta oscillation in a heterogenous subthalamopallidal network. Nonlinear Dynamics. 2023 Jun;111(11):10505-27.

[4] Wang X, Yu Y, Han F, Wang Q. Beta-band bursting activity in computational model of heterogeneous external globus pallidus circuits. Communications in Nonlinear Science and Numerical Simulation. 2022 Jul 1; 110:106388.

[5] Yu Y, Wang Q. Oscillation dynamics in an extended model of thalamic-basal ganglia. Nonlinear Dynamics. 2019 Oct;98(2):1065-80.

[6] Lee J, Wang W, Sabatini BL. Anatomically segregated basal ganglia pathways allow parallel behavioral modulation. Nature neuroscience. 2020 Nov;23(11):1388-98.

[7] Terman, D., Rubin, J.E., Yew, A.C., Wilson, C.J.: Activity patterns in a model for the subthalamopallidal network of the basal ganglia. J. Neurosci. 22, 2963–2976 (2002).

[8] Rubin, J. E., & Terman, D. (2004). High frequency stimulation of the subthalamic nucleus eliminates pathological thalamic rhythmicity in a computational model. Journal of Computational Neuroscience, 16(3), 211–235. http://dx.doi. org/10.1023/B: JCNS.0000025686.47117.67.

[9] Yu Y, Hao Y, Wang Q. Model-based optimized phase-deviation deep brain stimulation for Parkinson's disease. Neural networks. 2020 Feb 1; 122:308-19.

[10] Seeley WW, Crawford RK, Zhou J, Miller BL, Greicius MD. Neurodegenerative diseases target large-scale human brain networks. Neuron. 2009 Apr 16;62(1):42-52.

[11] Neymotin SA, Dura-Bernal S, Lakatos P, Sanger TD, Lytton WW. Multitarget multiscale simulation for pharmacological treatment of dystonia in motor cortex. Frontiers in Pharmacology. 2016 Jun 14; 7:157.

[12] Terman D, Rubin JE, Yew AC, Wilson CJ. Activity patterns in a model for the subthalamopallidal network of the basal ganglia. Journal of Neuroscience. 2002 Apr 1;22(7):2963-76.

[13] So RQ, Kent AR, Grill WM. Relative contributions of local cell and passing fiber activation and silencing to changes in thalamic fidelity during deep brain stimulation and lesioning: a computational modeling study. Journal of computational neuroscience. 2012 Jun;32(3):499-519.

[14] Yu Y, Fan Y, Hou S, Wang Q. Optogenetic stimulation of primary motor cortex regulates beta oscillations in the basal ganglia: A Computational study. Communications in Nonlinear Science and Numerical Simulation. 2023 Feb 1; 117:106918. http://dx.doi.org/10.1016/j.cnsns.2022.106918.

[15] Vilela M, Halidi N, Besson S, Elliott H, Hahn K, Tytell J, Danuser G. Fluctuation analysis of activity biosensor images for the study of information flow in signaling pathways. InMethods in enzymology 2013 Jan 1 (Vol. 519, pp. 253-276). Academic Press.

[16] Orcioni S, Paffi A, Apollonio F, Liberti M. Revealing spectrum features of stochastic neuron spike trains. Mathematics. 2020 Jun 20;8(6):101

.

IJBBE International Journal of Biophotonics & Biomedical Engineering Vol. 5, No. 1, Spring-Summer , 2025

Research Article

A New Method in Improving the Accuracy of Fetal Brain Health Diagnosis Based on Analysis of Constrictors Feature in Ultrasound Images

S. Surani[a] and M. Emadi[b,*]

a Master Student, Department of Bioelectric Engineering, Ragheb Isfahani, Institute of Higher Education, Isfahan, Iran
b Department of Electrical Engineering, Mo.C., Islamic Azad University, Isfahan, Iran

*** Corresponding Author Email: mehranemadi49@iau.ac.ir**

DOI:10.71498/ijbbe.2025.1195960

ABSTRACT

Received: Jan. 09, 2025, Revised: Apr. 23, 2025, Accepted: May 10, 2025, Available Online: Jul. 14, 2025

Fetal growth is a critical stage in prenatal care that requires the timely identification of abnormalities in ultrasound images to protect the health of the fetus and mother. Ultrasound-based imaging has played an essential role in diagnosing fetal malformations and abnormalities. Despite significant advances in ultrasound technology, detecting abnormalities in prenatal images still poses considerable challenges. These challenges often arise from time constraints and the need for substantial expertise from medical professionals. The aim is to classify several K classes of random forest support vector machine (SVM) and use this for evaluation. The aim is to perform a multi-class classification of 3 health stages, including healthy, suspicious, and diseased brain. Methods based on machine learning are among the methods that help experts. In this research, a machine learning method based on image scattering features is presented for the classification of fetal brain ultrasound images. In the proposed method, after integration, which is based on the maximum integration rule in scattered features, and discrete wavelet and cosine transform, a method based on the mutual information is presented for feature selection. The selected features have been used to diagnose the health status of the fetus with the help of the nearest neighbor. The evaluation criteria of accuracy, recall rate, accuracy and F criterion have been used for evaluation. The support vector machine classifier has shown its superiority in comparison with other classifiers with 98% accuracy, 97% accuracy, 99% recall rate, and F-criterion more than 98%. The comparison of the results obtained in the diagnosis of the health status of the fetus compared to other methods shows the superiority of the proposed method.

KEYWORDS

Improvement, Diagnosis, Fetal Brain Health, Ultrasound Images, Scattered Transform, Discrete Wavelet Transform.

I. INTRODUCTION

Pregnancy is a significant and joyous phase in a woman's life that necessitates careful attention to maternal health. As a comprehensive assessment of fetal health prior to birth, it is essential for effective monitoring and outcomes. The fetus is dependent on the

mother in terms of the exchange of oxygen and carbon dioxide in the placenta, and this, in turn, depends on the sufficient concentration of gases in the mother's blood, the amount of blood in the uterus, the placenta's exchanges, and gas transfer to the fetus. A defect in any of the above factors can lead to a lack of oxygen in the fetal tissues (hypoxia), which, despite the presence of compensatory mechanisms, may cause an abnormal increase in the level of acid in the blood (acidosis) [2].To monitor the growth and development of the fetus, several laboratory tests are suggested every trimester. One of these tests is ultrasound imaging, which is usually used in clinical evaluation to check the health status of the fetus in the womb [3]. The main goal is to monitor or diagnose the possible disease of different parts of the fetus, especially the brain, which can prevent the possible death of the fetus. If there is a system that can predict the future state of the fetus according to the current state, it can prevent problems such as miscarriage or serious injuries [4]. Determining fetal health is a difficult process that depends on various input factors. Depending on the input symptoms, the health status of the fetus is diagnosed. Sometimes it is difficult to determine the diagnosis of diseases, and there may always be differences of opinion between specialist doctors. As a result, the diagnosis of diseases is often performed in uncertain conditions and can sometimes cause undesirable errors. Therefore, the vague nature of diseases and incomplete patient data can lead to uncertain decision-making. One of the effective approaches to solve such a problem is the use of methods based on machine learning and deep learning in the diagnostic system [5]. Machine learning is widely used in studies related to fetal health diagnosis. Traditional machine learning techniques require manual feature extraction before classification. However, for automated analysis of neuron imaging data, manual feature extraction cannot accurately detect fetal brain health [6]. Approaches based on user-defined features in classical machine learning have limitations. Improved performance can be achieved by learning specific features to achieve the desired result. In the traditional machine learning based method, pattern recognition processes are used. In this category of methods, after applying pre-processing on the image, numerous features, including textural, spectral, geometric and statistical features are extracted from the target image. These features are reduced in another step with the help of methods based on principal component analysis PCA, independent component analysis LDA. At this stage, feature selection methods can be used to select the most effective features [7,8]. Methods such as SFFS hierarchical forward feature selection or methods based on information theory, such as maximum correlation and minimum correlation mRMR can be used. Finally, the selected features are classified with the help of classifications such as support vector machine SVM, k-nearest neighbor KNN, and random forest RF. In this category of methods, a learning criterion or clustering methods are used to check the presence of lesions in the images. In the traditional methods of machine learning and pattern recognition, Euclidean, Mahalolunbis, or Shahr Block learning criteria are also used [9]. In the pre-processing, noise removal is done, and it is associated with image quality improvement processes. Feature extraction includes the use of different descriptors to find unique features from each image [10]. The most common descriptors used for feature extraction are transform domain methods such as discrete Fourier transform, discrete wavelet transform, discrete cosine transform, space domain-based methods such as internal and statistical features, and image histogram. Methods based on building information, such as local binary patterns, extracting effective features from images, are an essential step in diagnosing fetal brain health in ultrasound. The extracted features are used to create a one-to-one mapping between the target images. Extracting unique features is very important in creating accurate one-to-one mapping [11]. In the last decade, there have been many tendencies towards feature extraction with scattered representation. Because in this representation, there are almost only a small number of non-zero coefficients, or they have been scattered after applying transformations on the image. This trend seems

to be due to the potential to reconstruct the signal or image from a smaller number of measurements than conventional methods to reconstruct an entire signal. The features extracted in scatter transformations are more unique. One of the significant scatter transforms is the use of wavelet transform. The purpose of wavelet transform is a desirable strategy to establish an optimal balance between time accuracy and frequency accuracy. At higher frequencies, the wavelet transforms gains temporal information at the cost of losing frequency information. While at lower frequencies, it gains frequency information at the expense of temporal information loss. This favorable approach to information exchange is useful for digital signal processing and music applications. Machine learning algorithms can be presented for segmentation and classification of normal and abnormal fetal brain ultrasound images. Through the studies, it was found that although there have been many studies and researches to determine the health of the fetal brain in ultrasound images, there is still a long way to go before reaching a favorable answer in the classification and diagnosis of these images. According to the studies conducted in the review of the research literature and the background of the research, it is clear that the methods based on image scattering transformations such as wavelet transformation and its group can provide effective and suitable features for this work. Based on the presented content, the innovations of this research can be stated as follows:

Using scattering transform based on the wavelet transform to detect fetal brain health stage in ultrasound images.

Using feature selection methods to identify informative data in ultrasound images.

The goal of this study is to implement a classification of multiple K classes using random forest and support vector machine (SVM) methodologies for evaluation. This classification will focus on three health stages: healthy, suspicious, and diseased brain.

II. LITERATUREANDRELATED WORKS

A. Research Background

In [12], a complex neural network (ECNN) model is used, which combines basic models to classify fetal plates using an open-access database containing 12,400 images with six fetal plates. Previous studies on this database included advanced CNN methods, and the pre-trained Densenet-169 model provided an accuracy of 93.6%, which is presented as a deep learning model named FetSAM. The [13], proposed model is an advanced deep learning model, which aims to revolutionize fetal head ultrasound segmentation and thereby increase the accuracy of prenatal diagnosis. In [14], a three-way crossover randomized control method (trial registration: ChiCTR2100048233) reported evaluating the effectiveness of a deep learning system, the Prenatal Ultrasound Diagnosis Artificial Intelligence Behavior System (PAICS), in helping to detect fetal intracranial malformations. In [15], a U-Net fetal head measurement tool is presented, that uses a hybrid dice and binary cross-entropy loss to calculate the similarity between actual and predicted regions. Reference [16] has proposed to use ultrasound images in a deep learning model to automate fetal organ classification. The proposed model has been trained and tested on a dataset of fetal ultrasound images, including two datasets from different regions, and they have been recorded with different machines to ensure the effective detection of fetal organs. In [17], ultrasound images were analyzed using a Dense Net model. The accuracy of the trained model in correctly identifying cystic hygroma cases was evaluated. This evaluation was conducted by calculating sensitivity, specificity, and the area under the receiver operating characteristic (ROC) curve. In [18], to investigate the application of Deep Learning Neural Network (DLNN) algorithms to identify and optimize the ultrasound image to analyze the impact and value in the diagnosis of fetal central nervous system (CNSM) malformation. It was in the diagnosis of ultrasound images (before birth) by

designing and implementing a new framework called Defending Against Child Death (DACD) [19]. The existing method is a semi-automatic method in which the Convolution Neural Network (CNN) algorithm is used to classify ultrasound images. In [20], the maturity of current deep learning classification techniques was evaluated for their application in a real maternal and fetal clinical setting. In [21], has proposed two main methods based on deep convolution neural networks for automatic detection of six standard fetal brain screens. One is a deep convolutional neural network (CNN) and the other is domain transfer learning based on CNN. The suggested methods in diagnosing fetal brain health in ultrasound images have low accuracy. The quality of the classification affects the diagnostic accuracy of the systems because many features, such as shape, aspect ratio, and border smoothness, are related to the contour of the region involved in brain pain. Furthermore, an automatic and real-time classification system may help radiologists identify disease in the fetal brain and provide a signal in case of human error.

B. Scattered Representation Analysis

Scattered representation is a way to reduce natural or artificial observations to their basic components. These signals often have scattered representation in a domain with regard to the place or time in which they usually appear. For tasks such as compression or parsing, it is often more efficient and meaningful to transform a signal into another domain or to find its scattered representation among a collection of basic signals, called atoms, that make up a dictionary. Analytical dictionaries have precise definitions that make them convenient in some situations, but are generally difficult and inefficient. For greater consistency, scattered coding methods were introduced to allow atoms from a mix of different cultures to be selected and added to represent signals [22]. Following this paradigm shift, Olshausen and field were among the first to propose a way to train a dictionary on examples associated with the desired signal [23]. Other algorithms, such as the K-SVD dictionary learning algorithm, are widely used today [24].

C. Discrete Cosine Transform (DCT)

Discrete cosine transform (DCT) represents a signal as a superposition of cosine waveforms with different frequencies. This transform is similar to the Discrete Fourier Transform (DFT) but only deals with real domain numbers. More importantly, DCT is more efficient in representing limited signals. This is because the Fourier Transform implicitly assumes a periodic expansion of a signal, which creates a discontinuity at the boundaries for most signals. Conversely, DCT assumes an anti-symmetric expansion to the signal. This problem leads to creating more sine waves to represent the signal with DFT than with DCT. The two-dimensional DCT transform of a signal x with dimensions M and N is:

$$A(p,q) = \alpha_p \alpha_q \sum_{m=0}^{M-1} \sum_{n=0}^{N-1} x(m,n) \cos\frac{(2m+1)\pi p}{2M} * cos\frac{(2n+1)\pi p}{2N} \begin{matrix} 0 \le p \le M-1 \\ 0 \le q \le N-1 \end{matrix}$$

$$\alpha_p = \begin{cases} 1/\sqrt{M} & p = 0 \\ \sqrt{2/M} & 1 \le p \le M-1 \end{cases} \quad (1)$$

$$\alpha_q = \begin{cases} 1/\sqrt{N} & q = 0 \\ \sqrt{2/N} & 1 \le q \le N-1 \end{cases}$$

The DCT inverse transform is used to reconstruct the signal:

$$x(m,n) = \sum_{p=0}^{M-1} \sum_{q=0}^{N-1} \alpha_p \alpha_q A(p,q) \cos\frac{(2m+1)\pi p}{2M} * cos\frac{(2n+1)\pi q}{2N} \begin{matrix} 0 \le p \le M-1 \\ 0 \le q \le N-1 \end{matrix} \quad (2)$$

In this reconstruction of those basic functions $\alpha_p \alpha_q A(p,q) \cos\frac{(2m+1)\pi p}{2M} cos\frac{(2n+1)\pi q}{2N}$ form a dictionary and by the coefficients if $A(p,q)$. are integers, the number of atoms is equal to the size of the signal ($M \times N$) and the dictionary is orthogonal. Figure 1, shows an orthogonal

dictionary. Because of its simplicity, the orthogonal dictionary has often been used in the past, but relaxing this restriction allows sparse representations of signals.

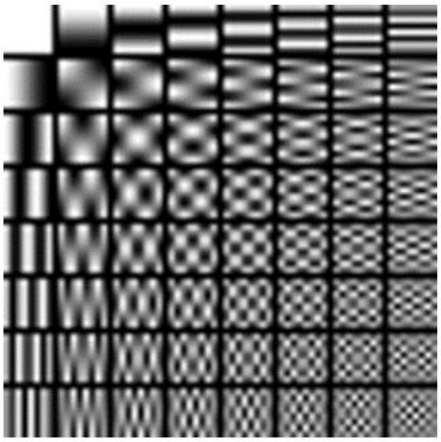

Fig. **1.** Orthogonal DCT dictionary with 64 atoms of size 8x8.

This is achieved by allowing non-integer values for p and q, thereby increasing the number of atoms beyond the size of the signal. An example of such an overcomplete dictionary is shown in Figure 2.

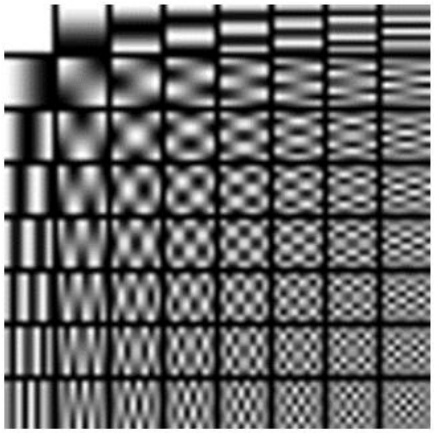

Fig. **2.** Overcomplete DCT dictionary with 256 atoms of 8x8 dimensions.

D. Discrete Cosine Transform

Wavelet transform can be calculated by equation (3):

$$C(a,b) = \frac{1}{\sqrt{a}} \int_{-\infty}^{\infty} f(x)\psi^*\left(\frac{x-b}{a}\right)dx \qquad (3)$$

The ψ basis wavelet is designed to be reversible and computationally efficient. In practice, the translation and scaling parameters are as $a = a_0^m, b = nb_0a_0^m$ as $m, n \in \mathbb{Z}$, $a_0 > 1$, b_0, Disc > 0 are discrete in this case. The wavelet transform (DWT) becomes:

$$C(m,n) = \frac{1}{\sqrt{a_0^m}} \int_{-\infty}^{\infty} f(x)\psi^*\left(\frac{x - nb_0a_0^m}{a_0^m}\right)dx \qquad (4)$$

The signal f can be reconstructed by summing the weighted wavelets:

$$f = \sum_{m,n} c_{m,n} \qquad (5)$$

The following values are usually used: $a0 = 2$, $b0 = 1$. There are ψ options where the set of wavelets $\psi m,n$ form a canonical basis, in which case the wavelets are critically in. Each scale is sampled to accurately capture the newly introduced details. The scale of the simplest such wavelet is the scattering wavelet (Figure 3). Various other wavelets have been designed by Stromberg [25], Meyer [26], Daubeshiz [27] and others.

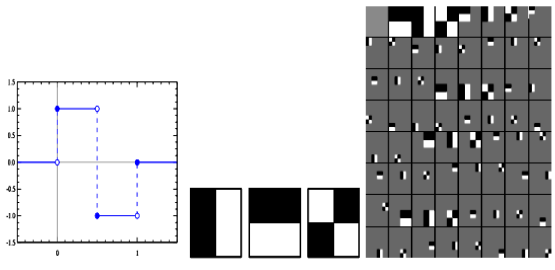

(a) **(b)** **(c)**

Fig. **3.** a: 1D Haar wavelet, b: three configurations of Haar wavelet in 2D. Black color is negative and white is positive, c: Haar orthogonal dictionary consisting of wavelet expansion and translation.

In higher dimensions, the DWT is just a separable one-dimensional transform. So, for an image, first the columns and then the rows are individually transformed in the same way as any 1D signal. This makes DWT translation and rotation sensitive in higher dimensions. To overcome this issue, the Stationary Wavelet Transform (SWT) was introduced by Beylkin [28], which ignores orthogonality in favor of over-completeness. This is achieved by removing subsampling and summing all translations of wavelet atoms.

III. Methodology

The main goal of this research is to diagnose the health of the fetal brain with the help of image scattering features. In this regard, fetal brain ultrasound images should be pre-processed in a standard way. The block diagram of the proposed method is shown in Figure 4. In the following, different parts of the proposed method will be examined.

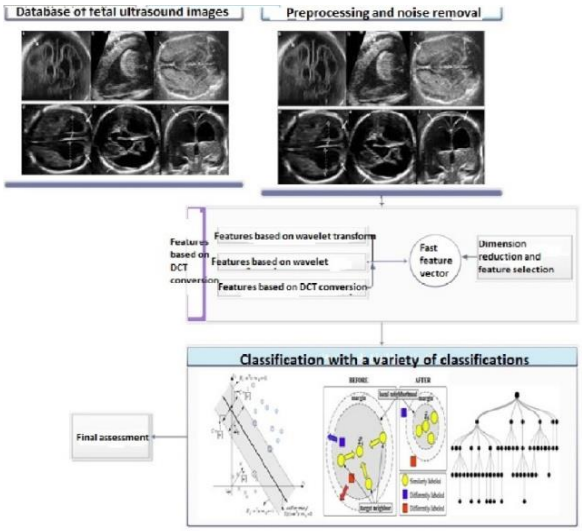

Fig. **4.** The block diagram of the proposed method.

A. Preprocessing

In this paper, a fast algorithm for grayscale images is proposed as an adaptive two-way filter, which is otherwise computationally expensive and complex. This can be extended to color filtering using channel-wise processing. Bidirectional filtering is used as an edge preservation tool in image enhancement applications. Along with a low-pass spatial core (which helps with smooth scattering), it uses a core to prevent smoothing near the edges. As a result, the filter can smooth homogeneous areas and preserve sharp edges at the same time. Gaussian spatial and domain cores were shown to improve the upscaling capacity of the two-way filter by adjusting the width and center of the curved range at each pixel. A two-way filter is shown as equations 6 and 7:

$$g(t) = \eta(i)^{-1} \sum_{J \in \Omega} w(j)\Phi_i(f(i-j) - \theta(i))f(i-j) \quad (6)$$

$$\eta(i) = \sum_{j \in \Omega} w(j)\phi_i(f(i-j) - \theta(i)) \quad (7)$$

In this article, spatial and locative cores will be used in the form of equations 8 and 9:

$$w(j) = \exp\left[-\frac{\|j\|^2}{2\rho^2}\right] \quad (8)$$

$$\Phi_i(t) = \exp\left[-\frac{t^2}{2\sigma^2}\right] \quad (9)$$

In the above equation, $\sigma(i)$, ρ are effective width and bandwidth Gaussian window. In this way, $\Omega = [-3\rho, 3\rho]^2$ unlike the classic bilateral filter, which uses a fixed-amplitude kernel in each pixel, the width σ(i) is allowed to change in each pixel in (8) and (9). In addition, the center of f(i) can be different from f(i) used in the classical two-way filter. Figure 5 shows the improved image with the help of the bilateral filter.

Fig. **5.** An example of the improved image in the filtering method.

B. Scattered Transformers

B.I. Scattered Representation Analysis

The curve transformation, which is a combination of the previous two transformations, allows us to analyze the image with different block sizes. The work process is that first, the image is decomposed into a set of wavelet bands, and the analysis of each band is performed by the Regretted transformation. The size of the blocks can be changed in each level. In fact, it is a two-dimensional transformation that cannot be separated into one-dimensional transformations parallel to the coordinate axes. Curve transformation is presented for optimal representation of two-dimensional discontinuities. In this research, 2 levels of curve transformation are used. Figure 6a shows the feature map of level 1, and Figure 6b shows the feature map of level 2 of the curve transformation. The feature vector obtained from these two levels will be included in the feature vector of each pixel.

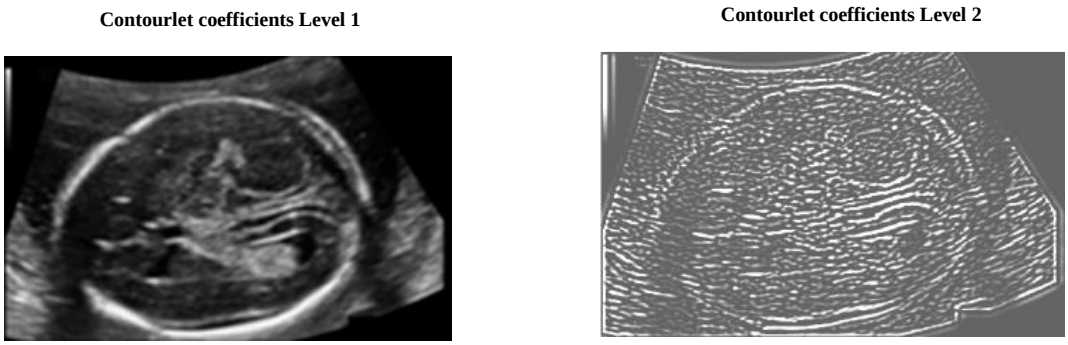

Fig. **6.** Sub-bands created from curve transformation in a: level one, b: level two.

B.II. DCT implementation

The DCT algorithm is a compression and scattering algorithm to extract image scattering features. Due to the slowness of the previous calculation methods in the reviewed articles, at this stage, by applying this algorithm, we increase the processing speed to a great extent. By compressing the image, it scatters the image and reduces the processing load to the program imposes. Figure 7 shows the process of applying the discrete cosine transformation function. Also, Figures 3- 6 show the scattered images by the DCT algorithm.

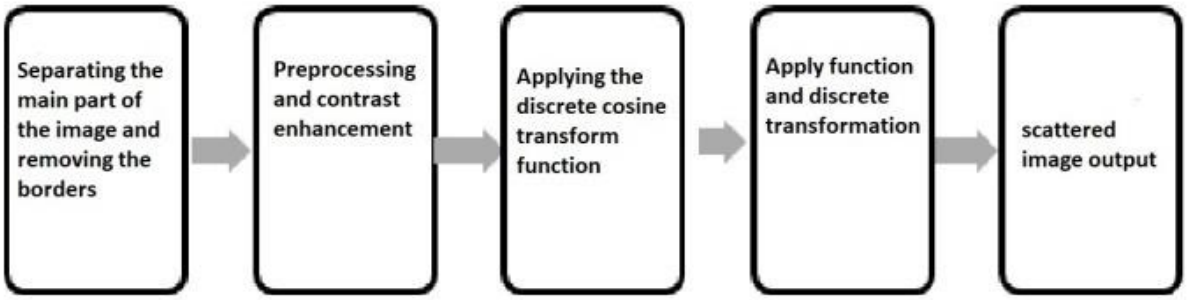

Fig. **7.** The process of applying the discrete cosine transformation function.

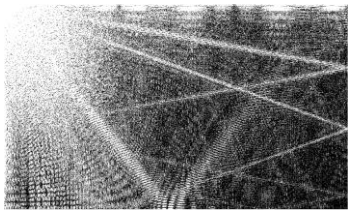

Fig. **8.** Image resulting from the DCT algorithm on the original image.

B.III. Features based on wavelet transform

Figure 9-a shows the wavelet transformation on the image and how to create the sub-image and related filters. Part B shows the division of the image. In this figure, the approximation of the image with A and sub-images, or in other words, the details of the image in high frequencies, H, are vertical details, D are diagonal details, and V are horizontal details in the image. If higher levels of wavelet transformation are needed, this transformation is applied in part a. The edges of the image are visible in the sub-bands obtained from this transformation in such a way that the horizontal, vertical, and diagonal edges are shown in each of the sub-images. If the fabric has damage, the edges in each corresponding sub-band will be shown more clearly. Figure 10 shows the scattered image created from the wavelet transform in different sub-bands.

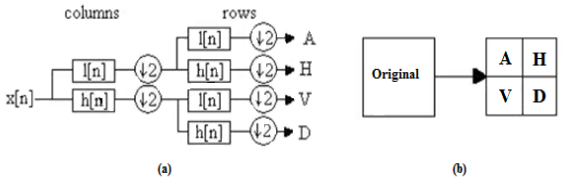

Fig. **9.** Block diagram of wavelet transformation on the image a) bank of filters, b) dividing the image into approximation and detail sub-bands.

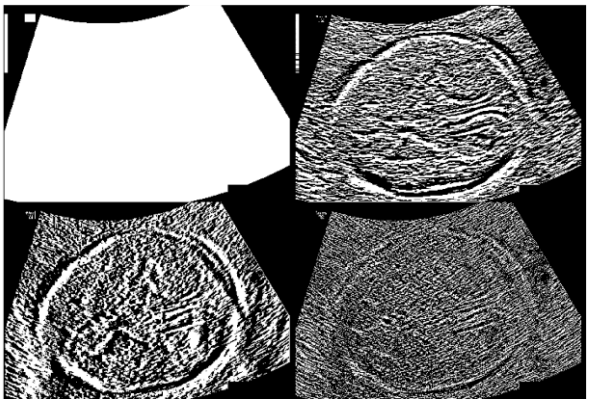

Fig. **10.** Scattered image created by wavelet transform.

C. Feature integration

Three feature maps are created by applying the DCT algorithm, wavelet transform, and curve

scattering transform, and the selection of the best features plays an important role in the final segmentation. Merge rules are used to merge the image at the feature level. The most common rules used for image integration are the selection of maxima, minima, and finally, averaging. The following relationships represent these rules. In this thesis, the proposed method, as well as the other methods, each of which uses the integration law to select the maximum coefficients.

$$Selected_{def} = Max\{CURV_{def}(i.j).DCT_{def}(i.j).DWT_{def}(i.j)\} \quad (10)$$

$$Selected_{def} = Min\{CURV_{def}(i.j).DCT_{def}(i.j).DWT_{def}(i.j)\} \quad (11)$$

$$Selected_{def} = Avg\{CURV_{def}(i.j).DCT_{def}(i.j).DWT_{def}(i.j)\} \quad (12)$$

n the above equation, $Selected_{def}$is the output image after selecting the area in thefeature map. $CURV_{def}(i.j)$ represents the feature map resulting from curve transformation. $DCT_{def}(i.j)$ represents the map obtained from the DCT thinning transform and at the end, $DWT_{def}(i.j)$ is discrete wavelet of transform feature map. Min، $Max$and Avg indicate the selection of minimum, maximum, and average, respectively. Max is used in this research.

D. Feature integration

Evaluation criteria play a decisive role in the feature selection. In other words, these criteria are the basis of feature selection. The selection of an optimal subset of the feature set directly depends on the appropriate selection of the evaluation criteria. In a way that, if any evaluation criterion assigns an inappropriate value to the subset of optimal features, this subset is never selected as the optimal subset. The values that different evaluation criteria give to a subset are different. In the concept of classification and its related issues, an optimal criterion must have a Bayesian error rate. E(S) is calculated from equation 13. Equation 14 is also used in discrete space [29].

$$E(s) = \int_S \mathrm{P}(s)(1-\max_i(\mathrm{P}(c_i \mid S)))ds \quad (13)$$

$$or \ \sum_S (1-\max(\mathrm{P}(c_i \mid S))) \quad (14)$$

As can be seen from equations 13 and 14, E(S) is desired as a sum or integral and is also non-linear and non-negative. In equation 15, the upper bound of E(S) is calculated, $H(C|S)$ the conditional entropy C in each S is given.

$$E(s) \le \frac{H(C \mid S)}{2} \quad (15)$$

Calculating E(S) directly is very difficult because S is a combination of features. As a result, most researchers prefer to use criteria based on correlation and distance. Equation 16, shows the evaluation criterion of the correlation coefficient. The covariance of the variables a and b is the variance.

$$r(a,b) = \frac{\mathrm{cov}(a,b)}{\sqrt{\mathrm{var}(a)}\sqrt{\mathrm{var}(b)}} \quad (16)$$

Pearson's correlation coefficient is calculated in equation 17.

$$r(a,b) = \frac{N\sum a_i b_i - \sum a_i \sum b_i}{\sqrt{N\sum a_i^2 - (\sum a_i)^2}\sqrt{N\sum b_i^2 - (\sum b_i)^2}} \quad (17)$$

Mutual Information (MI) is obtained from equation 18. $p(0)$ is Probability Density Function (PDF).

$$I(a,b) = \sum_a \sum_b p(ab)\log\frac{p(ab)}{p(a)p(b)} \quad (18)$$

Equation19, illustrates symmetric uncertainty (SU). H (0) is the entropy of each feature.

$$SU(a,b) = \frac{2I(a;b)}{H(a)+H(b)} \quad (19)$$

Distance information is calculated in equation 20. H(a|b) is the conditional entropy a in term b.

$$d(a,b) = \frac{H(a|b)+H(b|a)}{2} \quad (20)$$

Finally, the last criterion, which is very common for evaluation, is calculated from

equation 21, and it is the Euclidean distance criterion.

$$d(a,b)=\sqrt{\sum(a_i-b_i)^2} \quad (21)$$

These common criteria are used to evaluate feature selection methods. Although there are other criteria, such as Laplacian score, Fisher Score [30], and other criteria, information criteria require features in a discrete state, and discretization is required if they are used [31].

E. Classification

For the experiment, three different machine learning algorithms were used together: support vector machine (SVM), K-nearest neighbors (KNN), ensemble method, and random forest (RF).

SVM is a statistically supervised learning algorithm. It was originally developed for regression work but later used for linear and non-linear classification. In an SVM, the cloud that defines the boundary in the data space is trained to maximize the distance to the nearest data. SVMs can have higher performance in classification and regression problems than other statistical and ML techniques.

KNN is a widely used method for data mining. This method determines the similarity between the new data and the existing data and groups the new data into groups similar to the existing data. The algorithm works on this basis.

1.Choosing the number of K neighbors.

2.Calculate the "Euclidean distance", which is to measure the distance between any two points. Formula like equation 22.

$$D=\sqrt{((X_2-X_1)^2+(Y_2-Y_1)^2)} \quad (22)$$

3.From the calculation in step 2.

4. The bundle for a new data point is assigned to the maximum number of neighbors.

RF random forest is a group algorithm that uses bagging as a set method and decision tree as an individual method, thus helping to reduce variance and bias in improved findings. The classifier combines multiple decision trees and a more robust classification with better generalization and easier hyperparameter tuning to overcome overfitting problems. For classification tasks in RF, each tree provides a classification or takes a "vote".

IV. EVALUATION

In this article, a new method based on image thinning features and common classifications is proposed. In the following, the proposed method will be evaluated with common evaluation criteria. The system used for simulation is an Intel processor system. The desired hardware is a 5-core (Core™) i7 CPU with a working frequency of 2.60GHz. 8 GB of RAM. The Windows 10 operating system is installed on this system. The software used is MATLAB 2022b. To classify the integrated features, the mutual validation method is used with a factor of 10 (K=10), which means that the data is first divided into 10 equal categories (because the factor of 5 has a better bias and considering that the number the registrations were 120, the test coefficient was 30%, and the training was 70%. In each stage, one group out of 10 categories is used for testing and four other categories are used for training, and finally, the average is made between the 10 classification indicators of the test. This process is generally shown in Figure 11.

Fig. **11.** Cross-validation method from the tenth rank.

The proposed method is analyzed using a variety of Accuracy and Precision evaluation criteria. These two criteria are among the most significant evaluation criteria for diagnosis and classification. Therefore, these two criteria are used in this research. Two accuracy and precision evaluation criteria, recall rate and sensitivity, and F-Measure are introduced and calculated according to equations 23 and 27 and used to evaluate the system [32].

$$\mathrm{Re}call = \frac{TP}{TP + FN} \tag{23}$$

$$ACC = \frac{TN + TP}{TN + TP + FN + FP} \tag{24}$$

$$Specificity = \frac{TN}{TN + FP} \tag{25}$$

$$F\_Measure = \frac{2 \times TP}{2 \times TP + FP + FN} \tag{26}$$

In these equations, TP, is true positive, TN, is true negative, FP, is false positive, and FN, is false negative.

A. Databases

A dataset will be used in this paper. Fetal head ultrasound is a dataset for measuring fetal head circumference (HC), ultrasound imaging used to measure fetal biometrics during pregnancy. The dataset is part of the HC18 challenge and contains a total of 1334 two-dimensional (2D) ultrasound images of a standard plane that can be used to measure HC. All two-dimensional (2D) ultrasound images of HC were collected from the database of the Department of Obstetrics and Gynecology, Radboud University Medical Center, Nijmegen, The Netherlands. Ultrasound images were obtained from 551 pregnant women who received a routine ultrasound screening examination between May 2014 and May 2015. Only embryos that did not show any developmental abnormalities were included in this study. Images were obtained by experienced sonographers using a Voluson E8 or Voluson 730 ultrasound machine (General Electric, Austria). CMO Arnhem-Nijmegen approved the collection and use of these data for this study. Due to retrospective data collection, informed consent was waived. All data were anonymized according to the principles of the Declaration of Helsinki. The size of each 2D ultrasound image was 800 x 540 pixels, with pixel sizes ranging from 0.052 to 0.326 mm. This large variation in pixel size is the result of ultrasound settings by the sonographer (depth and zoom settings typically vary during the exam) to account for different fetal sizes. The size of each 2D ultrasound image was 800 x 540 pixels, with pixel sizes ranging from 0.052 to 0.326 mm. This large variation in pixel size is the result of ultrasound adjustments by the sonographer (depth and zoom settings typically

vary during the exam) to account for different fetal sizes. Figure 12 shows sample ultrasound images from each trimester. The distribution of GA in this study is shown in Figure 12. Most of the data were obtained after 12 and 20 weeks of gestation, as these are the standard times for routine ultrasound screening for pregnant women in the Netherlands. During each examination, the sonographer manually annotated the HC. This was done by drawing an ellipse that best fit the head circumference. Figure 12 also shows a comparison between the HC distribution and the Verburg et al. growth curve. The reference GA was determined by measuring the CRL between 20 mm (8+4 weeks) and 68 mm (12+6 weeks). This database is available at https://datasetninja.com/fetal-head-ultrasound.

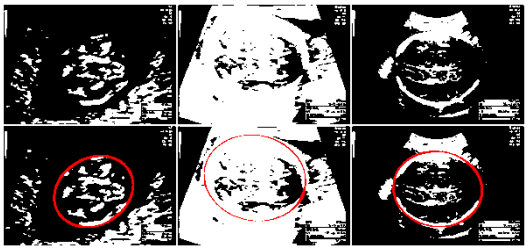

Fig. **12.** Some images in the database.

B. Results

Table 1, shows the test accuracy and validity loss of the proposed network with three tests in multi-class AD classification. The average of each time in the detection of each state is also determined. It is important to repeat the experiment to show that the results obtained are not random. The best average test accuracy is obtained with the proposed network in the second run. Table 2 shows the final evaluation results in more detail and in each test in terms of accuracy, recall rate, F criterion, and AUC criterion.

Table **1**.Comparison of the accuracy of fetal brain health diagnosis in different implementations with different classifications.

Class Name	SVM	KNN	RF
Normal	0.9593	0.9688	0.9900
Suspicious	0.9984	0.9999	0.9685
Sick	0.9729	0.9801	0.9801

Figure 13 shows the comparison of accuracy in different conditions of fetal brain health in three tests, as well as the average value. As can be seen in Figure 13, the accuracy of diagnosis in all stages is more than 98%. This is important because of the entry of the most informative bands of the image into the proposed deep neural network, and also the settings made in the proposed deep network.

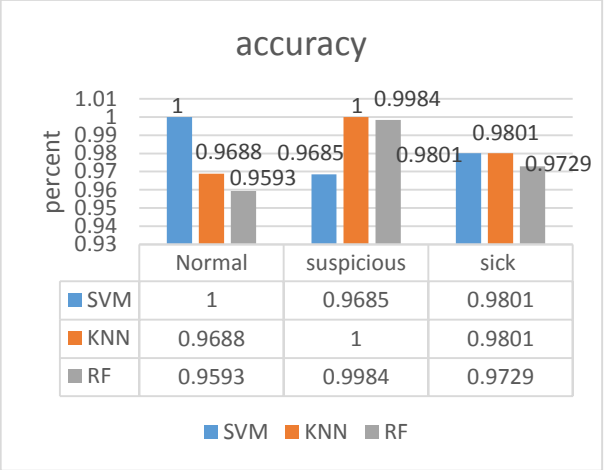

Fig. **13.** Graphical comparison of the results in detection accuracy.

Table **2**.Comparison of the results obtained in different tests in the rest of the criteria.

Evaluation Criteria	Class Name	Normal	Suspicious	Sick
Precision	SVM	0.9979	0.9984	1.0000
	KNN	0.9988	0.9999	1.0000
	RF	0.8964	1.0000	1.0000
Recall	SVM	0.9593	0.9729	0.9713
	KNN	0.9686	0.9801	0.9781
	RF	1.0000	0.9801	0.9740
F-Measure	SVM	0.9782	0.9855	0.9854
	KNN	0.9836	0.9899	0.9899
	RF	0.9454	0.9899	0.9868
AUC	SVM	0.9994	0.9995	0.9996
	KNN	0.9996	0.9997	0.9997
	RF	0.9996	0.9997	0.9997

Figure 14, shows the comparison of accuracy, figure 15, compares the recall rate, figure 16, compares the F criterion and figure 17, shows the comparison of AUC in different states of fetal brain health in three tests with three categories used.

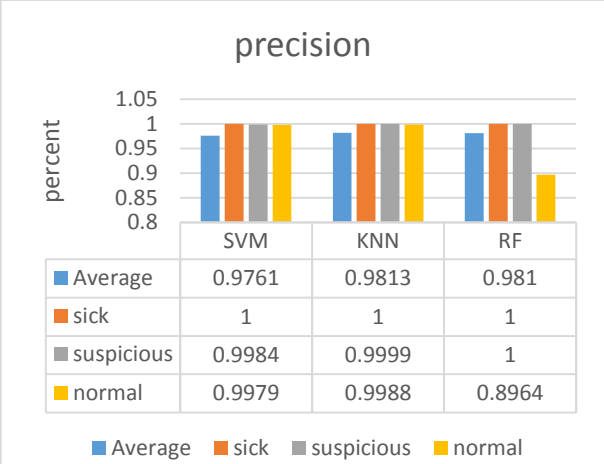

Fig. **14.** Comparison of the accuracy of fetal brain health diagnosis for each category

.

As seen in these figures, the criteria obtained in all stages are more than 98%. This is important because of the inclusion of the most informative features in the desired and proposed classifications, as well as the adjustments made in the proposed method.

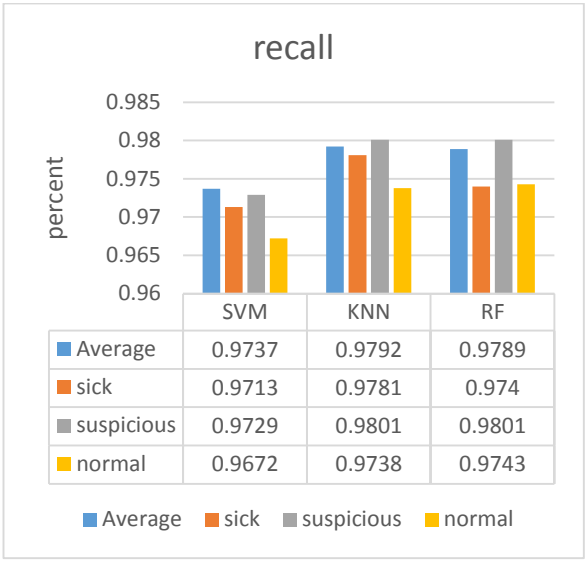

Fig. **15.** Comparison of the recall rate of fetal brain health diagnosis for each category.

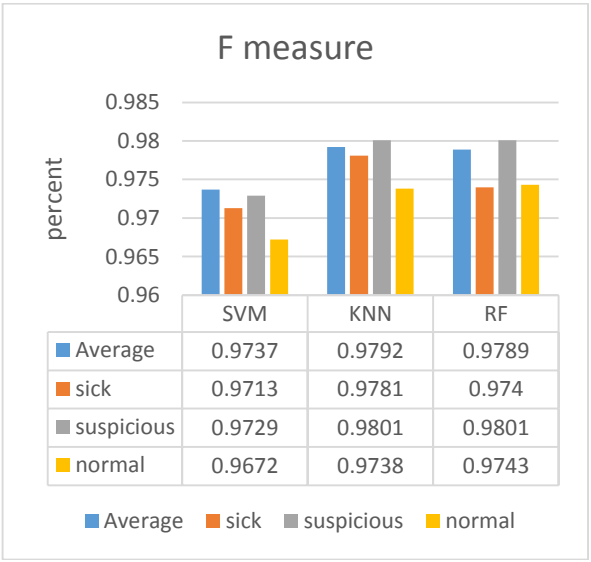

Fig. **16.** Comparison of the F criteria for diagnosing fetal brain health status for each category.

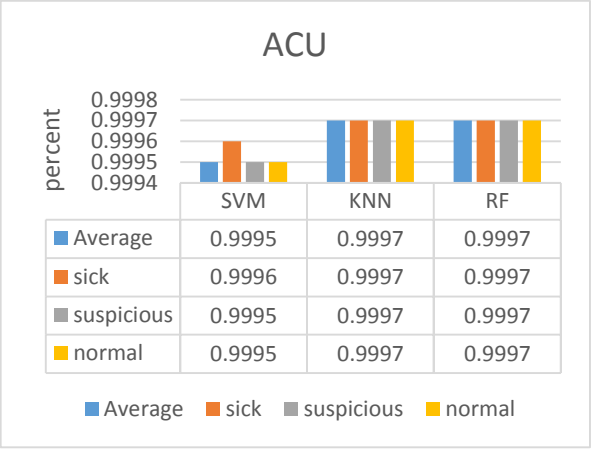

Fig. **17.** Comparison of the AUC criterion for detecting fetal brain health status in each test.

C. Comparison with other research

The proposed performance was evaluated three times with three different categories. Also, the results obtained were compared with [33]. This research has been divided into two groups: healthy and sick. To make a comparison, using the same data sample, data partitioning, and the number of steps, an additional evaluation is compared with the Alex Net training used on the dataset [34]. The classification results have been evaluated in terms of the average classification precision and accuracy of each AD stage. Table 3 provides a comparative analysis and also summarizes the classification results with other approaches.

Table **3**. Comparison with the reference [35]in diagnosing fetal brain health status.

Pathology	[35]	SVM	KNN	AlexNet
Normal	98.34	100.0	96.88	91.73
Suspicious	94.55	96.85	100.0	100.0
Sick	94.97	98.01	98.01	95.14

In the comparative analysis, the proposed model has performed better than [34]and the trained AlexNet model. In all implementations, the accuracy and correctness of the proposed method are much better. The reason for this is the use of the most informative scattered extracted features with the help of the selection of the proposed feature and the settings made on the proposed method. In order to further evaluation, the proposed method has been compared with the other methods of diagnosing fetal brain health status, which have been done by other researchers. The database of these studies is the same in Table 4. In [36], deep learning based on support vector machines [37], deep learning based on convolutional neural networks [38] are compared. The results obtained in accuracy in the three cases compared show the superiority of the proposed method in diagnosing the progress of the disease stage.

V. CONCLUSION

Early diagnosis of fetal diseases is very important to improve the quality of life of people after birth and to develop improved treatment and targeted drugs.

Table **4**. Comparison with other research in different situations.

Reference	Subjects	Task	ACC
[36]	43,890 images, 16,463 subjects	Sick again NL	94.10 87.14 85.85
[37]	INTERGROWTH21st dataset INTERBIO-21st dataset [40]	Sick again NL	97.79 94.73 42.70
[38]	INTERGROWTH21st dataset INTERBIO-21st dataset [40]	Sick again NL	96.47 88.47 80.17
Proposed D2 Model	INTERGROWTH21st dataset INTERBIO-21st dataset [40]	Sick again NL	98.61 98.67 98.87

In this article, the purpose of investigating the effectiveness of ultrasound imaging in advanced machine learning techniques for the classification and diagnosis of multiple classes of fetal health was carried out. This study proposed the use of various machine learning classifiers along with various features based on the thinning transformation to perform 3-class classification. The proposed method was trained three times separately on single-channel ultrasound images. Using the proposed method helped to achieve better performance. The results of this study show that the integration of imaging methods and machine learning can help to make diagnostic decisions in the early diagnosis of fetal diseases. Diagnosing fetal health status can aid drug discovery by providing better pathogenesis to measure the effects of targeted therapies that can slow disease progression. By combining clinical imaging with machine learning techniques, we can help uncover patterns of functional changes in the brain associated with the development of fetal health and can help identify risk factors and prognostic indicators.

REFERENCES

[1] Z. Alfirevic, G. M. Gyte, A. Cuthbert, and D. Devane, "Continuous cardiotocography (CTG) as a form of electronic fetal monitoring (EFM) for fetal assessment during labour," *Cochrane database of systematic reviews*, no. 2, 2017.

[2] N. Muhammad Hussain ,A. U. Rehman, M. T. B. Othman, J. Zafar, H. Zafar, and H. Hamam, "Accessing artificial intelligence for fetus health status using hybrid deep learning algorithm (AlexNet-SVM) on cardiotocographic data," *Sensors*, vol. 22, no. 14, pp. 5103, 2022.

[3] K. Barnova, R. Martinek, R. Vilimkova Kahankova, R. Jaros, V. Snasel, and S. Mirjalili, "Artificial Intelligence and Machine Learning in Electronic Fetal Monitoring," *Archives of Computational Methods in Engineering*, pp. 1-32, 2024.

[4] M. Vafaeezadeh, H. Behnam, and P. Gifani, "Ultrasound Image Analysis with Vision Transformers–Review," 2024.

[5] M. C. Fiorentino, F. P. Villani, M. Di Cosmo, E. Frontoni, and S. Moccia, "A review on deep-learning algorithms for fetal ultrasound-image analysis," *Medical image analysis*, vol. 83, pp. 102629, 2023.

[6] P. H. Diniz, Y. Yin, and S. Collins, "Deep learning strategies for ultrasound in pregnancy," *European Medical Journal. Reproductive health*, vol. 6, no. 1, pp. 73, 2020.

[7] P.-H. Yeung, L. S. Hesse, M. Aliasi, M. C . Haak, W. Xie, A. I. Namburete, and I.-s. Consortium, "Sensorless volumetric reconstruction of fetal brain freehand ultrasound scans with deep implicit representation," *Medical Image Analysis*, vol. 94, pp. 103147, 2024.

[8] S. MolinaGiraldo, N. TorresValencia, C. TorresValencia, and H. F. Restrepo, "Anatomical structure characterization of fetal ultrasound images using texture based segmentation technique via an interactive MATLAB application," *Journal of Clinical Ultrasound*, vol. 52, no. 2, pp. 189-20.٢٠٢٤ ,٠

[9] H. P. Kim, S. M. Lee, J.-Y. Kwon, Y. Park, K. C. Kim, and J. K. Seo, "Automatic evaluation of fetal head biometry from ultrasound images using machine learning," *Physiological measurement*, vol. 40, no. 6, pp. 065009, 2019.

[10] J. Yu, Y. Wang ,P. Chen, and Y. Shen, "Fetal abdominal contour extraction and measurement in ultrasound images," *Ultrasound in medicine & biology*, vol. 34, no. 2, pp. 169-182, 2008.

[11] Z. Cömert, A. F. Kocamaz, and V. Subha, "Prognostic model based on image-based time-frequency features and genetic algorithm for fetal hypoxia assessment," *Computers in biology and medicine*, vol. 99, pp. 85-97, 2018.

[12] S. Thomas, and S. Harikumar, "An ensemble deep learning framework for foetal plane identification," *International Journal of Information Technology*, pp. 1-10, 2024.

[13] M. Alzubaidi, U. Shah, M. Agus, and M. Househ, "FetSAM: Advanced Segmentation Techniques for Fetal Head Biometrics in Ultrasound Imagery," *IEEE Open Journal of Engineering in Medicine and Biology*, 202.٤

[14] M. Lin, Q. Zhou, T. Lei, N. Shang, Q. Zheng, X. He, N. Wang, and H. Xie, "Deep learning system improved detection efficacy of fetal intracranial malformations in a randomized controlled trial," *NPJ Digital Medicine*, vol. 6, no. 1, pp. 191, 2023.

[15] V. Nagabotu, and A. Namburu, "Precise segmentation of fetal head in ultrasound images using improved U- Net model," *ETRI Journal*, 2023.

[16] H. Ghabri, M. S. Alqahtani, S. Ben Othman, A. Al-Rasheed, M. Abbas, H. A. Almubarak, H. Sakli, and M. N. Abdelkarim, "Transfer learning for accurate fetal organ classification from ultrasound images: a potential tool for maternal healthcare providers," *Scientific Reports*, vol. 13, no. 1, pp. 17904, 2023.

[17] M. C. Walker, I. Willner, O. X. Miguel, M. S. Murphy, D .El-Chaâr, F. Moretti, A. L. Dingwall Harvey, R. Rennicks White, K. A. Muldoon, and A. M. Carrington, "Using deep-learning in fetal ultrasound analysis for diagnosis of cystic hygroma in the first trimester," *Plos one*, vol. 17, no. 6, pp. e0269323, 2022.

[18] Y. Zhou, "Prediction and value of ultrasound image in diagnosis of fetal central nervous system malformation under deep learning algorithm," *Scientific Programming*, vol. 2021, pp. 1-7, 2021.

[19] P. Deepika, R. Suresh, and P. Pabitha, "Defending Against Child Death: Deep learning based diagnosis method for abnormal

identification of fetus ultrasound Images," *Computational Intelligence*, vol. 37, no. 1, pp. 128-154, 2021.

[20] X. P. Burgos-Artizzu, D. Coronado-Gutiérrez, B. Valenzuela-Alcaraz, E. Bonet-Carne, E. Eixarch, F. Crispi, and E. Gratacós, "Evaluation of deep convolutional neural networks for automatic classification of common maternal fetal ultrasound planes," *Scientific Reports*, vol. 10, no. 1, pp. 10200, 2020.

[21] R. Qu, G. Xu, C. Ding, W .Jia, and M. Sun, "Deep learning-based methodology for recognition of fetal brain standard scan planes in 2D ultrasound images," *Ieee Access*, vol. 8, pp. 44443-44451, 2019.

[22] P. Durka, M. Dovgialo, A. Duszyk-Bogorodzka, and P. Biegański, "Two-Stage Atomic Decomposition of Multichannel EEG and the Previously Undetectable Sleep Spindles," *Sensors*, vol. 24, no. 3, pp. 842, 2024.

[23] B. A. Olshausen, and D. J. Field, "Sparse coding with an overcomplete basis set: A strategy employed by V1?," *Vision research*, vol. 37, no. 23, pp. 3311-3325, 1997.

[24] M. Aharon, M. Elad, and A. Bruckstein, "K-SVD: An algorithm for designing overcomplete dictionaries for sparse representation," *IEEE Transactions on signal processing*, vol. 54, no. 11, pp. 4311-4322, 2006.

[25] J. Stromberg, "A Modified Haar System and Higher Order Spline Systems; Conf. in Honor of A. Zygmund," *Wadsworth Math. Series*, pp. 475-493, 1981.

[26] Y. Meyer, "Principe d'incertitude, bases hilbertiennes et algebres d'operateurs," *Séminaire Bourbaki*,vol. 662, 1986.

[27] I. Daubechies, "Orthonormal bases of compactly supported wavelets," *Communications on pure and applied mathematics*, vol. 41, no. 7, pp. 909-996, 1988.

[28] G. Beylkin, "On the representation of operators in bases of compactly supported wavelets," *SIAM Journal on Numerical Analysis*, vol. 29, no. 6, pp. 1716-1740, 1992.

[29] A. Benkessirat, and N. Benblidia, "Fundamentals of feature selection: An overview and comparison." pp. 1-6.

[30] M. A. Valizade Hasanloei, R. Sheikhpour, M. A. Sarram, E. Sheikhpour, and H. Sharifi, "A combined Fisher and Laplacian score for feature selection in QSAR based drug design using compounds with known and unknown activities," *Journal of Computer-Aided Molecular Design*, vol. 32, no. 2, pp. 375-384, 2018.

[31] M. Azhar, and P. A. Thomas, "Comparative review of feature selection and classification modeling." pp. 1-9.

[32] S. Qi, X. Wu, W.-H. Chen, J. Liu, J. Zhang, and J. Wang, "sEMG-based recognition of composite motion with convolutional neural network," *Sensors and Actuators A: Physical*, vol. 311, pp. 112046, 2020.

[33] V. Gude, and S. Corns, "Integrated deep learning and supervised machine learning model for predictive fetal monitoring," *Diagnostics*, vol. 12, no. 11, pp. 2843, 2022.

[34] R. Sreelakshmy ,A. Titus, N. Sasirekha, E. Logashanmugam, R. B. Begam, G. Ramkumar, and R. Raju, "[Retracted] An Automated Deep Learning Model for the Cerebellum Segmentation from Fetal Brain Images," *BioMed Research International*, vol. 2022, no. 1, pp. 8342767, 2022.

[35] Y. Kazemi, and S. Houghten, "A deep learning pipeline to classify different stages of Alzheimer's disease from fMRI data." pp. 1-8.

[36] H. Xie, N. Wang, M. He, L. Zhang, H. Cai, J. Xian, M. Lin, J. Zheng, and Y. Yang, "Using deep- learning algorithms to classify fetal brain ultrasound images as normal or abnormal," *Ultrasound in Obstetrics & Gynecology*, vol. 56, no. 4, pp. 579-587, 2020.

[37] M. Lin, X. He, H. Guo, M. He, L. Zhang, J. Xian, T. Lei, Q. Xu, J. Zheng, and J. Feng, "Use of real- time artificial intelligence in detection of abnormal image patterns in standard sonographic reference planes in screening for fetal intracranial malformations," *Ultrasound in Obstetrics & Gynecology*, vol. 59, no. 3, pp. 304-316, 2022.

[38] L. H. Lee, E. Bradburn, R .Craik, M. Yaqub, S. A. Norris, L. C. Ismail, E. O. Ohuma, F. C. Barros, A. Lambert, and M. Carvalho, "Machine learning for accurate estimation of fetal gestational age based on ultrasound images," *NPJ digital medicine*, vol. 6, no. 1, pp. 36, 2023.

[39] W. Li, X. Lin, and X. Chen, "Detecting Alzheimer's disease Based on 4D fMRI: An exploration under deep learning framework," *Neurocomputing*, vol. 388, pp. 280-287, 2020.

[40] J. Villar, R. B. Gunier, C. O. Tshivuila-Matala, S. A. Rauch, F. Nosten, R. Ochieng, M. C. Restrepo-Méndez, R. McGready, F. C. Barros, and M. Fernandes, "Fetal cranial growth trajectories are associated with growth and neurodevelopment at 2 years of age: INTERBIO-21st Fetal Study," *Nature Medicine*, vol. 27, no. 4, pp. 647-652, 2021.

THIS PAGE IS INTENTIONALLY LEFT BLANK.

IJBBE International Journal of Biophotonics & Biomedical Engineering Vol. 5, No. 1, Spring-Summer , 2025

Review Article

A review of the antibacterial properties of zinc oxide nanoparticles: synthesis, mechanism of action, and medical applications

A. Jafari-Sales[a,b], Z. Ghahremani[b,c], A. Golestani[b,c], M. Pashazadeh[b,d*]

a Department of Microbiology, Kaz.C., Islamic Azad University, Kazerun, Iran.
b Infectious Diseases Research Center, TaMS.C., Islamic Azad University, Tabriz, Iran
c Department of Cellular and Molecular Biology, Ta.C., Islamic Azad University, Tabriz, Iran
d Department of Laboratory Sciences and Microbiology, TaMS.C., Islamic Azad University, Tabriz, Iran

***Corresponding Author Email: mehrdadpashazadeh85@gmail.com**

DOI: 10.71498/ijbbe.2025.1202308

ABSTRACT

Received: Mar. 17, 2025, Revised: May. 21, 2025, Accepted: May. 25, 2025, Available Online: Jul. 24, 2025

Zinc oxide nanoparticles (ZnO-NPs) have emerged as one of the leading nanomaterials, demonstrating strong antimicrobial properties and high potential in controlling bacterial infections. ZnO-NPs exert their antibacterial effects through the generation of reactive oxygen species, damage to the cell membrane, and disruption of bacterial DNA and protein functions. Numerous studies have shown that these nanoparticles are effective against a wide range of Gram-positive and Gram-negative bacteria, including antibiotic-resistant strains. The small size, high specific surface area, and ability to penetrate bacterial cell walls are key factors contributing to the efficacy of these nanoparticles. Furthermore, due to their minimal side effects on human cells and high biocompatibility, ZnO-NPs are considered a suitable option for clinical and industrial applications. The applications of these nanoparticles have been extensively reviewed, and potential strategies to enhance their efficiency and safety have been proposed. This study highlights the significant potential of ZnO-NPs to either replace or complement existing methods in combating bacterial infections, offering a novel approach to addressing antibiotic resistance and other challenges. This article reviews the antibacterial mechanisms of ZnO-NPs, examining factors influencing their activity and performance, and their potential applications in medical and industrial fields.

KEYWORD

Zinc oxide, metal nanoparticles, multifunctional nanoparticles, reactive oxygen species, antibacterial agents

I. INTRODUCTION

Nanotechnology has garnered significant global attention in the field of modern materials science and its applications in medicine and other scientific disciplines. Nanoparticles, defined as particles with sizes ranging from 1 to 100 nanometers, have demonstrated their efficacy in treating infectious diseases, including antibiotic-resistant strains, in both in vitro and animal models. Due to their high surface area, nanomaterials exhibit remarkable mechanical, optical, magnetic, and chemical properties. These tiny particles represent a modified version of fundamental elements, achieved through the manipulation of their atomic and molecular characteristics. Research has shown that antibacterial mineral materials often include metal nanoparticles and metal oxide nanoparticles, such as Ag, Au, Cu, TiO_2, and Zinc oxide (ZnO). Among metal oxide nanoparticles, ZnO has found extensive applications due to its optical (1), semiconducting (2), ultraviolet (UV) absorbing (3), and antimicrobial (4) properties (5-8). Zinc (Zn) is an essential element used in medicine, biology, and industry. Adults require 8 to 15 mg of Zn daily, with 5 to 6 mg lost through urine and sweat. Zn is vital for bones, teeth, enzymes, and proteins (9). The use of metallic nanoparticles and their oxides represents a promising approach to combating antibiotic resistance (10). Metal oxide nanoparticles are notable for their catalytic inhibitory activity in antimicrobial compounds. However, their bactericidal mechanisms depend on various factors, such as morphology, composition, and concentration (11). Given the emergence of new bacterial mutations, increasing antibiotic resistance, and the proliferation of pathogenic strains, there is a pressing need for the advancement and development of more effective antibacterial agents. ZnO has always been of interest due to its strong antibacterial properties (12). With the rise of bacterial resistance to conventional antibiotics, there is a growing need for innovative and effective methods to combat bacterial infections. Zinc oxide nanoparticles (ZnO-NPs) have emerged as a promising alternative due to their strong antibacterial properties, high biocompatibility, and relatively low production costs. The exact mechanisms of ZnO-NPs antibacterial effects, as well as the optimization of synthesis techniques to increase efficiency and lower potential toxicity, remain unclear despite the large number of investigations that have been done on their synthesis and applications. This article provides a comprehensive review of ZnO-NPs synthesis methods, analyzes their antibacterial mechanisms, and introduces medical applications while proposing strategies for the effective use of this technology in health and treatment. A deeper understanding of these aspects can pave the way for the development of more effective and safer treatments for bacterial infections.

II. STRUCTURE AND PHYSICOCHEMICAL PROPERTIES OF ZINC OXIDE

All of the human body's tissues contain Zn; however, muscle and bone have the highest concentration (around 85% of the total zinc content) (13). Zn is essential for the proper functioning of numerous macromolecules and enzymes, serving as a coenzyme with catalytic and structural roles. Furthermore, protein subdomains can interact with DNA or other proteins thanks to the special framework that zinc-finger structures offer (14). ZnO is an inorganic compound that typically appears as a white powder and is insoluble in water (15). ZnO exhibits three crystalline structures: wurtzite, zinc-blende, and rock salt, with the latter being rarely observed. Crystalline ZnO has a wurtzite structure with a hexagonal unit cell. Each anion is surrounded by four cations in a tetrahedral arrangement, representing sp^3 covalent bonding and creating an asymmetric structure (16). ZnO-NPs are versatile materials widely used in biosensors, cosmetics, drug delivery, and agriculture due to their optical,

electrical, piezoelectric, and antimicrobial properties. The morphology of ZnO-NPs, such as nanorods (17), nanowires (18), and nanoflowers, depends on the synthesis process (19). Traditional methods for synthesizing ZnO-NPs, including sol-gel, hydrothermal, and mechanochemical processes, are often time-consuming, expensive, and require high temperatures and specialized precursors. These methods also generate significant chemical waste (20). In contrast, green synthesis of nanoparticles utilizes renewable organic extracts from sources such as yeast, bacteria, and plants. This approach avoids the use of toxic chemicals and helps reduce waste (21). Compared to other nanoparticles in the same group, Zn demonstrates higher antibacterial activity against Gram-positive bacteria (9). The synthesis of ZnO-NPs has led to their investigation as a novel antibacterial agent. In addition to strong antibacterial and antifungal properties, these nanoparticles exhibit high catalytic and photochemical activities. Furthermore, ZnO has high optical absorption in the UVA and UVB ranges, making it suitable for antibacterial applications and UV protection in cosmetics (22). ZnO is a wide-bandgap semiconductor (3.37 eV at room temperature) with unique properties such as high transparency, strong luminescence, and excellent electron mobility (23). Despite partial covalent characteristics, ZnO primarily features strong ionic bonding in its Zn-O structure, contributing to superior durability, enhanced selectivity, and greater thermal resistance compared to organic and inorganic materials (4). According to an investigation using scanning electron microscopy and energy dispersive X-ray, ZnO-NPs are mostly made up of Zn (37.5%), oxygen (19.9%), and carbon (42.6%), which is consistent with the green synthesis technique used (24).

III. METHODS FOR SYNTHESIS OF ZINC OXIDE NANOPARTICLES

ZnO-NPs are produced using various physical and chemical methods such as solvent evaporation, sol-gel, physical degradation, interference lithography, vapor condensation, and microemulsion deposition (25, 26). However, chemical methods often employ toxic substances that are hazardous to operators and harmful to the environment, while physical methods require high energy, pressure, and temperature (27). Common toxic compounds used in chemical synthesis include triethylamine (28), oleic acid (29), thioglycerol (30), polyvinyl alcohol (31), and ethylene diamine tetraacetic acid (32). These compounds are typically used as stabilizers or coatings to control nanoparticle size and prevent aggregation. However, residual amounts of these compounds in the final product may introduce toxicity, limiting the biomedical and environmental applications of the nanoparticles (25). Green synthesis of metal and metal oxide nanoparticles using biological methods (particularly plant extracts, microorganisms, and fungi) has emerged as a novel field in nanotechnology, offering a sustainable alternative to chemical and physical approaches (33, 34). Natural sources such as plants, algae, fungi, and non-pathogenic microorganisms (e.g., Lactobacillus bacteria) are used in the biosynthesis of ZnO-NPs. This approach represents an eco-friendly, cost-effective, and green solution that utilizes biological compounds (e.g., enzymes and secondary metabolites) for the safe and sustainable production of nanoparticles with minimal environmental contamination and without hazardous chemicals (32, 35). Plant extracts are more widely used in nanoparticle synthesis than microorganism-based methods due to their bioactive phytomolecules (e.g., flavonoids and terpenoids) and advantages such as high biocompatibility and simple extraction processes (36). Phytochemical studies have shown that key plant-derived compounds and metabolites, including lupeol, oleanolic acid, kaempferol glycosides, quercetin, leucocyanidin, ursolic acid, sitosterol, rutin, anthocyanins, and proanthocyanidins possess antioxidant, antibacterial, antimutagenic, and chemopreventive properties (37). Studies indicate that ZnO-NPs synthesized from plant extracts exhibit superior antibacterial properties compared to conventional drugs in disease treatment (38). In this synthesis, plant

components (roots, leaves, stems, seeds, and fruits) are used because their extracts contain high concentrations of phytochemicals that act as stabilizing and reducing agents. The most common method for preparing ZnO-NPs from leaves or flowers involves washing, sterilization, drying, grinding, adding Milli-Q H_2 O, boiling, filtering, and finally mixing with hydrated zinc nitrate, ZnO, or zinc sulfate (39). Although green synthesis of ZnO-NPs is promising, variability in plant extract composition can lead to heterogeneity in nanoparticle size, shape, and purity. This necessitates precise control of reaction parameters (e.g., metal ion concentration, temperature, pH, and time) to ensure reproducibility (40-43). Recent studies have demonstrated the efficacy of lactic acid bacteria (LAB) in mediating ZnO-NP synthesis (44, 45). Given their ability to synthesize metallic nanoparticles (e.g., Se, Au, and Ag), LAB strains are recognized as efficient cellular factories for metal nanoparticle production. Gram-positive LAB possess thick cell walls composed of peptidoglycan, lipoteichoic acid, collagen, and polysaccharides. Due to their negative electrophoretic mobility, these layers serve as sites for biosorption of metal ions and bioreduction, attracting metal cations to initiate nanoparticle biosynthesis (46, 47). Green production of ZnO-NPs using bacteria such as Lactobacillus and Bacillus has gained attention as a sustainable and eco-friendly alternative to chemical methods. Species like Lactobacillus plantarum and Lactobacillus casei significantly contribute to metal ion reduction and ZnO-NP formation through their bioactive metabolites and enzymes. Studies show these nanoparticles are predominantly spherical (average size: 10–13 nm) and exhibit exceptional antibacterial and antibiofilm properties (48-50). Green synthesis of ZnO-NPs has also been achieved using non-Lactobacillus bacteria (e.g., Bacillus subtilis), enabling tailored control over nanoparticle size and morphology. These nanoparticles are effective in organic pollutant removal and exhibit strong antibacterial activity against Salmonella typhimurium, Escherichia coli, and Staphylococcus aureus (S. aureus) (51). Enzymes produced by non-pathogenic Lactobacillus strains can act as reducing, stabilizing, or capping agents in nanoparticle synthesis (43).

IV. The Effect of Zinc Oxide on Gram-Positive and Gram-Negative Bacteria

ZnO-NPs exhibit effective antimicrobial and anti-biofilm properties, impacting a wide range of Gram-positive and Gram-negative bacteria (52). ZnO-NPs effectively target drug-resistant bacteria, disrupt biofilms, and reduce the virulence of pathogens. They also demonstrate promising antifungal properties, particularly for skin infections (53). During the exponential development phase, ZnO-NPs exhibit potent antibacterial properties against both Gram-positive and Gram-negative bacteria. However, their antibacterial efficacy significantly decreases during the lag and stationary phases of bacterial growth (54). Biologically synthesized ZnO-NPs have demonstrated significantly higher growth inhibition compared to chemically synthesized ZnO-NPs and other conventional antimicrobial agents. ZnO also exhibits notable selectivity, greater durability, and good thermal resistance. These unique properties make ZnO a powerful tool in combating a wide range of microorganisms, including *S. aureus* (55, 56), *Escherichia coli* (57). TiO_2, ZnO, and Ag are used in various fields to regulate microbial proliferation. However, ZnO exhibits greater biocompatibility compared to TiO_2 due to its exceptional photocatalytic efficiency (58). Green-synthesized ZnO-NPs demonstrate antibacterial properties against both Gram-positive and Gram-negative bacteria (59). Typically, Gram-negative bacteria show lower sensitivity to ZnO-NPs compared to Gram-positive bacteria. This increased resistance in Gram-negative bacteria can be attributed to the unique structure of their cell walls, which, unlike Gram-positive bacteria, include an additional outer membrane composed of lipopolysaccharides that reduces their susceptibility (60, 61). ZnO-NPs inhibit the formation of amyloid peptide fibrils, which are essential for bacterial biofilm formation (62). The combination of meropenem and ZnO-NPs reduces the expression of genes associated with

biofilm formation. Additionally, the small size of ZnO-NPs enhances their ability to penetrate the biofilm matrix, leading to stronger anti-biofilm activity. Complete biofilm removal in certain areas has been observed using scanning electron microscopy (63). Based on evidence from studies, ZnO-NPs, particularly those synthesized via green methods, are considered promising anti-biofilm agents for medical applications (e.g., implant coatings) and the control of biofilm-related infections (64). According to studies, ZnO-NPs reduce the ability of *S. aureus* to form biofilms by inhibiting the expression of biofilm-related genes such as *ica A*, *ica D*, and *fnb A*. These nanoparticles exhibit strong antibacterial activity against multidrug-resistant strains of *S. aureus*, including methicillin-resistant, vancomycin-resistant, and linezolid-resistant strains (65) (Table 1).

Name of bacteria	Type of bacteria	Effect of ZnO-NPs	Mechanism of action	Reference
Staphylococcus aureus	Gram positive	Inhibition of bacterial growth, damage to the cell wall, and plasma membrane	Production of reactive oxygen species (ROS), disruption of cell membrane function	(66)
		Reduction of biofilm formation	Inhibition of the expression of biofilm-related genes such as *icaA* and *fnbA*	(67)
Streptococcus pyogenes	Gram positive	Increase in cell membrane permeability	Damage to lipids and membrane proteins	(68)
Escherichia coli	Gram negative	Inhibition of bacterial growth, damage to the outer and plasma membranes	ROS production, damage to lipopolysaccharides, and membrane proteins	(69)
Pseudomonas aeruginosa	Gram negative	Reduction of biofilm formation	Disruption of the biofilm matrix and inhibition of bacterial attachment to surfaces	(70)
Klebsiella pneumoniae	Gram negative	Increase the sensitivity to antibiotics	Increase the permeability of the outer membrane and facilitate the entry of antibiotics.	(71)
Bacillus subtilis	Gram positive	Inhibition of bacterial growth and reduction of spore formation	ROS production, damage to the cell membrane, and disruption of DNA function	(25)
Salmonella typhi	Gram negative	Inhibition of bacterial growth and reduction of biofilm formation	ROS production, damage to the outer membrane, and disruption of DNA function	(72)

V. The Effect of Zinc Oxide on Other Microorganisms

ZnO-NPs exhibit strong antifungal and anti-yeast properties against various harmful fungi and yeasts. Studies have shown that biosynthesized ZnO-NPs are effective against *Fusarium solani*, *Fusarium oxysporum*, *Sclerotinia sclerotiorum*, and *Aspergillus terreus* (73). Additionally, ZnO-NPs produced using *Serratia nematodiphila* have shown significant antifungal activity against *Alternaria* species and *Xanthomonas oryzae* pv. *Oryzae* (74). ZnO-NPs significantly inhibit the growth of yeasts such as *Saccharomyces cerevisiae* (75), *Candida albicans* (76), and *Candida tropicalis* (77). Aquatic ecosystems

may be significantly affected by the toxicity of nanoparticles, and algae are an ideal organism for understanding the impact of nanoparticle toxicity. ZnO-NPs have an effect on the algae *Chlorella vulgaris* (78), *Microcystis aeruginosa* (79), and *Spirulina platensis* (80).

VI. Mechanism of Action of Zinc Oxide on Bacteria

ZnO-NPs, recognized as Generally Recognized as Safe by the U.S. Food and Drug Administration (FDA), are a suitable alternative to antibiotics against drug-resistant bacteria (81). ZnO-NPs exert their antibacterial effects by disrupting bacterial DNA replication processes, causing cell membrane rupture, binding to proteins and DNA, generating reactive oxygen species (ROS), and altering (often reducing) the expression of several genes (10). Metal oxide nanoparticles induce oxidative stress, membrane damage, and cell death by infecting bacteria, increasing ROS production, causing membrane peroxidation, lipid bilayer peroxidation, and leakage of cytoplasmic components (82). Due to its powerful oxidative properties, ZnO damages bacterial cell membranes and disrupts their metabolic pathways by generating ROS and releasing zinc ions (Zn^{2+}). Further studies on the antibacterial mechanisms of ZnO-NPs could enhance our understanding of bacterial resistance mechanisms and improve the contact time and efficacy of ZnO-NPs in inhibiting bacteria (11). The reduction of Zn^{2+} disrupts intracellular Zn^{2+} balance, leading to enzyme inactivation, chromatin structure alteration, inhibition of DNA replication, and ultimately bacterial death (83).

A. Generation of Reactive Oxygen Species by Zinc Oxide

The toxicity of metallic and metal oxide nanoparticles is primarily attributed to their ability to generate ROS (84). Several investigations have demonstrated that the high amounts of ROS generated in ZnO aqueous solutions aid in the antibacterial activity of ZnO. These species include hydroxyl radicals (OH), hydrogen peroxide (H_2O_2), and singlet oxygen, which play a key role in killing bacteria (55). ROS disrupt or alter respiratory cycles, protein synthesis, food metabolism, and DNA replication, leading to cell death (25). Exposure to UV radiation stimulates valence band electrons in ZnO-NPs, creating holes in the conduction band that require energy absorption to cross the bandgap (85). Electrons in the conduction band can reduce molecular oxygen on the ZnO surface, forming superoxide anions, which can react with each other to produce other ROS, such as H_2O_2 (86). H_2O_2 penetrates the cell membrane, causing membrane damage and degradation of DNA and membrane proteins. Negatively charged peroxides cannot cross the cell membrane, and OH^- accumulates on the bacterial cell membrane, destroying it (87).

B. Release of Zn^{2+} Ions and Their Impact on the Antibacterial Activity of Zinc Oxide Nanoparticles

The antibacterial activity of ZnO-NPs is primarily associated with the release of Zn^{2+} ions, which can inhibit bacterial growth by disrupting metal-dependent enzymes and osmotic homeostasis. This toxicity occurs even without direct physical contact with the nanoparticles and is highly dependent on environmental conditions, such as soluble compounds and surface defects of the particles (88). ZnO-NPs can slowly release Zn^{2+} ions in aqueous solutions, which can penetrate the cell membrane, leading to protein denaturation and disruption of cellular respiration. However, studies have shown that increasing Zn^{2+} concentration does not significantly enhance antibacterial effects. Additionally, experiments have demonstrated that minimal Zn^{2+} release under certain conditions does not fully explain high cell mortality. Therefore, Zn^{2+} release should not be considered the primary mechanism of ZnO's antibacterial activity (87) (Figure 1).

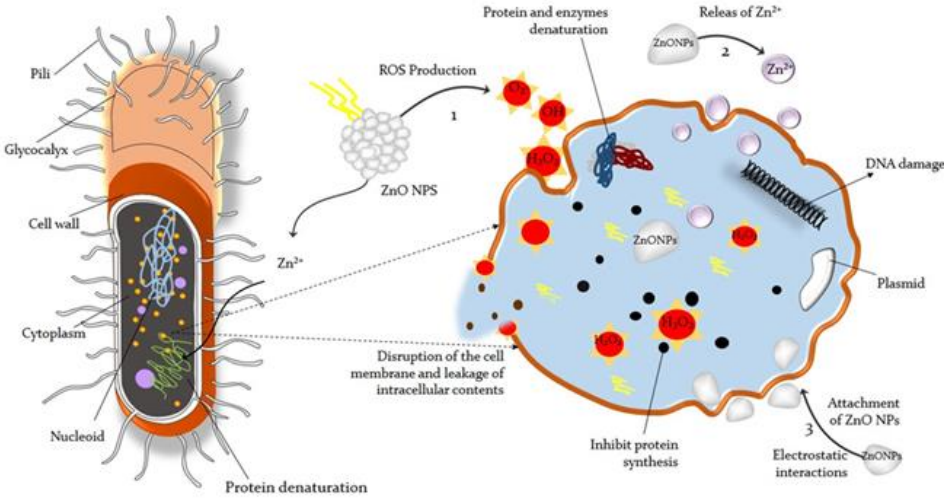

Figure 1. Mechanisms of action of ZnO-NPs on bacteria, including the generation of reactive oxygen species, release of Zn^{2+} ions, and their effects on the cell membrane and bacterial metabolism.

VII. Applications of Zinc Oxide in Medicine and Industry

ZnO nanostructures, due to their multifunctional properties, are utilized in sensors, energy harvesting, and electronic devices. Additionally, in the medical and antiviral fields, ZnO is highly regarded for its excellent biocompatibility, solubility in alkaline environments, and polar surfaces (89). The use of nanoparticles as drug carriers and for targeted delivery of substances, particularly in treating infections caused by microbial biofilms, is a significant and actively researched area among scientists (90). Drug delivery systems are innovative technologies that facilitate the transport of drugs, including tablets and vaccines, into or throughout the body. These systems protect drugs from degradation and maintain their stability until they reach the target site, thereby enhancing the efficacy and safety of therapeutic treatments (91). The small size of nanoparticles enables them to cross the blood-brain barrier (92). Doping ZnO with Gd^{3+} and Al^{3+} improves electrical conductivity and increases charge carrier concentration. The high exciton binding energy of ZnO is attributed to its high dielectric constant, which is influenced by defects such as Zn interstitials and oxygen vacancies. The enhanced dielectric properties of ZnO-NPs are due to oxygen vacancies, nanoscale size effects, and the electronegativity of added impurities. For instance, Li-In doped ZnO achieved a dielectric constant of 3800, with ε′ stabilizing at higher frequencies for doped samples, unlike pure ZnO, where dielectric relaxation was observed in all samples (93). ZnO is well-known for its antibacterial properties in skincare creams and UV protection. The use of modified ZnO-NPs (4%) in coatings for hospital implants can be more effective in controlling bacterial infections. Moreover, these modified nanoparticles are a better option for use in skin lotions and UV protection compared to conventional ZnO (4). In addition to FDA approval, ZnO-NPs are suitable for various biomedical applications, including medical devices, biomedical diagnostics, tissue engineering, healthcare, and drug delivery, due to their simple, safe, and cost-effective production process (94-97). In biology and medicine, ZnO-NPs hold significant value due to their anticancer (98), antimicrobial (99), anti-inflammatory (100, 101), wound-healing (102), bioimaging (103, 104), and antidiabetic (105, 106) properties. The freeze-dry technique was used to create a composite bandage composed of ZnO-NPs and alginate hydrogel. This porous bandage not only demonstrated exceptional antibacterial activity against a wide range of pathogens but also promoted controlled

degradation and accelerated blood clotting (107). According to preliminary research, ZnO-NPs at low concentrations in a biomaterial can enhance tissue integration by improving fibroblast attachment, promoting new blood vessel growth, and accelerating wound healing. ZnO-NPs may also increase levels of angiogenic factors such as vascular endothelial growth factor through the production of ROS (108). Skin wounds should be treated with topical medications that stimulate tissue repair while minimizing free radical production (109, 110). Consequently, having a wound dressing material that possesses both antibacterial properties and wound-healing capabilities is crucial (111).

VIII. Key Challenges in Antimicrobial and Environmental Applications of Zinc Oxide Nanoparticles

Organic materials reduce the antimicrobial efficacy of ZnO-NPs by affecting their stability and surface properties. For instance, ZnO-NPs perform better in organic-free environments because organic compounds limit their activity by coating the nanoparticle surfaces (112). The production process of ZnO-NPs, including the high-energy ball milling of metal powders, reduces particle size and ultimately yields nanoparticles. However, the resulting nanoparticles often have irregular sizes and shapes, which may lead to contamination from the surrounding environment or milling process, rendering them unusable (113). While antimicrobial nanoparticles hold significant potential, they face challenges such as resistance development, biocompatibility and toxicity concerns, environmental impact, nonspecific effects on microbiota, formulation optimization, drug delivery hurdles, and regulatory frameworks (114). The use of man-made nanoparticles in agriculture, such as nanofertilizers and nanopesticides, has led to their accumulation in soil. Although ZnO-NPs are more biocompatible, their antimicrobial properties may disrupt soil microbiota and interfere with key processes such as the nitrogen cycle and plant growth (115). The toxicity of nanoparticles varies depending on their type and concentration. For example, while ZnO-NPs provide UV protection, they can penetrate the skin and generate ROS, leading to cellular damage. Toxicity tests that examine nanoparticle characteristics, exposure pathways, distribution, and biological interactions are essential to ensure safe usage (116). Although the application of ZnO-NPs has been limited due to concerns over toxicity, stability, and environmental effects, targeted synthesis techniques have enabled the development of safer and more efficient formulations. These advancements pave the way for maximizing the antimicrobial and protective capabilities of nanoparticles in healthcare products, provided that safety assessments and regulatory standards evolve alongside technological progress to ensure safer and more effective products (117).

IX. Conclusion

ZnO-NPs have garnered significant attention due to their unique properties, such as antimicrobial and optical activities. As potent antibacterial agents, ZnO-NPs exhibit broad applications, particularly in combating antibiotic-resistant bacteria. By penetrating bacterial cell membranes, ZnO-NPs disrupt membrane integrity and reduce the transcription of genes associated with oxidative stress resistance. In the medical field, these nanoparticles are utilized in drug delivery, bioimaging, cancer therapy, and wound healing. Green synthesis of ZnO-NPs using natural resources offers an environmentally friendly and cost-effective approach. Key challenges in biosynthesis include heterogeneity in nanoparticle size and shape, toxicity arising from ROS and Zn^{2+} ions, environmental accumulation, and scalability issues in large-scale production. However, owing to their high biocompatibility and safety, ZnO-NPs are regarded as promising alternatives to antibiotics and are increasingly being explored for advanced industrial and biomedical applications.

References

[1] Kakhaki ZM, Youzbashi A, Naderi N. “Optical properties of zinc oxide nanoparticles prepared

by a one-step mechanochemical synthesis method," Journal of Physical Science. vol. 26, pp. 41–51, 2015.

[2] Maruthupandy M, Anand M, Maduraiveeran G, Suresh S, Beevi ASH, Priya RJ. "Investigation on the electrical conductivity of ZnO nanoparticles-decorated bacterial nanowires," Advances in Natural Sciences: Nanoscience and Nanotechnology. vol. 7, pp. 045011, 2016.

[3] Goh E, Xu X, McCormick P. "Effect of particle size on the UV absorbance of zinc oxide nanoparticles," Scripta Materialia. vol. 78, pp. 49-52, 2014.

[4] Sirelkhatim A, Mahmud S, Seeni A, Kaus NHM, Ann LC, Bakhori SKM, et al. "Review on zinc oxide nanoparticles: antibacterial activity and toxicity mechanism," Nano-micro letters. vol. 7, pp. 219-242, 2015.

[5] Pulit-Prociak J, Chwastowski J, Bittencourt Rodrigues L, Banach M. "Analysis of the physicochemical properties of antimicrobial compositions with zinc oxide nanoparticles," Science and Technology of Advanced Materials. vol. 20, pp. 1150-1163, 2019.

[6] Daniel M-C, Astruc D. "Gold nanoparticles: assembly, supramolecular chemistry, quantum-size-related properties, and applications toward biology, catalysis, and nanotechnology," Chemical reviews. vol.104, pp. 293-346, 2004.

[7] Chaudhry Q, Scotter M, Blackburn J, Ross B, Boxall A, Castle L, et al. Applications and implications of nanotechnologies for the food sector. Food additives and contaminants. 2008;25(3):241-58.

[8] Mahamuni-Badiger PP, Patil PM, Badiger MV, Patel PR, Thorat-Gadgil BS, Pandit A, et al. Biofilm formation inhibition: Role of zinc oxide-based nanoparticles. Materials Science and Engineering: C. 2020;108:110319.

[9] Siddiqi KS, Ur Rahman A, Tajuddin N, Husen A. Properties of zinc oxide nanoparticles and their activity against microbes. Nanoscale Research Letters. 2018;13:141.

[10] Gudkov SV, Burmistrov DE, Serov DA, Rebezov MB, Semenova AA, Lisitsyn AB. A mini review of the antibacterial properties of ZnO nanoparticles. Frontiers in Physics. 2021;9:641481.

[11] Mendes CR, Dilarri G, Forsan CF, Sapata VdMR, Lopes PRM, de Moraes PB, et al. Antibacterial action and target mechanisms of zinc oxide nanoparticles against bacterial pathogens. Scientific Reports. 2022;12(1):2658.

[12] Frederickson CJ, Koh J-Y, Bush AI. The neurobiology of zinc in health and disease. Nature Reviews Neuroscience. 2005;6(6):449-62.

[13] Król A, Pomastowski P, Rafińska K, Railean-Plugaru V, Buszewski B. Zinc oxide nanoparticles: Synthesis, antiseptic activity and toxicity mechanism. Advances in colloid and interface science. 2017;249:37-52.

[14] Klug A, Rhodes D, editors. Zinc fingers: a novel protein fold for nucleic acid recognition. Cold Spring Harbor symposia on quantitative biology; 1987: Cold Spring Harbor Laboratory Press.

[15] Sabir S, Arshad M, Chaudhari SK. Zinc oxide nanoparticles for revolutionizing agriculture: synthesis and applications. The Scientific World Journal. 2014;2014(1):925494.

[16] Özgür Ü, Alivov YI, Liu C, Teke A, Reshchikov MA, Doğan S, et al. A comprehensive review of ZnO materials and devices. Journal of Applied Physics. 2005;98(4):041301.

[17] Jang JS, Yu C-J, Choi SH, Ji SM, Kim ES, Lee JS. Topotactic synthesis of mesoporous ZnS and ZnO nanoplates and their photocatalytic activity. Journal of Catalysis. 2008;254(1):144-55.

[18] Mahmud S, Johar Abdullah M, Putrus GA, Chong J, Karim Mohamad A. Nanostructure of ZnO fabricated via French process and its correlation to electrical properties of semiconducting varistors. Synthesis and Reactivity in Inorganic and Metal-Organic and Nano-Metal Chemistry. 2006;36(2):155-9.

[19] Gandhi RR, Koche DK. An Insight of Zinc Oxide Nanoparticles (ZnO NPs): Green Synthesis, Characteristics and Agricultural Applications. Biosciences Biotechnology Research Asia. 2024;21(3):863-76.

[20] Atapakala S, Sana SS, Kuppam B, Varma RS, Aly MAS, Kim S-C, et al. Honey-mediated synthesis of zinc oxide nanoparticles, and evaluation of antimicrobial, antibiofilm activities against multidrug-resistant clinical bacterial isolates. Journal of Industrial and Engineering Chemistry. 2024;135:110-21.

[21] Guirguis HA, Youssef N, William M, Abdel-Dayem D, El-Sayed MM. Bioinspired Stevia rebaudiana Green Zinc Oxide Nanoparticles for the Adsorptive Removal of Antibiotics from Water. ACS Omega. 2024;9(11):12881-95.

[22] Song Z, Kelf TA, Sanchez WH, Roberts MS, Rička J, Frenz M, et al. Characterization of optical properties of ZnO nanoparticles for quantitative imaging of transdermal transport. Biomedical Optics Express. 2011;2(12):3321-33.

[23] Wang X, Ding Y, Summers CJ, Wang ZL. Large-scale synthesis of six-nanometer-wide ZnO nanobelts. The Journal of Physical Chemistry B. 2004;108(26):8773-7.

[24] Elabbasy MT, El Bayomi RM, Abdelkarim EA, Hafez AE-SE, Othman MS, Ghoniem ME, et al. Antibacterial and Antibiofilm Activity of Green-Synthesized Zinc Oxide Nanoparticles Against Multidrug-Resistant Escherichia coli Isolated from Retail Fish. Molecules. 2025;30(4):768.

[25] Agarwal H, Menon S, Kumar SV, Rajeshkumar S. Mechanistic study on antibacterial action of zinc oxide nanoparticles synthesized using green route. Chemico-biological interactions. 2018;286:60-70.

[26] Kołodziejczak-Radzimska A, Jesionowski T. Zinc oxide—from synthesis to application: a review. Materials. 2014;7(4):2833-81.

[27] Naveed Ul Haq A, Nadhman A, Ullah I, Mustafa G, Yasinzai M, Khan I. Synthesis approaches of zinc oxide nanoparticles: the dilemma of ecotoxicity. Journal of Nanomaterials. 2017;2017:14.

[28] Ju D, Xu H, Qiu Z, Guo J, Zhang J, Cao B. Highly sensitive and selective triethylamine-sensing properties of nanosheets directly grown on ceramic tube by forming NiO/ZnO PN heterojunction. Sensors and Actuators B: Chemical. 2014;200:288-96.

[29] McLaren A, Valdes-Solis T, Li G, Tsang SC. Shape and size effects of ZnO nanocrystals on photocatalytic activity. Journal of the American Chemical Society. 2009;131(35):12540-1.

[30] Aboulaich A, Balan L, Ghanbaja J, Medjahdi G, Merlin C, Schneider R. Aqueous route to biocompatible ZnSe: Mn/ZnO core/shell quantum dots using 1-thioglycerol as stabilizer. Chemistry of Materials. 2011;23(16):3706-13.

[31] Nagvenkar AP, Deokar A, Perelshtein I, Gedanken A. A one-step sonochemical synthesis of stable ZnO–PVA nanocolloid as a potential biocidal agent. Journal of Materials Chemistry B. 2016;4(12):2124-32.

[32] Chandrasekaran P, Viruthagiri G, Srinivasan N. The effect of various capping agents on the surface modifications of sol–gel synthesised ZnO nanoparticles. Journal of Alloys and Compounds. 2012;540:89-93.

[33] Fakhari S, Jamzad M, Kabiri Fard H. Green synthesis of zinc oxide nanoparticles: a comparison. Green Chemistry Letters and Reviews. 2019;12(1):19-24.

[34] Bandeira M, Giovanela M, Roesch-Ely M, Devine DM, da Silva Crespo J. Green synthesis of zinc oxide nanoparticles: A review of the synthesis methodology and mechanism of formation. Sustainable chemistry and pharmacy. 2020;15:100223.

[35] Yusof HM, Rahman NAA, Mohamad R, Zaidan UH, Samsudin AA. Optimization of biosynthesis zinc oxide nanoparticles: Desirability-function based response surface methodology, physicochemical characteristics, and its antioxidant properties. OpenNano. 2022;8:100106.

[36] Iqbal J, Abbasi BA, Yaseen T, Zahra SA, Shahbaz A, Shah SA, et al. Green synthesis of zinc oxide nanoparticles using Elaeagnus angustifolia L. leaf extracts and their multiple in vitro biological applications. Scientific Reports. 2021;11(1):20988.

[37] Chikkanna MM, Neelagund SE, Rajashekarappa KK. Green synthesis of zinc oxide nanoparticles (ZnO NPs) and their biological activity. SN Applied Sciences. 2019;1:117.

[38] Al-darwesh MY, Ibrahim SS, Mohammed MA. A review on plant extract mediated green synthesis of zinc oxide nanoparticles and their biomedical applications. Results in Chemistry. 2024;7:101368.

[39] Agarwal H, Kumar SV, Rajeshkumar S. A review on green synthesis of zinc oxide nanoparticles–An eco-friendly approach. Resource-Efficient Technologies. 2017;3(4):406-13.

[40] Lahoti R, Carroll D. Green synthesis of zinc oxide nanoparticles and their broad-spectrum

antibacterial activity. Next Research. 2025;2(1):100164.

[41] Mohammadi FM, Ghasemi N. Influence of temperature and concentration on biosynthesis and characterization of zinc oxide nanoparticles using cherry extract. Journal of Nanostructure in Chemistry. 2018;8:93-102.

[42] Uribe-López M, Hidalgo-López M, López-González R, Frías-Márquez D, Núñez-Nogueira G, Hernández-Castillo D, et al. Photocatalytic activity of ZnO nanoparticles and the role of the synthesis method on their physical and chemical properties. Journal of Photochemistry and Photobiology A: Chemistry. 2021;404:112866.

[43] Mohd Yusof H, Mohamad R, Zaidan UH, Abdul Rahman NA. Microbial synthesis of zinc oxide nanoparticles and their potential application as an antimicrobial agent and a feed supplement in animal industry: a review. Journal of Animal Science and Biotechnology. 2019;10:57.

[44] Chauhan R, Reddy A, Abraham J. Biosynthesis of silver and zinc oxide nanoparticles using Pichia fermentans JA2 and their antimicrobial property. Applied nanoscience. 2015;5:63-71.

[45] Al-Zahrani H, El-Waseif A, El-Ghwas D. Biosynthesis and evaluation of TiO2 and ZnO nanoparticles from in vitro stimulation of Lactobacillus johnsonii. J Innov Pharm Biol Sci. 2018;5(1):16-20.

[46] Suba S, Vijayakumar S, Vidhya E, Punitha V, Nilavukkarasi M. Microbial mediated synthesis of ZnO nanoparticles derived from Lactobacillus spp: Characterizations, antimicrobial and biocompatibility efficiencies. Sensors International. 2021;2:100104.

[47] Garmasheva I, Kovalenko N, Voychuk S, Ostapchuk A, Livins'ka O, Oleschenko L. Lactobacillus species mediated synthesis of silver nanoparticles and their antibacterial activity against opportunistic pathogens in vitro. BioImpacts. 2016;6(4):219–23.

[48] Selvarajan E, Mohanasrinivasan V. Biosynthesis and characterization of ZnO nanoparticles using Lactobacillus plantarum VITES07. Materials Letters. 2013;112:180-2.

[49] Chakra PS, Banakar A, Puranik SN, Kaveeshwar V, Ravikumar C, Gayathri D. Characterization of ZnO nanoparticles synthesized using probiotic Lactiplantibacillus plantarum GP258. Beilstein Journal of Nanotechnology. 2025;16(1):78-89.

[50] Salman Z, Taj Al-Deen WR. Biosynthesis of zinc oxide nanoparticles by Lactobacillus casei. Biochemical & Cellular Archives. 2019;19:2259-65.

[51] Iqtedar M, Siddique M, Shahzad A, Kaleem A, Abdullah R. Green Synthesis of zinc oxide nanoparticles by Bacillus subtilis and their use in various applications. Biologia (Lahore). 2024;70(2):66-74.

[52] Shkodenko L, Kassirov I, Koshel E. Metal oxide nanoparticles against bacterial biofilms: Perspectives and limitations. Microorganisms. 2020;8(10):1545.

[53] Al-Tameemi AI, Masarudin MJ, Rahim RA, Mizzi R, Timms VJ, Isa Nm, et al. Eco-friendly zinc oxide nanoparticle biosynthesis powered by probiotic bacteria. Applied Microbiology and Biotechnology. 2025;109(1):32.

[54] Dadi R, Azouani R, Traore M, Mielcarek C, Kanaev A. Antibacterial activity of ZnO and CuO nanoparticles against gram positive and gram negative strains. Materials Science and Engineering: C. 2019;104:109968.

[55] Raghupathi KR, Koodali RT, Manna AC. Size-dependent bacterial growth inhibition and mechanism of antibacterial activity of zinc oxide nanoparticles. Langmuir. 2011;27(7):4020-8.

[56] Manoharan C, Pavithra G, Dhanapandian S, Dhamodaran P, Shanthi B. Properties of spray pyrolised ZnO: Sn thin films and their antibacterial activity. Spectrochimica Acta Part A: Molecular and Biomolecular Spectroscopy. 2015;141:292-9.

[57] Liu Y-j, He L-l, Mustapha A, Li H, Hu Z, Lin M-s. Antibacterial activities of zinc oxide nanoparticles against Escherichia coli O157: H7. Journal of applied microbiology. 2009;107(4):1193-201.

[58] Sánchez-López P, Hernández-Hernández KA, Fuentes Moyado S, Cadena Nava RnD, Smolentseva E. Antimicrobial and virus adsorption properties of Y-Zeolite exchanged with silver and zinc cations. ACS omega. 2024;9(7):7554-63.

[59] Elumalai K, Velmurugan S. Green synthesis, characterization and antimicrobial activities of zinc oxide nanoparticles from the leaf extract of

Azadirachta indica (L.). Applied Surface Science. 2015;345:329-36.

[60] Zhong L, Liu H, Samal M, Yun K. Synthesis of ZnO nanoparticles-decorated spindle-shaped graphene oxide for application in synergistic antibacterial activity. Journal of Photochemistry and Photobiology B: Biology. 2018;183:293-301.

[61] Kashef N, Huang Y-Y, Hamblin MR. Advances in antimicrobial photodynamic inactivation at the nanoscale. Nanophotonics. 2017;6(5):853-79.

[62] Yoo SI, Yang M, Brender JR, Subramanian V, Sun K, Joo NE, et al. Inhibition of amyloid peptide fibrillation by inorganic nanoparticles: functional similarities with proteins. Angewandte Chemie International Edition. 2011;123:5216-21.

[63] El-Telbany M, Mohamed AA, Yahya G, Abdelghafar A, Abdel-Halim MS, Saber S, et al. Combination of meropenem and zinc oxide nanoparticles; antimicrobial synergism, exaggerated antibiofilm activity, and efficient therapeutic strategy against bacterial keratitis. Antibiotics. 2022;11(10):1374.

[64] Udayagiri H, Sana SS, Dogiparthi LK, Vadde R, Varma RS, Koduru JR, et al. Phytochemical fabrication of ZnO nanoparticles and their antibacterial and anti-biofilm activity. Scientific Reports. 2024;14:19714.

[65] Afrasiabi S, Partoazar A. Targeting bacterial biofilm-related genes with nanoparticle-based strategies. Frontiers in Microbiology. 2024;15:1387114.

[66] Ann LC, Mahmud S, Bakhori SKM, Sirelkhatim A, Mohamad D, Hasan H, et al. Antibacterial responses of zinc oxide structures against Staphylococcus aureus, Pseudomonas aeruginosa and Streptococcus pyogenes. Ceramics International. 2014;40(2):2993-3001.

[67] Hassan A, Al-Salmi FA, Saleh MA, Sabatier J-M, Alatawi FA, Alenezi MA, et al. Inhibition mechanism of methicillin-resistant staphylococcus aureus by zinc oxide nanorods via suppresses penicillin-binding protein 2a. ACS Omega. 2023;8(11):9969-77.

[68] Lianga SXT, Wong LS, Lim YM, Djearamanea S, Lee PF. Effects of zinc oxide nanoparticles on Streptococcus pyogenes. South African Journal of Chemical Engineering. 2020;34(1):63-71.

[69] Jiang Y, Zhang L, Wen D, Ding Y. Role of physical and chemical interactions in the antibacterial behavior of ZnO nanoparticles against E. coli. Materials Science and Engineering: C. 2016;69:1361-6.

[70] Lee J-H, Kim Y-G, Cho MH, Lee J. ZnO nanoparticles inhibit Pseudomonas aeruginosa biofilm formation and virulence factor production. Microbiological Research. 2014;169(12):888-96.

[71] Mulani MS, Kamble EE, Kumkar SN, Tawre MS, Pardesi KR. Emerging strategies to combat ESKAPE pathogens in the era of antimicrobial resistance: a review. Frontiers In Microbiology. 2019;10:539.

[72] Meraat R, Ziabari AA, Issazadeh K, Shadan N, Jalali KM. Synthesis and characterization of the antibacterial activity of zinc oxide nanoparticles against Salmonella typhi. Acta Metallurgica Sinica (English Letters). 2016;29:601-8.

[73] Mohamed AA, Abu-Elghait M, Ahmed NE, Salem SS. Eco-friendly mycogenic synthesis of ZnO and CuO nanoparticles for in vitro antibacterial, antibiofilm, and antifungal applications. Biological trace element research. 2021;199(7):2788-99.

[74] Jain D, Shivani, Bhojiya AA, Singh H, Daima HK, Singh M, et al. Microbial fabrication of zinc oxide nanoparticles and evaluation of their antimicrobial and photocatalytic properties. Frontiers in chemistry. 2020;8:778.

[75] Galván Márquez I, Ghiyasvand M, Massarsky A, Babu M, Samanfar B, Omidi K, et al. Zinc oxide and silver nanoparticles toxicity in the baker's yeast, Saccharomyces cerevisiae. PloS one. 2018;13(3):e0193111.

[76] Janaki AC, Sailatha E, Gunasekaran S. Synthesis, characteristics and antimicrobial activity of ZnO nanoparticles. Spectrochimica Acta Part A: Molecular and Biomolecular Spectroscopy. 2015;144:17-22.

[77] Yassin MT, Al-Otibi FO, Al-Askar AA, Elmaghrabi MM. Synergistic anticandidal effectiveness of greenly synthesized zinc oxide nanoparticles with antifungal agents against nosocomial candidal pathogens. Microorganisms. 2023;11(8):1957.

[78] Saxena P, Saharan V, Baroliya PK, Gour VS, Rai MK. Mechanism of nanotoxicity in Chlorella vulgaris exposed to zinc and iron oxide. Toxicology Reports. 2021;8:724-31.

[79] Tang Y, Xin H, Yang S, Guo M, Malkoske T, Yin D, et al. Environmental risks of ZnO nanoparticle exposure on Microcystis aeruginosa: Toxic effects and environmental feedback. Aquatic Toxicology. 2018;204:19-26.

[80] Djearamane S, Lim YM, Wong LS, Lee PF. Cytotoxic effects of zinc oxide nanoparticles on cyanobacterium Spirulina (Arthrospira) platensis. PeerJ. 2018;6:e4682.

[81] Zhu X, Wang J, Cai L, Wu Y, Ji M, Jiang H, et al. Dissection of the antibacterial mechanism of zinc oxide nanoparticles with manipulable nanoscale morphologies. Journal of Hazardous Materials. 2022;430:128436.

[82] Djearamane S, Loh ZC, Lee JJ, Wong LS, Rajamani R, Luque PA, et al. Remedial aspect of zinc oxide nanoparticles against Serratia marcescens and Enterococcus faecalis. Frontiers in Pharmacology. 2022;13:891304.

[83] Wei Y, Wang J, Wu S, Zhou R, Zhang K, Zhang Z, et al. Nanomaterial-based zinc ion interference therapy to combat bacterial infections. Frontiers in Immunology. 2022;13:899992.

[84] Kessler A, Hedberg J, Blomberg E, Odnevall I. Reactive oxygen species formed by metal and metal oxide nanoparticles in physiological media—a review of reactions of importance to nanotoxicity and proposal for categorization. Nanomaterials. 2022;12(11):1922.

[85] Rasheed HM, Aroosh K, Meng D, Ruan X, Akhter M, Cui X. A review on modified ZnO to address environmental challenges through photocatalysis: Photodegradation of organic pollutants. Materials Today Energy. 2024;48:101774.

[86] Baig A, Siddique M, Panchal S. A Review of Visible-Light-Active Zinc Oxide Photocatalysts for Environmental Application. Catalysts. 2025;15(2):100.

[87] Jiang S, Lin K, Cai M. ZnO nanomaterials: current advancements in antibacterial mechanisms and applications. Frontiers in Chemistry. 2020;8:580.

[88] Caron AJ, Ali IJ, Delgado MJ, Johnson D, Reeks JM, Strzhemechny YM, et al. Zinc oxide nanoparticles mediate bacterial toxicity in Mueller-Hinton Broth via Zn2+. Frontiers in Microbiology. 2024;15:1394078.

[89] Mishra YK, Chakravadhanula VSK, Hrkac V, Jebril S, Agarwal DC, Mohapatra S, et al. Crystal growth behaviour in Au-ZnO nanocomposite under different annealing environments and photoswitchability. Journal of Applied Physics. 2012;112(6):064308.

[90] Davaeifar S, Shahabani-Zahiri H, Mohammadi M, Akbari-Noghabi K. Evaluation of the Effect of Zinc Oxide Nanoparticles on the Inhibition of Biofilm formation of standard Pathogenic Bacteria and Comparison with Drug Resistant Isolates. Journal of Ilam University of Medical Sciences. 2019;27(3):138-49.

[91] Jain KK. Drug delivery systems-an overview. Drug delivery systems. 2008;437:1-50.

[92] 92. Agrawal A, Veronica A, Mythreyi R, Gopenath T, Basalingappa KM, Gobianand K. Zinc Oxide Nanoparticles in Disease Diagnosis. Metals in Medicine: Apple Academic Press; 2025. p. 81-117.

[93] Luo Z, Rong P, Yang Z, Zhang J, Zou X, Yu Q. Preparation and Application of Co-Doped Zinc Oxide: A Review. Molecules. 2024;29(14):3373.

[94] Jayaseelan C, Rahuman AA, Kirthi AV, Marimuthu S, Santhoshkumar T, Bagavan A, et al. Novel microbial route to synthesize ZnO nanoparticles using Aeromonas hydrophila and their activity against pathogenic bacteria and fungi. Spectrochimica Acta Part A: Molecular and Biomolecular Spectroscopy. 2012;90:78-84.

[95] Gao Y, Han Y, Cui M, Tey HL, Wang L, Xu C. ZnO nanoparticles as an antimicrobial tissue adhesive for skin wound closure. Journal of Materials Chemistry B. 2017;5(23):4535-41.

[96] Thompson CB, Wiemken TL, Brown TS. Effect of postoperative dressing on excisions performed on the leg: a comparison between zinc oxide compression dressings versus standard wound care. Dermatologic Surgery. 2017;43(11):1379-84.

[97] Jiang J, Pi J, Cai J. The advancing of zinc oxide nanoparticles for biomedical applications. Bioinorganic chemistry and applications. 2018;2018(1):1062562.

[98] Mishchenko T, Mitroshina E, Balalaeva I, Krysko O, Vedunova M, Krysko DV. An emerging role for nanomaterials in increasing immunogenicity of cancer cell death. Biochimica et Biophysica Acta (BBA)-Reviews on Cancer. 2019;1871(1):99-108.

[99] Houšková V, Štengl V, Bakardjieva S, Murafa N, Kalendova A, Opluštil F. Zinc oxide prepared by homogeneous hydrolysis with thioacetamide, its destruction of warfare agents, and photocatalytic activity. The Journal of Physical Chemistry A. 2007;111(20):4215-21.

[100] Agarwal H, Shanmugam V. A review on anti-inflammatory activity of green synthesized zinc oxide nanoparticle: Mechanism-based approach. Bioorganic chemistry. 2020;94:103423.

[101] Nagajyothi PC, Cha SJ, Yang IJ, Sreekanth T, Kim KJ, Shin HM. Antioxidant and anti-inflammatory activities of zinc oxide nanoparticles synthesized using Polygala tenuifolia root extract. Journal of Photochemistry and Photobiology B: Biology. 2015;146:10-7.

[102] Mishra PK, Mishra H, Ekielski A, Talegaonkar S, Vaidya B. Zinc oxide nanoparticles: a promising nanomaterial for biomedical applications. Drug discovery today. 2017;22(12):1825-34.

[103] Wang Y, Song S, Liu J, Liu D, Zhang H. ZnO-functionalized upconverting nanotheranostic agent: multi-modality imaging-guided chemotherapy with on-demand drug release triggered by pH. Angewandte Chemie International Edition. 2015;54(2):536-40.

[104] Eixenberger JE, Anders CB, Wada K, Reddy KM, Brown RJ, Moreno-Ramirez J, et al. Defect engineering of ZnO nanoparticles for bioimaging applications. ACS applied materials & interfaces. 2019;11(28):24933-44.

[105] Umrani RD, Paknikar KM. Zinc oxide nanoparticles show antidiabetic activity in streptozotocin-induced Type 1 and 2 diabetic rats. Nanomedicine. 2014;9(1):89-104.

[106] El-Gharbawy RM, Emara AM, Abu-Risha SE-S. Zinc oxide nanoparticles and a standard antidiabetic drug restore the function and structure of beta cells in Type-2 diabetes. Biomedicine & Pharmacotherapy. 2016;84:810-20.

[107] Mohandas A, PT SK, Raja B, Lakshmanan V-K, Jayakumar R. Exploration of alginate hydrogel/nano zinc oxide composite bandages for infected wounds. International journal of nanomedicine. 2015;10(sup2):53-66.

[108] Augustine R, Dominic EA, Reju I, Kaimal B, Kalarikkal N, Thomas S. Investigation of angiogenesis and its mechanism using zinc oxide nanoparticle-loaded electrospun tissue engineering scaffolds. Rsc Advances. 2014;4(93):51528-36.

[109] Ghareib M, Abu Tahon M, Abdallah WE, Hussein M. Free radical scavenging activity of zinc oxide nanoparticles biosynthesised using Aspergillus carneus. Micro & Nano Letters. 2019;14(11):1157-62.

[110] Marin-Flores CA, Rodríguez-Nava O, García-Hernández M, Ruiz-Guerrero R, Juárez-López F, de Jesús Morales-Ramírez A. Free-radical scavenging activity properties of ZnO sub-micron particles: size effect and kinetics. Journal of Materials Research and Technology. 2021;13:1665-75.

[111] Rossi S, Marciello M, Sandri G, Ferrari F, Bonferoni MC, Papetti A, et al. Wound dressings based on chitosans and hyaluronic acid for the release of chlorhexidine diacetate in skin ulcer therapy. Pharmaceutical development and technology. 2007;12(4):415-22.

[112] Zhang R, Carlsson F, Edman M, Hummelgård M, Jonsson BG, Bylund D, et al. Escherichia coli bacteria develop adaptive resistance to antibacterial ZnO nanoparticles. Advanced Biosystems. 2018;2(5):1800019.

[113] Dey S, lochan Mohanty D, Divya N, Bakshi V, Mohanty A, Rath D, et al. A critical review on zinc oxide nanoparticles: Synthesis, properties and biomedical applications. Intelligent Pharmacy. 2024;3(1):53-70.

[114] Mondal SK, Chakraborty S, Manna S, Mandal SM. Antimicrobial nanoparticles: current landscape and future challenges. RSC Pharmaceutics. 2024;1:388-402.

[115] Strekalovskaya EI, Perfileva AI, Krutovsky KV. Zinc oxide nanoparticles in the "Soil–Bacterial Community–Plant" system: Impact on the stability of soil ecosystems. Agronomy. vol. 14, pp.1588, 2024.

[116] Salmani-Zarchi H, Mousavi-Sagharchi SMA, Sepahdoost N, Ranjbar-Jamalabadi M, Gross JD, Jooya H, et al. "Antimicrobial Feature of Nanoparticles in the Antibiotic Resistance Era: From Mechanism to Application," Advanced Biomedical Research. vol. 13, pp.113, 2024.

[117] Irede EL, Awoyemi RF, Owolabi B, Aworinde OR, Kajola RO, Hazeez A, et al. "Cutting-edge developments in zinc oxide nanoparticles: synthesis and applications for enhanced antimicrobial and UV protection in healthcare solutions," RSC Advances. vol. 14, pp. 20992-21034, 2024.

THIS PAGE IS INTENTIONALLY LEFT BLANK.

IJBBE International Journal of Biophotonics & Biomedical Engineering Vol. 5, No. 1, Spring-Summer, 2025

Research Article

Optical biosensor for detection of hemoglobin using ternary photonic crystals

M. Aghamohammadian [a], A. Vahedi[*, b], and S. Haghipour [a]

[a] Department of Medicine Engineering, Ta.C., Islamic Azad University, Tabriz, Iran
[b] Department of Physics, Ta.C., Islamic Azad University, Tabriz, Iran

***Corresponding Author Email: minooaghamohammadian74@gmail.com**

DOI: 10.71498/ijbbe.2025.1193386

ABSTRACT

Received: Dec. 13, 2024, Revised: May. 16, 2025, Accepted: May. 28, 2025, Available Online: Jul. 24, 2025

Optical biosensors have attracted the attention of researchers because they have a unique ability to control the dispersal of photons and detect the natural shape of biomolecules. The main component of blood is hemoglobin, whose main function is to transport oxygen to body tissues and remove carbon dioxide from them. This article aims to simulate biosensors that can detect hemoglobin concentration using photonic crystals. For this purpose, we have used two structures with $TiN/m/TiO_2$ and $Al_XGa_{1-X}N/m/TiO_2$. The m layer is a dielectric such as glass or air, which has a different refractive index and can control light transmittance. Photonic crystals have a region called the photonic band gap (PBG), in which waves cannot propagate in the structure. layers inside the photonic crystal structure controlled and adjusted the defect modes and PBG properties. To find the best result, parameters such as the layer thickness, the light incident angle, and the refractive index have been optimally selected. After examining the proposed structures, it was determined that both structures are more optimal in a wide defect layer. The results show that the $TiN/m/Al_XGa_{1-X}N$ structure has optimum sensitivity (S=780.0 nm/RIU), relative sensitivity (S_R=0.729), and figure of merit (FOM=780.01/RIU) at a selected wavelength range.

KEYWORD

Hemoglobin، Photonic Crystal،Transfer Matrix Method، Optical Biosensor

I. INTRODUCTION

The peculiar features of the photonic crystal (PhC)–structure are photonic band gaps and photon localization. The photonic band gap (PBG) is the frequency range where light of certain wavelengths cannot pass through the structure. These characteristics are the result of periodic modulation of dielectric functions, which significantly changes the spectrum of electromagnetic waves passing through it [1-3]. The photonic band gap in photonic crystals depends on the refractive index and thickness of the layers, the period of the photonic crystal, and the incident angle (and polarization) of light. PhC structures are the new technology for biosensor applications. Optical biosensors are considered analytical detectors that convert chemical, physical, or biological interactions into an optical signal. To use PhC as a

biosensor, it is crucial to change its structural arrangement to produce a resonant or defect mode in the transmission spectrum. The best way to form such a resonance mode is to create defects in the structure. Based on this, many optical devices such as optical filters, switchers, and photonic crystal fibers are produced [4-6]. PhC-based biosensors can detect biotoxins, veterinary drugs, microorganisms, pesticide residues, excessive additives, heavy metal compounds, and environmental pollutants [7-13]. Hemoglobin (Hb) is the most vital component of blood, which is mainly responsible for transporting oxygen from the lungs to different body tissues and returning carbon dioxide from the tissues to the lungs. Any deviation in the blood hemoglobin concentration leads to fatal diseases, Such as polycythemia, anemia, diabetes, and thyroid dysfunction. Detection of blood hemoglobin concentration is one of the most serious and challenging concerns of medical scientists and researchers. The resonance slope in the spectrum and its change with hemoglobin concentration are the basis of our sensor design [7, 14, 15].

In recent years, further work has been done on a PhC for hemoglobin detection. El-Khozondar et al. developed a one-dimensional ternary PhC structure for hemoglobin measurement from 0 g/L to 50 g/L concentration range, and the authors achieved a reported measurement of 46/51 nm/RIU [16] A.K. Goyal et al. recently investigated a defective PhC based on the Bloch surface. By entering samples in defect regions with different concentrations, the authors calculated the angular shift and thus obtained a result of 69 deg./RIU. [17]. J. Hao and her team designed a superconductor-based, one-dimensional PhC refractive index sensor to measure different concentrations of hemoglobin in human blood, with a sensitivity of 6.85 and 6.48 μm/RIU at 80 K and 134 K [18]. Goyal et al. studied the reflectance of a one-dimensional PhC incorporating a porous defect layer for hemoglobin detection. The authors concluded the optimal sensitivity of 323 nm/RIU and FOM of 517 1/RIU, respectively [19]. H.A. Elsayed et al. reported a one-dimensional binary hemoglobin PhC sensor in which the authors used TMM to measure the shift in the resonance peak with respect to different hemoglobin concentrations and achieved a sensitivity of 167 nm/RIU [20]. Recently, K. M. Abohassan and his team have extensively investigated one-dimensional PhC structures by studying the reflection properties via TMM for various biosensing applications. [21-24].

In this work, we designed and simulated a highly sensitive biosensor structure based on 1D-PhC with a defect layer. We calculate the transmission of polarized light (s) using the transmission matrix method (TMM) to measure the transmission of the mentioned structures and study the effect of some parameters to achieve the highest performance of the sensor configuration. The proposed sensor is efficient in measuring hemoglobin concentration. Various parameters such as figure of merit index (FOM), sensitivity (S), and full width at half maximum (FWHM) have been introduced to evaluate and compare the performance of biosensors. These parameters are numerically derived and are comparable with many of the reported values of photonic crystal-based biosensors [25-30].

II. METHOD

A schematic diagram of our proposed biosensor based on a one-dimensional defect PhC is shown in Fig. 1.

Fig. **1** Schematic representation of biophotonic sensor structure

In our design, the periodic structure consistsf three different dielectri terials abeled th thickness d_1, dm, d_2 and refractive index $n_1, , n_m$ and n_2 respectively. Ternary one-dimensional structures have more exactly controlled photonic band gaps compared to binary structures. The N and D are the periodic

layer numbers and the defect layer with thickness d_l and refractive index n_l. The PhC structure is surrounded by a substrate (S) layer at one end and air at the other. The surrounding medium and PhC determine the physical and optical characteristics of the biosensor. The transfer matrix method can be used to analyze the reflectance or transmittance properties. According to Abel's theory, the periodic structure matrix of one layer, for example (a) layer, can be described by $F(a)$ matrix, [31-33].

$$F(a) = \begin{pmatrix} g_{11} & g_{12} \\ g_{21} & g_{22} \end{pmatrix} \quad (1)$$

Elements g_{11}, g_{12}, g_{21} and g_{22} represented by:

$$g_{11} = cos\,\delta_1\, cos\,\delta_2 - \frac{p_2}{p_1}\, sin\,\delta_1 \quad (2)$$

$$g_{12} = \frac{-i}{p_1} sin\,\delta_1\, cos\,\delta_2 - \frac{i}{p_2} cos\,\delta_1\, sin\,\delta_2 \quad (3)$$

$$g_{21} = -ip_1\, sin\,\delta_1\, cos\,\delta_2 - ip_2\, cos\,\delta_1\, sin\,\delta_2 \quad (4)$$

$$g_{22} = cos\,\delta_1\, cos\,\delta_2 - \frac{p_1}{p_2}\, sin\,\delta_1\, sin\,\delta_2 \quad (5)$$

That:

$$\delta_1 = \frac{2\pi d_1}{\lambda} n_1\, cos\,\theta_1$$

$$\delta_2 = \frac{2\pi d_2}{\lambda} n_2\, cos\,\theta_2 \quad (6)$$

$$p_1 = n_1\, cos\,\theta_1$$

$$p_2 = n_2\, cos\,\theta_2 \quad (7)$$

And for period N, the matrix is:

$$F(Na) = \begin{pmatrix} F_{11} & F_{12} \\ F_{21} & F_{22} \end{pmatrix} \quad (8)$$

$$F_{11} = g_{11} u_{N-1}(\Psi) - u_{N-2}(\Psi) \quad (9)$$

$$F_{12} = g_{12} u_{N-1}(\Psi) \quad (10)$$

$$F_{21} = g_{21} u_{N-1}(\Psi) \quad (11)$$

$$F_{22} = g_{22} u_{N-1}(\Psi) - u_{N-2}(\Psi) \quad (12)$$

$$\Psi = \frac{1}{2}(g_{11} + g_{22}) \quad (13)$$

$$u_N(\Psi) = \frac{(sin(N+1)\, cos^{-1}\Psi)}{\sqrt{1-\Psi^2}} \quad (14)$$

In the next step, the defect matrix (D) was employed:

$$D(d_d) = \begin{bmatrix} cos\,\delta_d & \frac{-i}{p_d} sin\,\delta_d \\ -ip_d\, sin\,\delta_d & cos\,\delta_d \end{bmatrix} \quad (15)$$

were:

$$\delta_d = \frac{2\pi d_d}{\lambda} n_d\, cos\,\theta_d$$

$$p_d = n_d\, cos\,\theta_d \quad (16)$$

The total characteristic matrix is the product of three matrices:

$$M(\omega) = (M_a M_m M_b)^N M_D (M_b M_m M_a)^N$$

$$M = \begin{pmatrix} M_{11} & M_{12} \\ M_{21} & M_{22} \end{pmatrix} \quad (17)$$

Where the first one $(MaMmMb)^N$ describes the periodic structure on the left, and the last one $(MbMmMa)^N$ describes the periodic structure on the right, and between them, there is a defect layer matrix denoted by M_D. From these three matrices, we obtain the entire characteristic matrix of the structure, which allows us to calculate the reflection and transition coefficient (r).

$$r = \frac{(M_{11} + M_{12})j_0 - (M_{21} + M_{22})}{(M_{11} + M_{12})j_0 + (M_{21} + M_{22})} \quad (18)$$

That:

$$j_0 = \sqrt{\frac{\varepsilon_0}{\mu_0}} n_0\, cos\,\theta_0 \quad (19)$$

Finally, reflectance and transmittance are represented by:

$$R=r^2 \quad (20)$$

$$T = t^2 = 1 - r^2 \quad (21)$$

we have used glass as a substrate with refractive index $n_s = 1.524$. In a perfect, defect-free photonic crystal, it is observed a pure band gap, and when a defect is introduced, it leads to the localization of the defect states and a certain mode in the reflection spectrum is obtained. An example of the defect introduced is a hemoglobin solution. Different concentrations of the refractive index of hemoglobin solution depend on its concentration, and these changes are taken from a model function from reference [34]. The efficiency of the sensor is an important factor that determines sensitivity, which can be calculated from the following equation.

$$S = \frac{\Delta \lambda_{res}}{\Delta n} \quad (22)$$

The FOM is obtained by considering the ratio of the S to the FWHM.

$$FOM = \frac{S}{\text{FWHM}} \quad (23)$$

The quality factor is also calculated from the following formula:

$$Q = \frac{RF}{\text{FWHM}} \quad (24)$$

III. Conclusion

A. *Structure 1*

The first part aims to find the optimal state of the TiN/m/Ti O_2 layer. We use an optical biosensor based on a one-dimensional photonic crystal to detect the hemoglobin concentration. In the first part, da(TiN)=100, db(TiO_2) = 109 *and dm* thicknesses are 0, 60 and100 nm, N=3, 5, 7, 9 and dl= 2, 5, 10 μm were assumed for the number of ternary layers and the thickness of the defect layer, respectively. TiN is a metal-semiconductor composed of Titanium and Nitrogen. This chemical compound is used as a resilient coating on the surfaces of sensors due to its favorable optical properties, mechanical strength, exclusive electronic properties, and structural robustness [35]. An obtained state will be optimal if the obtained mode has a higher height, a sharper width, and a band gap with maximum width. Below, we will check the results obtained for different N and dm to find the optimal state for these variables. To carry out this research, we consider 0.0001 accuracy in all three cases. [36-38] The refractive index of hemoglobin was considered 1.380 and 1.365 in wavelength range 820 to 1300 nm [21, 39].

B. *Results of structure 1*

Fig. 2 represents the intensity of transmitted light of TiN/m/TiO_2 structure for a different number of periods N.

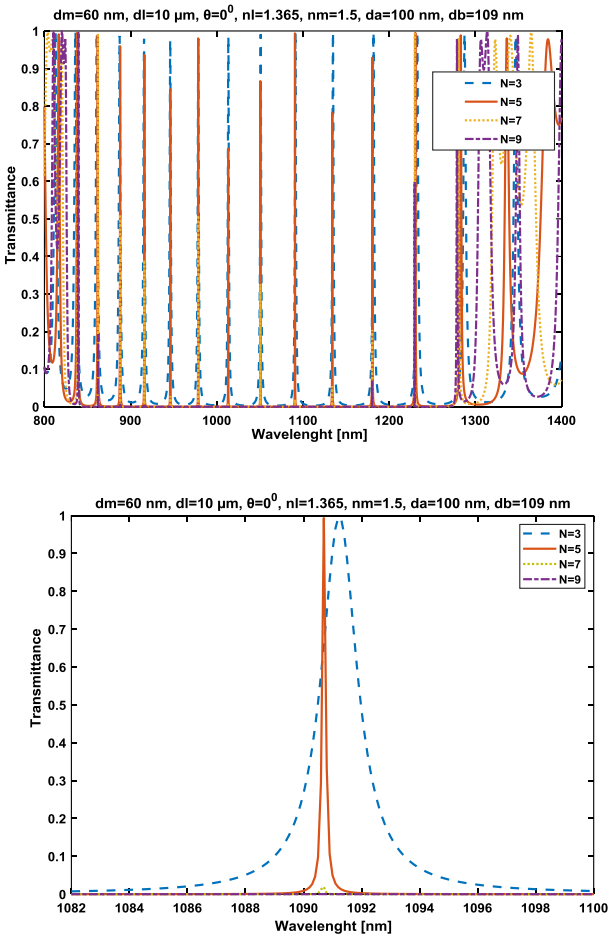

Fig. **2** Optimizing the number of periods (N) concerning wavelength. a: The effect of the number of triple layers (N), b: The height and width of the peaks

The result of Fig. 2 and numerical calculations shows that the system has a good bandgap width, and N=5 is the optimum state. Because at this value, the optimal situation is that more height and sharper width, and a band gap with maximum width are possible. Fig. 3 shows the transmitted light intensity for different values of dl =2 , 5 and 10 μm.

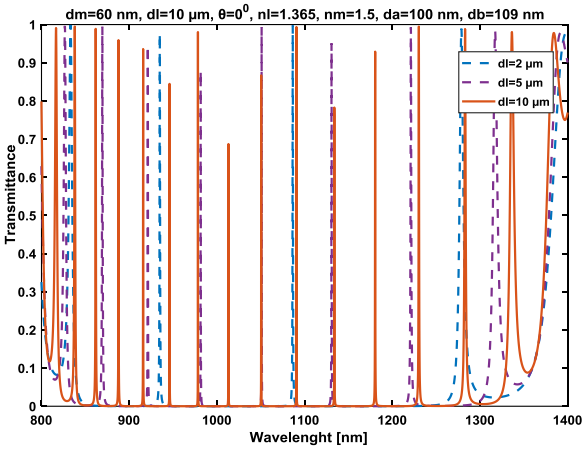

Fig. **3** Transmitted light intensity for dl =2 , 5 and 10 μm

Figure. 3 shows that the number of modes increases and the intensity of some modes decreases with increasing defect layer thicknesses. Table 1 shows the numerical calculations for different values of dl for the refractive index of hemoglobin. The parameters RW and $S_R = \frac{S}{RW}$ are the wavelengths of the peak of the defect mode (resonant wavelength) and relative or dimensionless sensitivity, respectively.

Table **1** Numerical calculations for dl = 2 , 5 and 10 μm for hemoglobin (structure 1).

$dl(\mu m)$	RW (nm)	S (nm /RIU)	S_R	FOM (1/RIU)
2	1087.0	546.7	0.53	364.5
5	1051.0	698.3	0.69	465.5
10	1091.0	780.0	0.73	780.0

As it is clear that, dl=10 μm is optimal due to the appropriate peak size and considering other effective components (band gap, width, sensitivity, etc.). The table denotes that dl=10 μm has optimum sensitivity (S=780.0 nm/RIU), relative sensitivity (S_R=0.729) and figure of merit (FOM=780.01/RIU) at resonance wavelength RF=1091.0 nm respectively. Fig. 4 shows the results obtained with different light incident angles θ. According to the previous sections, here we also calculated the results numerically.

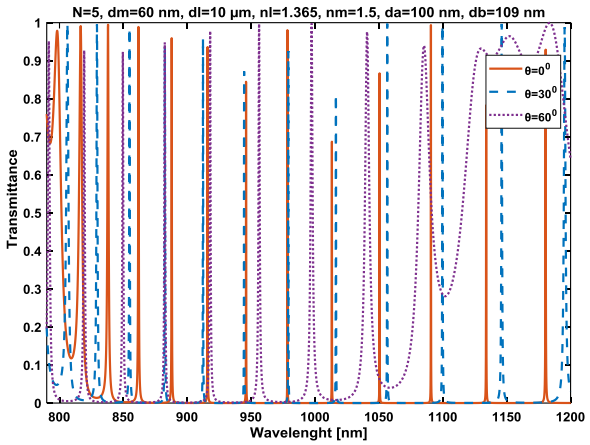

Fig. **4** Transmitted light intensity for $\theta = 0^0$, 30^0, 60^0 degrees

As the angle increases, the width of the modes increases, such that at an angle of 60 degrees, a small band gap with wide modes is produced. By examining these results, θ=0° is the most optimal possible mode. While the light incident is tuned to $\theta = 0^0$, the structure has a vast band gap and narrow, sharp modes. It can be observed from Fig. 5 that minor changes in the refractive index of hemoglobin can appropriately shift the mode.

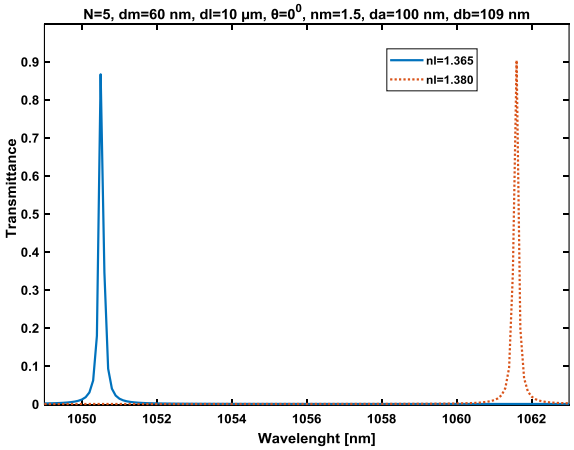

Fig. **5** Mode shifts of biosensor in two different hemoglobin refractive indices (nl)

In this part of the work, the effect of the refractive index of the middle layer (nm) is investigated. For comparison, we considered the values of 1, 1.5, 2, and 2.5.

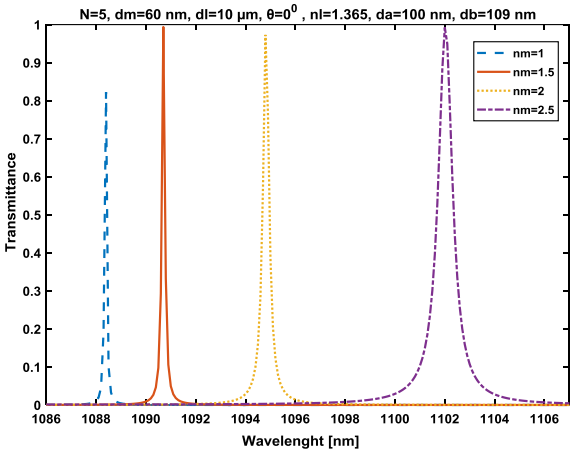

Fig. **6** Transmitted light intensity for different refractive indices of the middle layer (nm)

Figure. 6 shows that the glass layer (nm=1.5) is the most optimal possible state. On the other hand, the structure could be practically fabricated based on glass, and such a structure would be easier to access scientifically. In Fig. 7, we considered the thicknesses of the middle layer values of 0, 60, and 120 nm.

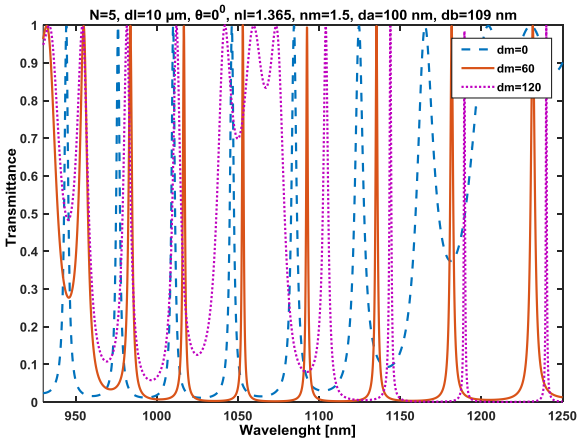

Fig. **7** The effect of thicknesses of the middle layer (dm)

Our analysis shows that dm = 60 is the most optimal state. According to the obtained results, the important parameters such as the width of the band gap, FWHM, resonance wavelength, quality factor, sensitivity, and FOM are 466.8 nm, 2 nm, 1181 nm, 590.5, 800 nm/RIU and 400, respectively.

C. *structure 2*

In this section, instead of layer a (TiN), in the first section, the $Al_XGa_{1-X}N$ layer was replaced. Aluminum Gallium Nitride is a III-Nitride semiconductor. This process alters the chemical composition by changing the ratios of aluminum (Al), gallium (Ga), and nitrogen (N). This flexibility allows for the tuning of its optical and electronic properties. The visual characteristics of $Al_xGa_{1-x}N$ semiconductor quantum dots can be altered by varying the composition percentages of Al and Ga. Introducing these quantum dots into the biosensor can allow for the modification of optical characteristics, thereby enhancing key biosensor features such as sensitivity, figure of merit, and quality factor. The obtained state ($Al_XGa_{1-X}N$/m/ TiO_2) will be optimal if the obtained mode has a higher height, a sharper width, and a band gap with the maximum width [40-42].

D. *Results of structure 2*

The important parameters in this section that should be determined are the fraction of aluminum composition (x), and some important parameters were investigated in section B. First, we examined the changes of x for x=0, 0.4, 0.8, and 1. Fig. 8 shows that a band gap only in the case of x=1 is suitable and wider than other values, because the peak corresponding to this value is narrower and the mode is thinner.

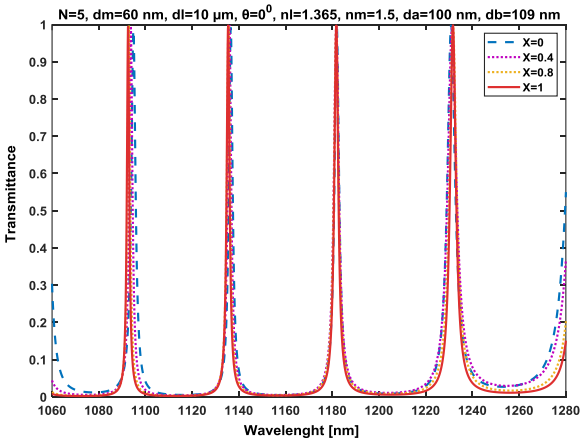

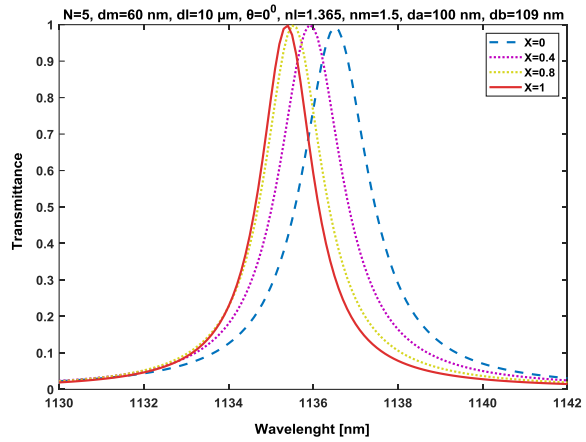

Fig. **8** (a) Transmittance for different values of aluminum fraction (x). (b) Shifts of modes by changing the aluminum fraction x

Figure. 9 shows the transmission spectrum of the biosensor concerning the thickness of the defect layer. In this structure, such as structure 1, it is clear that dl=10μm is the suitable selection, as shown in Fig. 9:

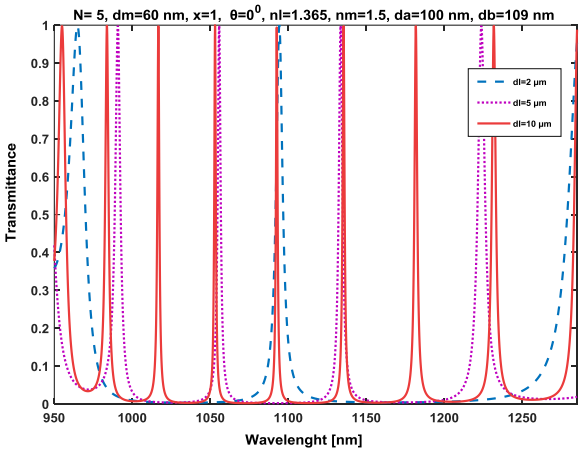

Fig. **9** Intensity of light passing through the biosensor according to the thickness of different defect layers

Figure. 10 shows some optimized modes located at approximately 1055 and 1095 nm. These modes have appropriate intensity and FWHM for detection purposes.

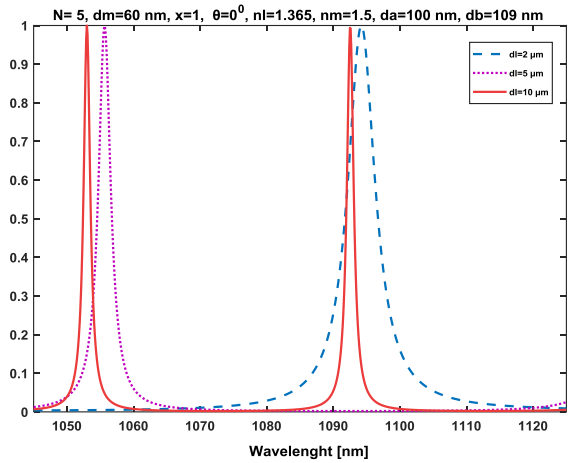

Fig. **10** Some optimized local modes in dl=10 μm.

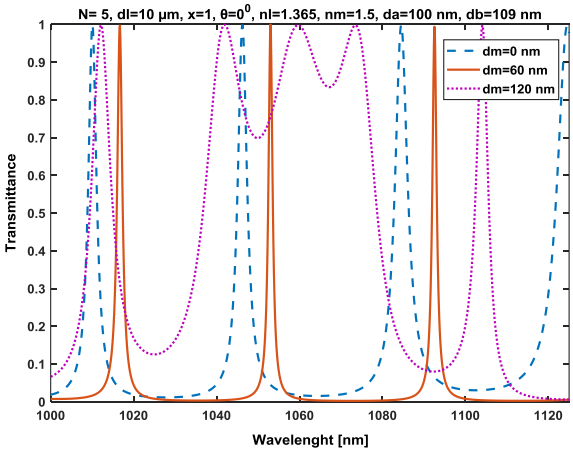

Fig. **11** The effect of thicknesses of the middle layer (dm)

As can be deduced from Fig. 11, the 60 nm thickness is optimal for structure 2. Fig. 12 shows the intensity of light passing through the biosensor according to the hemoglobin refractive index.

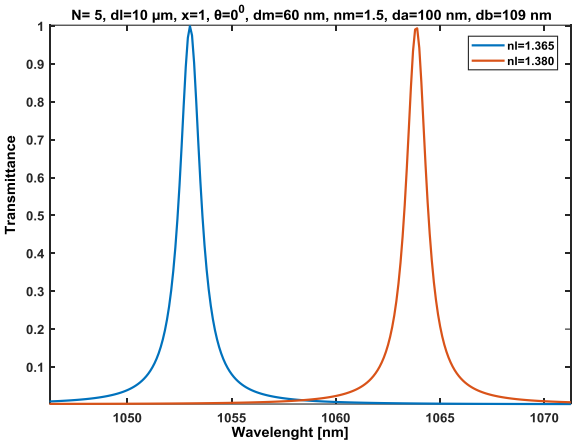

Fig. **12** the effect of thicknesses of the middle layer (dm)

Table 2 shows the numerical calculations for different values of dl for the refractive index of hemoglobin.

Table **2** Numerical calculations for dl = 2 , 5, 10 μm for hemoglobin (structure 2).

$dl(\mu m)$	RF (nm)	S $(nm$ /RIU)	S_R	FOM (1/RIU)
2	1094.0	600.0	0.55	300.0
5	1134.0	733.3	0.64	183.3
10	1135.0	800.0	0.70	400.0

Figure 13 shows the comparison of sensitivity and FOM values for different thicknesses of the two structures.

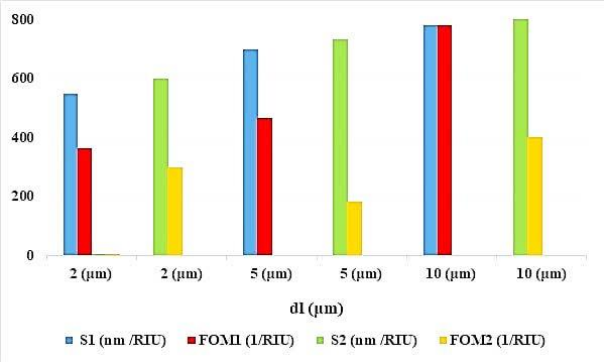

Fig. **13** The comparison of sensitivity and FOM values for different thicknesses of two structures.

The simulated biosensor exhibits sensitivity to refractive index variations of hemoglobin through apparent variations in the bandgap region, mode characteristics, and value of detection parameters. We have analyzed articles from various references to evaluate and compare the results obtained from the proposed structure. Table 3 demonstrates the sensing performance parameters of our biosensor compared to those reported in previous studies in wavelength range (WR).

Table 3. Assessing the sensitivity of the suggested sensor in comparison to other biosensing designs.

WR(nm)	S (nm /RIU)	FOM (1/RIU)	REFERENCE)
800-1200	46.51	-	[16]
2300-3100	6480	-	[18]
1630-1644	323	517	[17]
590-650	167	0.63	[20]
480-1800	1962	10916	[7]
950-1300	800	400	THIS WORK

Discussions

In this paper, we have established the theoretical studies of the ternary 1D-photonic crystal biosensor that enables enhanced sensitivity to small changes in the refractive index, to detect hemoglobin. Based on the presented findings, the proposed method has several advantages, including the ability to facilitate detection by increasing performance parameters, selecting optimal mode heights, and observing the effects of quantum dots, gallium nitride. Two similar structures were investigated, which, by using quantum dots instead of TiN layers, increased the sensitivity. Investigation shows that the photonic band gaps have sharp and suitable detection modes. This structure has suitable performance parameters such as Sensitivity, Figure of Merit, and Wavelength Ranges of 800 nm/RIU, 400, and 950 -1350 nm, respectively. We distinguished two hemoglobin samples. These efforts will advance future research and enhance knowledge in this field.

REFERENCES

[1] John, S. "Localization of light: Theory of photonic band gap materials," in Photonic band gap materials. Springer. pp. 563-665, 1996.

[2] CM, B. "Development and application of materials exhibiting photonic band gaps," J. Opt. Soc. Am. B, vol. **10**, pp. 280-413, 1993.

[3] John, S., H. Sompolinsky, and M.J. Stephen, "Localization in a disordered elastic medium near two dimensions," Physical Review B, vol. **27**, pp. 5592, 1983.

[4] Ďuriška, L., et al., Aqueous corrosion of aluminum-transition metal alloys composed of structurally complex phases: A review. Materials, 2021. **14**(18): p. 5418.

[5] Ghasemi, F. and S. Razi, Novel photonic bio-chip sensor based on strained graphene sheets for blood cell sorting. Molecules, 2021. **26**(18): p. 5585.

[6] Kong, W., et al., Wavelength manipulation in a grating metasurface loaded Bloch surface wave structure. Results in Physics, 2021. **27**: p. 104496.

[7] Firouzi, F., A. Vahedi, and S. Hagipour, Ternary one-dimensional photonic crystal biosensors for efficient bacteria detection: Role of quantum dots and material combinations. Physica B: Condensed Matter, 2025. **698**: p. 416766.

[8] Daher, M.G., et al., Design of a novel optical sensor for the detection of waterborne bacteria based on a photonic crystal with an ultra-high sensitivity. Optical and Quantum Electronics, 2022. **54**(2): p. 108.

[9] Taya, S.A., et al., Highly sensitive nano-sensor based on a binary photonic crystal for the detection of mycobacterium tuberculosis bacteria. Journal of Materials Science: Materials in Electronics, 2021. **32**: p. 28406-28416.

[10] Mohamed, A.M., et al., Design of a 1D PhC biosensor with enhanced sensitivity based on useful features provided for the detection of waterborne bacteria. Optical and Quantum Electronics, 2024. **56**(3): p. 433.

[11] Aly, A.H., et al., MATLAB simulation based study on poliovirus sensing through one-dimensional photonic crystal with defect. Scientific Reports, 2023. **13**(1): p. 9422.

[12] Meradi, K.A., et al., Optical biosensor based on enhanced surface plasmon resonance: theoretical optimization. Optical and Quantum Electronics, 2022. **54**(2): p. 124.

[13] Malek, C., et al., High performance biosensor composed of 1D defective photonic crystal for sensing and detection of distinguished blood components. Optical and Quantum Electronics, 2023. **55**(3): p. 196.

[14] Qu, W., et al., Application of Optical Fiber Sensing Technology and Coating Technology in Blood Component Detection and Monitoring. Coatings, 2024. **14**(2): p. 173.

[15] Su, M., et al., Tamm-plasmon-polariton biosensor based on one-dimensional topological photonic crystal. Results in Physics, 2023. **48**: p. 106454.

[16] El-Khozondar, H.J., et al., Design of one dimensional refractive index sensor using 40

[17] ternary photonic crystal waveguide for plasma blood samples applications. Physica E: Low-dimensional Systems and Nanostructures, 2019. **111**: p. 29-36.

[18] Goyal, A.K. and S. Pal, Design analysis of Bloch surface wave based sensor for haemoglobin concentration measurement. Applied Nanoscience, 2020. **10**: p. 3639-3647.

[19] Hao, J.-J., et al., Research on low-temperature blood tissues detection biosensor based on one-dimensional superconducting photonic crystal. Communications in Nonlinear Science and Numerical Simulation, 2020. **89**: p. 105299.

[20] Goyal, A.K., Design analysis of one-dimensional photonic crystal based structure for hemoglobin concentration measurement. Progress In Electromagnetics Research M, 2020. **97**: p. 77-86.

[21] Abadla, M.M. and H.A. Elsayed, Detection and sensing of hemoglobin using one-dimensional binary photonic crystals comprising a defect layer. Applied optics, 2020. **59**(2): p. 418-424.

[22] Abohassan, K.M. and H.S. Ashour, Demultiplexers for DWDM applications using one-dimensional planar binary photonic crystals defected with ZnS x Se1-x ternary alloys. Journal of Nanophotonics, 2022. **16**(1): p. 016006-016006.

[23] Abohassan, K.M., H.S. Ashour, and M.M. Abadla, A 1D binary photonic crystal sensor for detecting fat concentrations in commercial milk. RSC Advances, 2021. **11**(20): p. 12058-12065.

[24] Yashaswini, P.R., et al., Design and simulation of a highly sensitive one-dimensional photonic

crystal for different chemical sensing applications. Results in Optics, 2023. **11**: p. 100376.

[25] Ashour, H.S., K.M. Abohassan, and M.M. Abadla, Defective 1D quinary photonic crystal sensors for the detection of cancerous blood cells. Optical Engineering, 2021. **60**: p. 127106 - 127106.

[26] Al-Dossari, M., et al., Bio-Alcohol Sensor Based on One-Dimensional Photonic Crystals for Detection of Organic Materials in Wastewater. Materials, 2022. **15**(11): p. 4012.

[27] Kuliešaitė, M., et al., Partially coherent UV–VIS light generation in photonic crystal fiber using femtosecond pulses. Results in Physics, 2021. **31**: p. 104965.

[28] Mostafa, T., A. Ahmed, and E.-S. El-Rabie, Photonic crystal analog to digital converter a literature review, challenges, and some novel trends. Menoufia Journal of Electronic Engineering Research, 2022. **31**(2): p. 64-74.

[29] Rao, D.G.S., S. Swarnakar, and S. Kumar, Design of photonic crystal based compact all-optical 2× 1 multiplexer for optical processing devices. Microelectronics Journal, 2021. **112**: p. 105046.

[30] Zaky, Z.A. and A.H. Aly, Gyroidal graphene/porous silicon array for exciting optical Tamm state as optical sensor. Scientific Reports, 2021. **11**(1): p. 19389.

[31] Mohammed, N.A., et al., Tuberculosis biomedical sensor based on on-chip nanocavity 2D photonic crystal with high sensitivity and quality factor. Measurement, 2023. **222**: p. 113595.

[32] Patel, S.K., et al., Design of graphene metasurface based sensitive infrared biosensor. Sensors and Actuators A: Physical, vol. **301**, pp. 111767, 2020.

[33] Ramanujam, N., et al., Design of one dimensional defect based photonic crystal by composited superconducting material for bio sensing applications. Physica B: Condensed Matter, vol. **572**, pp. 42-55, 2019.

[34] White, I.M. and X. Fan, On the performance quantification of resonant refractive index sensors. Optics express, vol. **16**, pp. 1020-1028, 2008.

[35] Marmarou, A., et al. In vivo measurement of brain water by MRI. in Brain Edema VIII: Proceedings of the Eighth International Symposium, Bern, June 17–20, 1990. 1990. Springer.

[36] Del Villar, I., et al., Nano-Photonic Crystal D-Shaped Fiber Devices for Label-Free Biosensing at the Attomolar Limit of Detection. Adv Sci (Weinh), 2024. **11**(35): p. e2310118.

[37] Shaban, M., et al., Tunability and sensing properties of plasmonic/1D photonic crystal. Scientific reports, 2017. **7**(1): p. 41983.

[38] Panda, A. and P.D. Pukhrambam, Investigation of defect based 1D photonic crystal structure for real-time detection of waterborne bacteria. Physica B: Condensed Matter, 2021. **607**: p. 412854.

[39] Wang, P., et al., MXene/metal–organic framework based composite coating with photothermal self-healing performances for antifouling application. Chemical Engineering Journal, 2023. **474**: p. 145835.

[40] Chakaya, J., et al., The WHO Global Tuberculosis 2021 Report–not so good news and turning the tide back to End TB. International Journal of Infectious Diseases, 2022. **124**: p. S26-S29.

[41] Aly, A.H., et al., Novel biosensor detection of tuberculosis based on photonic band gap materials. Materials Research, 2021. **24**: p. e20200483.

[42] Altug, H., et al., Advances and applications of nanophotonic biosensors. Nature nanotechnology, vol. **17**, pp. 5-16, 2022.

[43] Lazareva, E.N. and V.V. Tuchin, "Measurement of refractive index of hemoglobin in the visible/NIR spectral range," Journal of biomedical optics, vol. **23**, pp. 035004-035004, 2018.

IJBBE International Journal of Biophotonics & Biomedical Engineering Vol. 5, No. 1, Spring-Summer, 2025

Review Article

Identifying Autism from EEG Signals Using Features Derived from Active Brain Source Models

M. Rajabioun*

*Mamaghan Branch, Islamic Azad University, Iran.

***Corresponding Author Email: mrajabioun@iau.ac.ir**

DOI: 10.71498/ijbbe.2025.1204968

ABSTRACT

Received: Apr. 25, 2025, Revised: Jul. 21, 2025, Accepted: Jul. 22, 2025, Available Online: Sep. 4, 2025

Autism is a neurological condition that influences brain function and behavior, often becoming evident in early childhood and lasting into adulthood. It is characterized by challenges in social interaction, communication, and behavior, as well as decreased attention to the surrounding environment. Early identification and diagnosis of autism can play a crucial role in addressing its impacts and enhancing social and communication abilities. Various tools, like questionnaires and neurological techniques, are used for this purpose. One such technique is electroencephalography (EEG), which records the brain's electrical activity through sensors positioned on the scalp. This paper presents a method for identifying autism using EEG data. The process starts by pinpointing active brain sources through localization techniques, followed by the application of a dual Kalman filter to assess their activity. Features are subsequently derived from EEG signals using multivariate autoregressive moving average (MVARMA) and multivariate integrated autoregressive (ARIMA) models. Principal component analysis (PCA) is employed to identify essential features, and a K-nearest neighbor (KNN) classifier is utilized to classify individuals as either autistic or neurotypical. The proposed approach achieves higher accuracy and superior classification performance compared to existing methods, highlighting its effectiveness in identifying autism.

KEYWORDS

Dual Kalman Filter, Autoregressive moving average(ARMA) model, Autoregressive integrated moving average(ARIMA) model, Autism, Electroencephalography(EEG)

I. INTRODUCTION

Autism is an intricate neurodevelopmental condition with diverse manifestations and impacts. Individuals with autism often face challenges in expressing emotions, socializing, and adapting to new situations. Common signs include difficulty speaking, limited attention to surroundings, reduced emotional expression, and challenges in facially conveying feelings. These traits are particularly noticeable in children diagnosed with autism [1-3]. The condition typically emerges in early childhood or adolescence, with many adults on the autism spectrum also experiencing epilepsy or seizures at some point. This co-occurrence underscores the need for early diagnosis, comprehensive

care, and tailored interventions for individuals with autism [4-7]. Evidence indicates a rising prevalence of autism diagnoses. A 2009 study by the Centers for Disease Control and Prevention (CDC) highlighted a consistent increase in cases. In the United States, autism prevalence rose from fewer than 3 per 10,000 children in the 1970s to over 30 per 10,000 by the 1990s. By 2012, the CDC revealed that autism was diagnosed in 1 out of every 88 children, including 1 in 54 boys. This increase highlights the critical need for early detection and intervention to enhance outcomes for individuals with autism [3, 7].

Various diagnostic methods aim to detect autism spectrum disorder (ASD) early, ensuring timely support and care. Each approach has strengths and limitations. Behavioral observation, for instance, involves closely monitoring a child's interactions, communication, and play. However, it is subject to observer bias and varying interpretations, leading to potential inconsistencies in diagnosis [8-10]. Standardized assessments such as the Autism Diagnostic Interview-Revised (ADI-R) and the Autism Diagnostic Observation Schedule (ADOS) have been developed to assess autism symptoms and severity[11, 12]. While these tools are valuable, reliance on self-reports or caregiver input can introduce biases and fail to capture the full range of behaviors. To overcome these challenges, researchers employ neuroimaging methods, such as functional magnetic resonance imaging (fMRI) and electroenc ephalography (EEG), to study brain function and connectivity in those with autism. These methods offer insights into the neural underpinnings of autism and may help identify biomarkers for diagnosis [12-15]. EEG, in particular, is a non-invasive and cost-effective method that captures the brain's electrical function through scalp electrodes. It is especially useful for studying brain rhythms and connectivity patterns associated with autism[15, 16]. EEG's ability to capture rapid changes in brain activity makes it an invaluable tool for identifying and understanding autism. By leveraging EEG data, researchers can facilitate early diagnosis, develop tailored interventions, and improve treatment outcomes.

Identifying autism through EEG signals has become a key area of interest in neuroscience, with numerous studies investigating novel approaches. Many of these studies have applied machine learning algorithms to EEG data, resulting in impressive accuracy in differentiating individuals with autism from those without the condition. [17-23]. Advanced deep learning techniques have also been suggested to extract crucial features from EEG signals, demonstrating encouraging outcomes in the identification of autism [24-27]. For example, Schwartz et al. examined specific frequency bands of EEG, identifying unique patterns associated with autism [28, 29]. Innovative methods that merge EEG analysis with graph theory, pioneered by Jurriaan and Precenzano et al., offer new insights into autism detection [30]. Tawhid et al. applied time-frequency analysis to reveal the dynamic patterns of the EEG associated with autism[31]. Additionally, Landowska integrated EEG with physiological data, such as heart rate and skin conductance, enhancing diagnostic accuracy[32]. Qaysar explored advanced signal processing methods such as wavelet transforms and independent component analysis, uncovering distinctive EEG patterns associated with autism [33]. Collectively, these methods highlight global efforts to enhance autism detection through EEG analysis, contributing to the development of more accurate diagnostic tools.

Research has also highlighted unusual patterns of connectivity in the brains of people with autism. Studies indicate heightened local connectivity and diminished long-range connections in individuals with autism[34-39]. Wass et al. discovered enhanced connectivity in frontal and short-range neural pathways, whereas Coben et al. noted increased frontal coherence and reduced coherence in posterior temporal regions[36]. Granger causality analyses revealed weakened connectivity between distant brain areas, particularly in the prefrontal cortex, anterior cingulate, and inferior parietal regions[37]. Coben et al.

further confirmed this reduced connectivity during tasks involving emotional processing[40], Similarly, Minshew and Williams reported increased frontal coherence but diminished connectivity between anterior and posterior temporal regions in autism[41]. Using dynamic causal modeling on fMRI data, Wataru Sato et al. identified decreased activity in the visual regions of the brain in children with autism [42].

This study introduces an innovative method that applies multivariate autoregressive moving average (MVARMA) and multivariate autoregressive integrated moving average (MVARIMA) models to detect autism. Key features are derived from the model parameters, highlighting the statistical properties of important ARMA and ARIMA parameters. The methodology begins with source localization to isolate active brain regions from EEG signals, then utilizes a dual Kalman filter to estimate the activities and interactions of these sources. EEG signals are mapped from sensor space to source space, where MVARMA and MVARIMA models are used to analyze these time series, incorporating past signal and source activity data. Assessing source dynamics, which represent temporal variations in brain activity, is a crucial and challenging step. Traditional methods like dynamic causal modeling (DCM) use linear or nonlinear frameworks for neural connections calculation, assuming nonlinear relationships between neural dynamics[43-45]. Moreover, dual Kalman filter methods are commonly employed to estimate dynamic source activity[46, 47]. Dual Kalman filter techniques are also employed for this purpose. For example, A.H. Omidvarnia employed dual Kalman filters on newborn EEG data[48], while Eduardo Giraldo introduced a comparable method for estimating source activity. Rajabioun et al. utilized a dual Kalman filter technique to investigate effective connectivity in EEG data from individuals with autism, revealing distinct differences between autistic and neurotypical subjects [47]. These advanced techniques demonstrate significant progress in analyzing brain dynamics and improving autism diagnosis through EEG.

II. MATERIALS AND METHODS

This study proposes a technique for distinguishing individuals with autism from neurotypical participants. This classification is crucial for halting the disorder's progression and enhancing the quality of life for affected individuals. The detailed diagram of the method is illustrated in Figure 1.

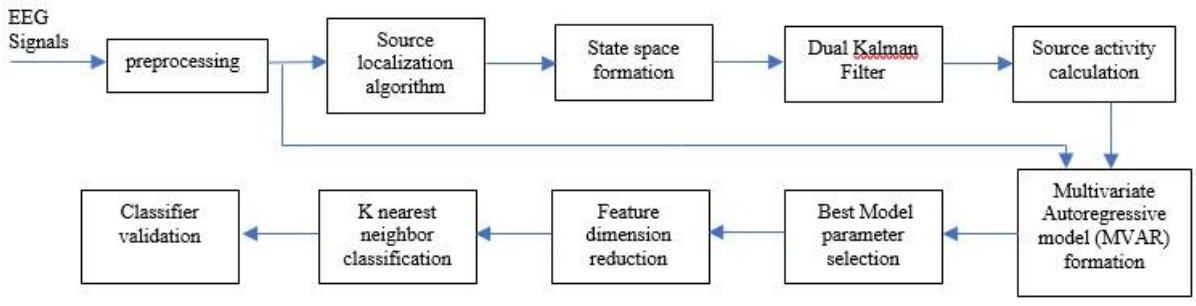

Fig. **1** The proposed method's flowchart is structured around features derived from MVAR parameters, with source activity as the input and EEG signals as the output time series.

The first step involves acquiring or preparing EEG signals. The signal that are used in this paper was sourced from a publicly available dataset [49]. The dataset comprises EEG recordings obtained with the Biosemi ActiveTwo system from 28 participants diagnosed with autism spectrum conditions and 28 neurotypical individuals, ranging in age

from 18 to 68 years. The data was collected during a 150-second resting state with eyes closed. Ethical approval for the study, including data collection and sharing, was provided by the Health Research Authority under IRAS ID 212171[49].

After preprocessing, the filtered EEG signals undergo a source localization procedure to identify and estimate the active brain regions or sources. This step simplifies the complexity of the data by selecting a finite set of active sources and mapping their spatial coordinates. The objective of source localization is to minimize a specific function, ultimately pinpointing active brain regions.

Raw EEG signals are preprocessed to remove noise and artifacts. This process begins with a bandpass Butterworth filter applied to restrict frequencies to the range of 0.5–100 Hz, reducing unwanted noise. Independent component analysis (ICA) is then performed to isolate components linked to brain activity. Non-brain-related components, such as those associated with eye blinks, electromyography (EMG), 50 Hz powerline interference, and auditory artifacts, are identified and removed, leaving a clean signal. For detailed methodologies on artifact removal and brain-component identification, refer to [50-52].

$$F = \|V_K - GJ_K\| + \alpha\|J_K\| \quad (1)$$

where $V_K(m \times 1)$ is the recorded signal recorded at the Kth sample, $J_K(3n \times 1)$ denotes the brain's source activity for the Kth sample and $G(m \times 3n)$ is the leadfield matrix, which is computed through forward problem-solving methods[53, 54]. This function is divided into two primary components: one accounts for error estimation, while the other manages noise reduction and smooths abrupt changes in source activities. The balance between these components is controlled by a parameter, α, which is determined using algorithms such as Tikhonov regularization or the L-curve method [55].

Several strategies are available to minimize Equation 1, with one widely used method being sLORETA. This approach is particularly effective due to its ability to achieve zero localization error [55, 56]. In sLORETA, the explicit solution can be obtained using the given values of G and V_K:

$$\widehat{J_K} = T.V_K \quad (2)$$

The approximated brain source activity, denoted as $\widehat{J_K}(3n \times 1)$, can be derived using the transformation matrix $T(3n \times m)$, which links the recorded EEG signals (V_K) to the estimated source activities. In sLORETA, TT is calculated as follows:

$$T = G^T H[HGG^T H + \alpha H]^+ \quad (3)$$

where $[\ ]^+$ denotes the pseudoinverse of the matrix, and HH is the regularization matrix used to ensure smoothness. HH is defined as:

$$H = I - 11^T/1^T 1 \quad (4)$$

In this equation, I denotes a unit matrix, and 1 refers to a column vector of ones with dimensions (m×1). These components are essential for selecting active regions. The source activity estimation method (Eq. 2) is applied to time-varying EEG signals to detect active brain regions. For each sample, the estimation identifies specific sources as active. Regions with the highest probability of activity across samples are selected, representing areas of significant neural engagement.

Once the active sources are identified, a model of linear variations is applied to capture their temporal dynamics. The model is expressed as:

$$J_K = F_K J_{K-1} + \eta_K \quad (5)$$

where η_K represents state noise, and F_K is the relationship matrix at the Kth sample, characterizing dependencies between active regions and their self-relation over time. The connection between these sources and the EEG signals is established through the leadfield matrix, which is calculated using forward

modeling techniques. This relationship can be summarized as follows:

$$\begin{cases} J_K = F_K J_{K-1} + \eta_K \\ V_K = G J_K + \varepsilon_K \end{cases} \quad (6)$$

Where η_K represents measurement noise. Both J_K (a source activity over time) and

F_K (spatiotemporal relationship matrix) are estimated using a dual Kalman filter, as detailed in [57, 58]. After source activity (J_K) changes calculation, a multivariate autoregressive moving average (ARMA) model is fitted to recorded signals. This model relates V_K to its past values and the estimated source activity

J, expressed as:

$$V_K = \sum_{i=1}^{p} a_i V_{K-i} + \sum_{i=0}^{q} b_i J_{K-i} \quad (7)$$

where a_i, b_i are parameter matrices, with a_i (m×p), and b_i (n×(q+1)), corresponding to the dimensions of V (m) and J (n).

To address the nonstationary nature of EEG signals, an autoregressive integrated moving average (ARIMA) model is also utilized. The ARIMA(p,d,q) model is defined as:

$$V_K = \sum_{i=1}^{p} a_i V_{K-i} + \sum_{i=0}^{q} b_i J_{K-i} + \sum_{i=1}^{d} c_i (1-Z)^d Y_i \quad (8)$$

Here, Z is the delay operator, and the difference operator is defined as:

$$(1-Z)Y_i = Y_i - Y_{i-1}$$
$$(1-Z)^2 Y_i = Y_i - 2Y_{i-1} + Y_{i-2} \quad (9)$$
$$\ldots$$

These models provide a robust framework for analyzing EEG data by leveraging both stationary and nonstationary signal characteristics, enabling more accurate assessments of brain dynamics.

In this part of the discussion, the activities from the sources act as the model's input, whereas the resultant EEG signals represent the output. The objective is to model each EEG sample by utilizing its delayed versions and the associated source activities. To accomplish this, matrices associated with the ARMA and ARIMA models—referred to as 'a', 'b', and 'c'—are calculated for every sample. The dimensions of these matrices are determined by the respective orders of the models.

Next, various characteristics are derived from these model parameters to assist with classification. To simplify the process, the parameters are divided into two distinct classes, with features extracted from each:

- **Class 1:** Parameters with low variability, indicated by a standard deviation of less than 20% of the average value. The mean values of these parameters are utilized to form the feature vectors.

- **Class 2:** Parameters that display a higher degree of variability compared to those in Class 1. For this class, the following statistical metrics are selected for the feature vector:

- Average signal value
- Standard deviation of the signal
- Signal kurtosis
- Signal skewness
- Signal entropy

Subsequently, horizontal and natural visibility graphs are created from each time series array, and several features are then extracted from them. Further details on visibility graphs can be found in [60, 62, 63]. Key features include:

- Average value of the graph nodes

• Standard deviation of the graph nodes

• Mean length of the shortest path from each node to all other nodes

After constructing the feature vectors, dimensionality reduction techniques are employed to reduce complexity and enhance classification accuracy. PCA, or principle component analysis, is employed as an effective method for reducing the dimensionality of the feature vectors. PCA converts a collection of potentially interrelated, high-dimensional features into a new set of independent variables, referred to as principal components. This process preserves the most important information from the original features while minimizing their dimensionality. PCA begins with the normalization of each feature, centering it by subtracting its mean. Next, a correlation matrix is created from these normalized features, followed by the computation of eigenvalues. The eigenvectors associated with the largest eigenvalues are then chosen to form a transformation matrix. This matrix transforms the original feature vector into a lower-dimensional space, effectively reducing its dimensions while retaining essential information.

Finally, a Support Vector Machine (SVM) is employed to classify and distinguish depressive subjects from normal individuals. SVM is chosen for its excellent performance in classifying high-dimensional feature spaces. It works by finding a hyperplane that maximizes the margin between classes, focusing on the nearest data points known as support vectors. While this is a brief overview, more detailed information on SVM mechanisms and optimization techniques can be found in the relevant literature. SVM is a widely used classifier, renowned for its robustness in managing complex classification tasks.

III. Simulation and Results

This part describes the application of the suggested approach to EEG data obtained from both individuals with autism and neurotypical participants. The procedure involved multiple stages, starting with the retrieval and recording of EEG signals from a reliable source. Next, the signals underwent preprocessing, which included the application of a bandpass filter designed to retain frequencies within the range of 0.5 to 30 Hz. Following this, ICA is applied to the signals to extract independent components, aiming to remove those unrelated to brain function, like blinking, EMG or ECG interference, 50Hz noise, and auditory brain responses. Detailed descriptions of the methods used to identify and remove these artifacts can be found in [50-52]. After preprocessing, the signals were processed using sLORETA(standardized low-resolution electromagnetic tomography) to extract the underlying brain sources with zero localization error [55, 56]. The regularization parameter for sLORETA was established through the use of the Tikhonov regularization technique [54]. Afterward, active sources were identified during the EEG recording process, and the most significant ones were selected based on their overall performance throughout the dataset. The number of EEG channels determined the selection of sources, after which a multivariate autoregressive (MVAR) model was applied to examine the identified active sources. This process led to the development of a state-space model that captures the interactions between the EEG channels and these sources. A dual Kalman filter was employed to simultaneously estimate dynamic source activity and compute the relationship matrix. Additionally, an autoregressive moving average (ARMA) or autoregressive integrated moving average (ARIMA) model was utilized to establish a connection between the source activity as input and the EEG channel recordings as output. Following this, statistical and graph-based features were extracted from the parameters estimated by the ARMA or ARIMA model. Principal Component Analysis (PCA) was then applied to reduce the dimensionality of these features, compressing the feature vector to 15 components. In the final step, a Support Vector Machine (SVM) was trained using the reduced feature set, allowing for classification based on the SVM model. To assess the classification performance, multiple simulations were carried out to examine the impact of different

parameter variations. Additionally, various performance metrics were defined to validate the classification outcomes.

$$Accurency = \frac{TP+TN}{TP+TN+FP+FN}$$ (Eq. 10)

$$sensitivity = \frac{TP}{TP+FN}$$ (Eq. 11)

$$specificity = \frac{TN}{TN+FP}$$ (12)

Firstly, the classification was conducted by altering the ARMA model's order. Different orders of models were tested for both the ARMA and ARIMA models (as described in Equation 7), and the results for each configuration are presented in Table 1.

Table 1. The proposed method evaluated the accuracy, sensitivity, and specificity of EEG classification between autistic and control groups, utilizing different orders of the ARMA and ARIMA models.

	ARMA(2,2)	ARMA(4,2)	ARMA(4,3)	ARMA(5,4)	ARMA(6,5)
Accuracy	0.9107	0.9286	0.9464	0.9821	0.9464
Sensitivity	0.9286	0.9643	0.9643	1	0.9643
Specificity	0.8929	0.8929	0.9286	0.9643	0.9286
	ARIMA(2,1,2)	ARIMA(4,2,2)	ARIMA(4,2,3)	ARIMA(4,3,4)	ARIMA(6,4,5)
Accuracy	0.9286	0.9821	0.9821	1	0.9464
Sensitivity	0.9643	0.9643	1	1	0.9643
Specificity	0.9286	0.9286	0.9643	1	0.9286

The data presented in Table 1 show that the ARMA(5,4) model exceeds the performance of all other models. Previous research has suggested several methods for determining model order, one of which is the Akaike Information Criterion (AIC) approach[59, 60]. By applying this method, the optimal ARMA model order was identified as ARMA(5,5), which closely resembles the ARMA(5,4) model that demonstrated superior performance in this study. For the ARIMA model, both ARIMA(4,2,3) and ARIMA(4,3,4) provided superior results compared to the other configurations. This indicates that the ARIMA model delivers more accurate results than the ARMA model when using the same order, highlighting its advantage in handling nonstationary signals due to the inclusion of differencing operations.

In the second simulation, the effect of two feature types is analyzed. First, classification is performed using only statistical features, followed by classification using features extracted from visibility graphs. Next, classification is performed by combining both statistical and visibility graph features. Figure 2 displays the classification accuracies for the models ARMA(4,3), ARMA(5,4), ARIMA(4,2,3), and ARIMA(4,3,4).

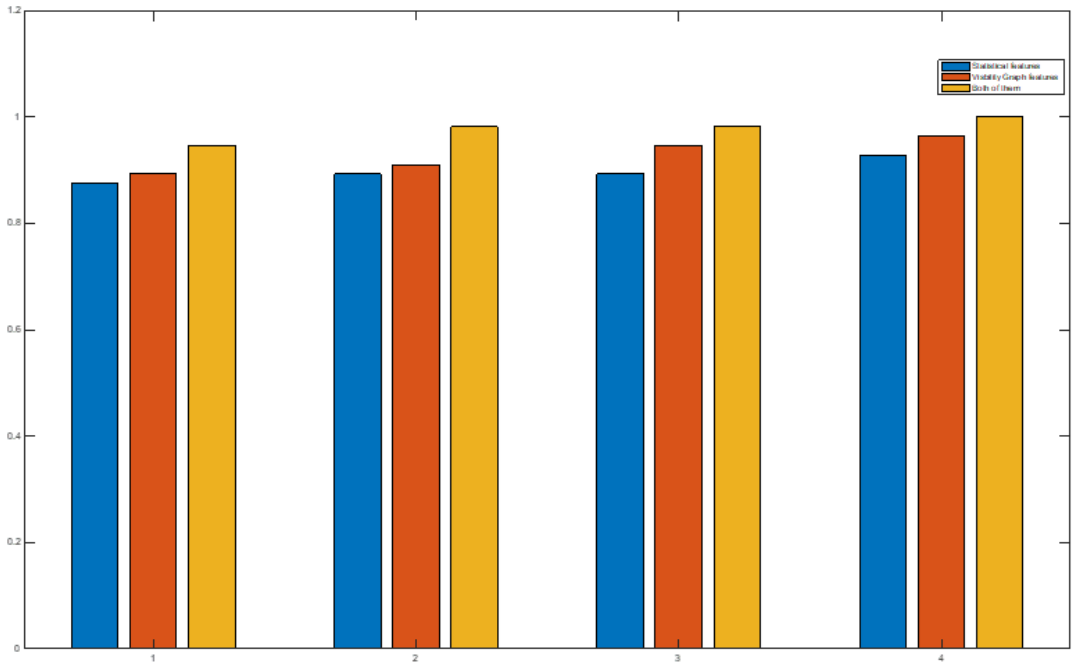

Fig. **2** The classification accuracy using the proposed method is evaluated based on different feature sets (statistical, visibility graph, and a combination of both). The classification is performed using various models, including ARMA(4,3), ARMA(5,4), ARIMA(4,2,3), and ARIMA(4,3,4).

In the second simulation, classifiers that were trained with features derived from visibility graphs showed higher accuracy compared to those trained solely with statistical features. This enhancement can be credited to the additional structural information captured by visibility graphs. As seen in Figure 2, the ARIMA(4,3,4) model outperforms other models, such as ARMA(4,3), ARMA(5,4), and ARIMA(4,2,3), highlighting its ability to better capture the inherent patterns and dynamics within the data, resulting in improved classification accuracy.

In the third simulation, the impact of decreasing the feature count through PCA is explored. While the previous simulations reduced the feature set to 15, this simulation evaluates various feature set sizes (5, 10, 15, 20, 30, and 50) and examines the corresponding classification accuracy and simulation time. Table 2 presents the results of this simulation, which was conducted using the ARMA(5,4) and ARIMA(4,3,4) models.

Table **2**. The results show the accuracy and simulation time of the proposed method with different numbers of features reduced by PCA, using the ARMA(5,4) and ARIMA(4,3,4) models.

	5	10	15	20	30	50
Accuracy (ARMA(5,4))	0.8929	0.9464	0.9821	0.9821	1	1
Simulation time (ARMA(5,4)) In sec	762	983	1463	2873	3182	8982
Accuracy (ARMA(5,4))	0.9286	0.9821	1	1	1	1
Simulation time (ARIMA(4,3,4)) In sec	1282	1676	3593	4282	7083	10012

The findings in Table 2 indicate that a larger feature set for SVM training enhances accuracy but also extends the simulation time, highlighting an increased computational burden. Notably, after selecting 15 features, further increases in the number of features do not yield significant improvements in accuracy, though the computational cost keeps increasing. Thus, it is recommended to strategically determine the reduced feature count through PCA, with 15 features providing an optimal balance between computational efficiency and accuracy.

Lastly, the performance of the proposed method was compared to other methods used for recognizing autistic individuals. The proposed method, along with approaches from previous studies, was tested on the same dataset, and their classification accuracies are shown in Table 3.

Table **3**. Comparison of Classification Accuracy for Autism Recognition Using Various Methods from Previous Studies

	Method No.1(48)	Method No.2 (20)	Method No.3(24)	Method No.4 (32)	Proposed method ARMA(5,4)	Proposed method ARIMA(4,3,4)
Accuracy	0.8929	0.9464	0.9464	0.9643	0.9821	1

The results from Table 3 show that the method which are proposed by this paper outperforms other methods in terms of classification accuracy. Specifically, using ARIMA(4,3,4) improves the classification performance. However, it is essential to recognize that this method demands more computational time than the ARMA(5,4) approach. ARMA models are typically favored when minimizing simulation time is a priority.

IV. Discussion

This research introduces an innovative approach to identifying individuals with autism by utilizing EEG signals and features extracted from multivariate autoregressive moving average (MVARMA) and multivariate integrated autoregressive (ARIMA) models. The approach consists of multiple essential steps, including source localization, source activity estimation using a dual Kalman filter, and parameter computation through MVARMA and ARIMA models. PCA is employed to identify key parameters, followed by classification using a K-nearest neighbor (KNN) classifier. The findings highlight improved classification accuracy over other methods, underscoring the effectiveness of this approach. The main objective is to use EEG signals to differentiate autistic participants from neurotypical individuals by estimating source activities and capturing the altered dynamics and connectivity between brain sources linked to autism.

To evaluate the effectiveness of the method, a series of simulations was performed to examine the effects of various parameter adjustments. The results presented in Table 1 demonstrate that the ARMA(5,4) and ARIMA(4,3,4) models performed better than other configurations, with the Akaike method suggesting that the ARMA(5,5) model is comparable to the superior ARMA(5,4) model. In the case of the ARIMA model, both ARIMA(4,2,3) and ARIMA(4,3,4) showed improved performance, emphasizing the benefit of ARIMA in handling nonstationary signals through its differencing process.

Additional simulations examined the effect of various features on classification accuracy, revealing that features derived from high visibility graphs (HVG) and non-visible graphs (NVG) play a crucial role in enhancing the results. Combining these graph-based features with statistical features led to better

performance. As numerous features increased computational load, PCA was used for feature dimensionality reduction. The findings suggested that reducing features improves accuracy but increases computation time, necessitating an optimal trade-off between computational efficiency and accuracy.

Finally, the method's performance was compared with other approaches, demonstrating that ARIMA(4,3,4) offers superior results. In conclusion, this research introduces a robust approach for identifying autism using EEG signals and features extracted from MVARMA/ARIMA models. The approach shows promise for gaining deeper insights into brain dynamics and connectivity associated with autism, through analysis of parameter variations and feature selection.

V. Conclusion

This study addresses autism spectrum disorder, a multifaceted condition impacting people across their lifespan, characterized by unique patterns of interaction, behavior, and communication, coupled with limited attention to external stimuli. Early detection is essential for intervention and enhancing interpersonal and communicative abilities. There are several techniques available for identifying autism, with one being EEG (electroencephalogram), which monitors electrical brain activity through sensors placed on the scalp. EEG signals offer valuable insights into brain activity, helping to explore the neurological processes associated with autism. Our approach estimates the activity of brain sources and analyzes the connectivity between regions to uncover patterns and dynamics unique to autism.

We present a method that leverages EEG signals and features extracted from MVARMA (Multivariate Autoregressive Moving Average) and ARIMA (Autoregressive Integrated Moving Average) models for autism classification. These models effectively capture dependencies in the data, statistical traits, and the nonstationarity often observed in brain activity associated with autism. Our method outperforms existing alternatives by accurately distinguishing autistic individuals from neurotypical participants. The method involves several essential stages: preprocessing the signals, localizing sources, modeling, extracting features, and performing classification. Through simulations and adjustments to parameters, we determine the ideal model configurations and features that optimize classification performance.

The study emphasizes the significance of comprehending brain source dynamics and connectivity in relation to autism. By analyzing recorded signals and applying MVARMA and ARIMA models, the study uncovers brain activity patterns in individuals with autism. PCA is used for feature reduction, which enhances computational efficiency while preserving accuracy. Selecting between ARIMA and ARMA models requires a trade-off between accuracy and simulation duration, with ARMA models being better suited for quicker simulations.

In summary, this research introduces a powerful approach for accurate autism identification through EEG data, which can support early diagnosis and therapeutic measures. Future studies involving larger and more varied datasets will strengthen the method's reliability and broaden its applicability. Investigating the method's applicability to various demographic groups and age ranges is crucial. Advances in EEG technology offer the potential to enhance autism detection, paving the way for tailored interventions and improved outcomes for those affected by the condition.

Reference

[1] A. Jack and J. P. Morris, "Neocerebellar contributions to social perception in adolescents with autism spectrum disorder," (in eng), Dev Cogn Neurosci, vol. 10, pp. 77-92, 2014.

[2] J. Grèzes, B. Wicker, S. Berthoz, and B. de Gelder, "A failure to grasp the affective meaning of actions in autism spectrum disorder subjects," Neuropsychologia, vol. 47, no. 8, pp. 1816-1825, 2009.

[3] W. Sato, M. Toichi, S. Uono, and T. Kochiyama, "Impaired social brain network for

processing dynamic facial expressions in autism spectrum disorders," (in eng), BMC Neurosci, vol. 13, p. 99, 2012.

[4] P. Shih, M. Shen, B. Ottl, B. Keehn, M. S. Gaffrey, and R. A. Müller, "Atypical network connectivity for imitation in autism spectrum disorder," (in eng), Neuropsychologia, vol. 48, no. 10, pp. 2931-2939, 2010.

[5] I. Mohammad-Rezazadeh, J. Frohlich, S. K. Loo, and S. S. Jeste, "Brain connectivity in autism spectrum disorder," (in eng), Curr Opin Neurol, vol. 29, no. 2, pp. 137-47, 2016.

[6] X. Yang, N. Zhang, and P. Schrader, "A study of brain networks for autism spectrum disorder classification using resting-state functional connectivity," Machine Learning with Applications, vol. 8, pp. 100290, 2022.

[7] M. K. Belmonte, G. Allen, A. Beckel-Mitchener, L. M. Boulanger, R. A. Carper, and S. J. Webb, "Autism and abnormal development of brain connectivity," (in eng), J Neurosci, vol. 24, no. 42, pp. 9228-9231, 2004.

[8] N. Bauminger-Zviely and A. Shefer, "Naturalistic evaluation of preschoolers' spontaneous interactions: The Autism Peer Interaction Observation Scale," (in eng), Autism, vol. 25, no. 6, pp. 1520-1535, 2021.

[9] J. Richer, "The social-avoidance behaviour of autistic children," Animal Behaviour, vol. 24, no. 4, pp. 898-906, 1976.

[10] P. Wei, D. Ahmedt-Aristizabal, H. Gammulle, S. Denman, and M. A. Armin, "Vision-based activity recognition in children with autism-related behaviors," Heliyon, vol. 9, no. 6, pp. e16763, 2023.

[11] T. Sappok et al., "Diagnosing autism in a clinical sample of adults with intellectual disabilities: How useful are the ADOS and the ADI-R?," Research in Developmental Disabilities, vol. 34, no. 5, pp. 1642-1655, 2013.

[12] C. Lord and R. Luyster, "Early diagnosis of children with autism spectrum disorders," Clinical Neuroscience Research, vol. 6, no. 3, pp. 189-194, 2006.

[13] M. Baygin et al., "Automated ASD detection using hybrid deep lightweight features extracted from EEG signals," Computers in Biology and Medicine, vol. 134, pp. 104548, 2021.

[14] S. N. Seyed Fakhari, F. Ghaderi, M. Tehrani-Doost, and N. Moghadam Charkari, "EEG-based brain connectivity analysis in autism spectrum disorder: Unraveling the effects of bumetanide treatment," Biomedical Signal Processing and Control, vol. 86, pp. 105054, 2023.

[15] E. L. Juarez-Martinez et al. "Prediction of Behavioral Improvement Through Resting-State Electroencephalography and Clinical Severity in a Randomized Controlled Trial Testing Bumetanide in Autism Spectrum Disorder," Biological Psychiatry: Cognitive Neuroscience and Neuroimaging, vol. 8, no. 3, pp. 251-261, 2023.

[16] W. J. Bosl, H. Tager-Flusberg, and C. A. Nelson, "EEG Analytics for Early Detection of Autism Spectrum Disorder: A data-driven approach," Scientific Reports, vol. 8, no. 1, pp. 6828, 2018.

[17] S. Peketi and S. B. Dhok, "Machine Learning Enabled P300 Classifier for Autism Spectrum Disorder Using Adaptive Signal Decomposition," (in eng), Brain Sci, vol. 13, no. 2, 2023.

[18] S. Raj and S. Masood, "Analysis and Detection of Autism Spectrum Disorder Using Machine Learning Techniques," Procedia Computer Science, vol. 167, pp. 994-1004, 2020.

[19] D. D. Khudhur and S. D. Khudhur, "The classification of autism spectrum disorder by machine learning methods on multiple datasets for four age groups," Measurement: Sensors, vol. 27, pp. 100774, 2023.

[20] B. Ari, N. Sobahi, Ö. F. Alçin, A. Sengur, and U. R. Acharya, "Accurate detection of autism using Douglas-Peucker algorithm, sparse coding based feature mapping and convolutional neural network techniques with EEG signals," Computers in Biology and Medicine, vol. 143, pp. 105311, 2022.

[21] A. R. Aslam and M. A. B. Altaf, "Chapter 14 - Machine learning–based patient-specific processor for the early intervention in autistic children through emotion detection," in Neural Engineering Techniques for Autism Spectrum Disorder, A. S. El-Baz and J. S. Suri Eds.: Academic Press, 2021, pp. 287-313.

[22] S. Parui, D. Samanta, N. Chakravorty, U. Ghosh, and J. J. P. C. Rodrigues, "Artificial intelligence and sensor-based autism spectrum

disorder diagnosis using brain connectivity analysis," Computers and Electrical Engineering, vol. 108, pp. 108720, 2023.

[23] J. Strzelecka, "Electroencephalographic studies in children with autism spectrum disorders," Research in Autism Spectrum Disorders, vol. 8, no. 3, pp. 317-323, 2014.

[24] A. S. Mohanty, P. Parida, and K. C. Patra, "ASD classification for children using deep neural network," Global Transitions Proceedings, vol. 2, no. 2, pp. 461-466, 2021.

[25] L. Xu et al., "Characterizing autism spectrum disorder by deep learning spontaneous brain activity from functional near-infrared spectroscopy," Journal of Neuroscience Methods, vol. 331, pp. 108538, 2020.

[26] C. Li, T. Zhang, and J. Li, "Identifying autism spectrum disorder in resting-state fNIRS signals based on multiscale entropy and a two-branch deep learning network," Journal of Neuroscience Methods, vol. 383, pp. 109732, 2023.

[27] T. M. Epalle, Y. Song, Z. Liu, and H. Lu, "Multi-atlas classification of autism spectrum disorder with hinge loss trained deep architectures: ABIDE I results," Applied Soft Computing, vol. 107, pp. 107375, 2021.

[28] S. Schwartz, R. Kessler, T. Gaughan, and A. W. Buckley, "Electroencephalogram Coherence Patterns in Autism: An Updated Review," (in eng), Pediatr Neurol, vol. 67, pp. 7-22, 2017.

[29] F. Precenzano et al. "Electroencephalographic Abnormalities in Autism Spectrum Disorder: Characteristics and Therapeutic Implications," (in eng), Medicina (Kaunas), vol. 56, no. 9, 19 2020.

[30] J. M. Peters et al., "Brain functional networks in syndromic and non-syndromic autism: a graph theoretical study of EEG connectivity," BMC Medicine, vol. 11, no. 1, pp. 54, 2013.

[31] M. N. A. Tawhid, S. Siuly, and H. Wang, "Diagnosis of autism spectrum disorder from EEG using a time–frequency spectrogram image-based approach," Electronics Letters, vol. 56, no. 25, pp. 1372-1375, 2020.

[32] A. Landowska et al., "Automatic Emotion Recognition in Children with Autism: A Systematic Literature Review," Sensors, vol. 22, no. 4, pp. 1649, 2022.

[33] Q. Mohi-Ud-Din and A. K. Jayanthy, "WITHDRAWN: EEG feature extraction using wavelet transform for classifying autism spectrum disorder," Materials Today: Proceedings, 2021.

[34] L. Cornew, T. P. Roberts, L. Blaskey, and J. C. Edgar, "Resting-state oscillatory activity in autism spectrum disorders," (in eng), J Autism Dev Disord, vol. 42, no. 9, pp. 1884-1894, 2012.

[35] J. R. Isler, K. M. Martien, P. G. Grieve, R. I. Stark, and M. R. Herbert, "Reduced functional connectivity in visual evoked potentials in children with autism spectrum disorder," (in eng), Clin Neurophysiol, vol. 121, no. 12, pp. 2035-2043, 2010.

[36] S. Wass, "Distortions and disconnections: disrupted brain connectivity in autism," (in eng), Brain Cogn, vol. 75, no. 1, pp. 18-28, 2011.

[37] M. E. Vissers, M. X. Cohen, and H. M. Geurts, "Brain connectivity and high functioning autism: a promising path of research that needs refined models, methodological convergence, and stronger behavioral links," (in eng), Neurosci Biobehav Rev, vol. 36, no. 1, pp. 604-25, 2012.

[38] P. Barttfeld et al. "State-dependent changes of connectivity patterns and functional brain network topology in autism spectrum disorder," (in eng), Neuropsychologia, vol. 50, no. 14, pp. 3653-3662, 2012.

[39] L. Q. Uddin, K. Supekar, and V. Menon, "Reconceptualizing functional brain connectivity in autism from a developmental perspective," (in eng), Front Hum Neurosci, vol. 7, pp. 458, 2013.

[40] R. Coben, I. Mohammad-Rezazadeh, and R. L. Cannon, "Using quantitative and analytic EEG methods in the understanding of connectivity in autism spectrum disorders: a theory of mixed over- and under-connectivity," (in eng), Front Hum Neurosci, vol. 8, pp. 45, 2014.

[41] N. J. Minshew and D. L. Williams, "The new neurobiology of autism: cortex, connectivity, and neuronal organization," (in eng), Arch Neurol, vol. 64, no. 7, pp. 945-50, 2007.

[42] W. Sato, M. Toichi, S. Uono, and T. Kochiyama, "Impaired social brain network for processing dynamic facial expressions in

autism spectrum disorders," BMC Neuroscience, vol. 13, no. 1, pp. 99, 2012.

[43] E. A. Aponte, S. Raman, B. Sengupta, W. D. Penny, K. E. Stephan, and J. Heinzle, "mpdcm: A toolbox for massively parallel dynamic causal modeling," (in eng), J Neurosci Methods, vol. 257, pp. 7-16, 15 2016.

[44] J. Nováková, M. Hromčík, and R. Jech, "Dynamic Causal Modeling and subspace identification methods," Biomedical Signal Processing and Control, vol. 7, no. 4, pp. 365-370, 2012.https://doi.org/10.1016/j.bspc.2011.07.002.

[45] M. Pyka, D. Heider, S. Hauke, T. Kircher, and A. Jansen, "Dynamic causal modeling with genetic algorithms," Journal of Neuroscience Methods, vol. 194, no. 2, pp. 402-406, 2011.

[46] M. Rajabioun, A. M. Nasrabadi, and M. B. Shamsollahi, "Estimation of effective brain connectivity with dual Kalman filter and EEG source localization methods," (in eng), Australas Phys Eng Sci Med, vol. 40, no. 3, pp. 675-686, 2017.

[47] M. Rajabioun, A. Motie Nasrabadi, M. B. Shamsollahi, and R. Coben, "Effective brain connectivity estimation between active brain regions in autism using the dual Kalman-based method," (in eng), Biomed Tech (Berl), vol. 65, no. 1, pp. 23-32, 28 2020.

[48] A. H. Omidvarnia, M. Mesbah, M. S. Khlif, J. M. O'Toole, P. B. Colditz, and B. Boashash, "Kalman filter-based time-varying cortical connectivity analysis of newborn EEG," (in eng), Annu Int Conf IEEE Eng Med Biol Soc, vol. 2011, pp. 1423-1426, 2011.

[49] E. Milne, *EEG Data for Electrophysiological signatures of brain aging in autism spectrum disorder* ed, The University of Sheffield, 2021.

[50] S. Makeig and J. Onton, *ERP features and EEG dynamics: An ICA perspective*, The Oxford Handbook of Event-Related Potential Components, 2012.

[51] J. Onton and S. Makeig, "Information-based modeling of event-related brain dynamics," (in eng), Prog Brain Res, vol. 159, pp. 99-120, 2006.

[52] A. Delorme and S. Makeig, "EEGLAB: an open source toolbox for analysis of single-trial EEG dynamics including independent component analysis," (in eng), J Neurosci Methods, vol. 134, no. 1, pp. 9-21, 2004.

[53] K. A. Awada, D. R. Jackson, J. T. Williams, D. R. Wilton, S. B. Baumann, and A. C. Papanicolaou, "Computational aspects of finite element modeling in EEG source localization," IEEE Transactions on Biomedical Engineering, vol. 44, no. 8, pp. 736-752, 1997.

[54] H. Hallez et al., "Review on solving the forward problem in EEG source analysis," Journal of NeuroEngineering and Rehabilitation, vol. 4, no. 1, pp.1- 46, 2007.

[55] R. Grech et al. "Review on solving the inverse problem in EEG source analysis," (in eng), J Neuroeng Rehabil, vol. 5, pp. 1- 25, 2008.

[56] M. A. Jatoi, N. Kamel, A. S. Malik, and I. Faye, "EEG based brain source localization comparison of sLORETA and eLORETA," (in eng), Australas Phys Eng Sci Med, vol. 37, no. 4, pp. 713-21, 2014.

[57] E. Wan and A. Nelson, "Neural Dual Extended Kalman Filtering: Applications In Speech Enhancement And Monaural Blind Signal Separation," Neural Networks for Signal Processing - Proceedings of the IEEE Workshop, 2000.

[58] E. A. Wan and A. T. Nelson, "Dual Extended Kalman Filter Methods," in Kalman Filtering and Neural Networks, pp. 123-173, 2001.

THIS PAGE IS INTENTIONALLY LEFT BLANK.

IJBBE International Journal of Biophotonics & Biomedical Engineering Vol. 5, No. 1, Spring-Summer, 2025

Research Article

Design and Experimental Validation of a Portable Photometer for Non-Invasive Neonatal Jaundice Assessment

M. J. Dinparvar [a] and M. Khanlari [*b]

a Department of Biomedical Engineering, NT.C., Islamic Azad University, Tehran, Iran
b Department of Biomedical Engineering, NT.C., Islamic Azad University, Tehran, Iran

***Corresponding Author Email: msmkhanlari@iau.ac.ir**

DOI: 10.71498/ijbbe.2025.1211116

ABSTRACT

Received: Jul. 5, 2025, Revised: Aug. 5, 2025, Accepted: Aug. 16, 2025, Available Online: Sep. 4, 2025

Background and Objective: Bilirubin, a yellow pigment, is a key biomarker for diagnosing and monitoring neonatal jaundice. Neonatal jaundice, caused by elevated blood bilirubin levels, can lead to severe complications if not detected and treated in time. Traditional methods for bilirubin measurement, although accurate, are invasive and require laboratory equipment, causing discomfort for the infant and increasing costs. This study presents the design and evaluation of a portable photometer for accurate non-invasive bilirubin measurement.

Methods:
The proposed device utilizes blue light at a wavelength of 470 nm to determine bilirubin concentration based on reflected light from simulated skin surfaces. The system incorporates multiple optical filters and advanced calibration algorithms to minimize errors caused by environmental and physical factors such as ambient light, temperature, and skin tone variations.

Results:
Experimental tests on skin phantoms with various bilirubin concentrations demonstrated the device's high accuracy in measuring bilirubin across a range of conditions, including light, medium, and dark skin tones.

Conclusion:
The results indicate that portable photometers can serve as rapid, accurate, and user-friendly tools in clinical and medical settings, particularly in environments with limited access to laboratory facilities.

KEYWORDS

Neonates Jaundice, Photometery, Transcutaneous Bilirubin

I. Introduction

Bilirubin is a yellow pigment generated during the breakdown of hemoglobin. Elevated levels of this pigment in the blood lead to jaundice, a common physiological condition particularly prevalent in newborns [1, 2]. It is observed in approximately 60% of full-term and up to 80% of preterm neonates and is primarily due to accelerated hemoglobin turnover and the temporary immaturity of the liver's bilirubin clearance mechanism. If not diagnosed and treated promptly, neonatal jaundice may result in irreversible neurological complications [3].

The conventional method for diagnosing jaundice is based on measuring the total serum bilirubin (TSB) through blood sampling. Although this method provides high accuracy, it is invasive and may cause discomfort or even anemia in newborns [4, 5]. Furthermore, it requires laboratory equipment and is both time-consuming and expensive. As a result, non-invasive techniques such as transcutaneous bilirubinometry (TcB) have been developed in recent years as effective alternatives to blood-based methods [6, 7].

Photometry is one such non-invasive method for estimating bilirubin concentration based on its selective absorption of light at specific wavelengths, particularly in the blue spectrum.

Photometric devices illuminate the skin and analyze the reflected light using calibration algorithms to estimate bilirubin concentration [8–10]. Bilirubin exhibits a distinct absorption peak in the 450–490 nm range [11, 12], which enables the design of simple and cost-effective optical diagnostic tools. Fig. 1 illustrates the absorption spectra of various tissue components, including hemoglobin, melanin, water, and bilirubin [13, 19].

In this study, a portable photometric device was designed and evaluated to provide a simple, rapid, and cost-effective solution for the initial screening of neonatal jaundice. This research is categorized as applied and is intended for use in clinical settings with limited access to laboratory infrastructure.

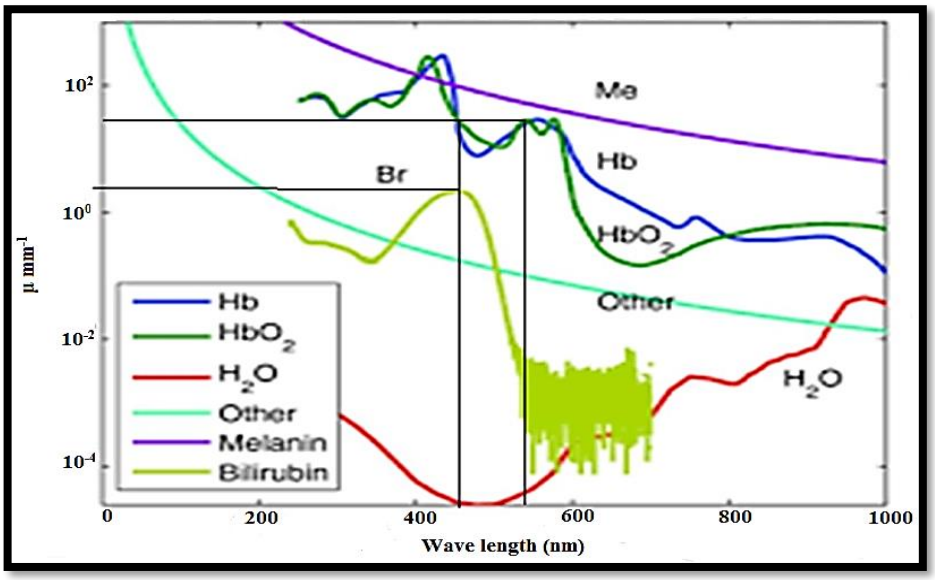

Fig. **1** Representative Absorption Spectra of Blood Constituents [13, 19]

Transcutaneous bilirubin measurement has emerged as a simple and non-invasive alternative to traditional invasive methods. By eliminating the need for blood sampling, it enables early screening and facilitates timely diagnosis and treatment.[10]

In recent years, numerous studies have focused on the development and enhancement of photometric devices for neonatal jaundice detection. These devices leverage modern optical technologies to deliver reliable and consistent non-invasive bilirubin measurements [11–14]. Techniques such as diffuse reflectance spectroscopy (DRS) analyze light reflected from the skin to estimate bilirubin concentration, even in turbid samples [11]. Furthermore, photon diffusion theory-based models have improved the accuracy of TcB methods by simulating light propagation in neonatal skin.[12]

The design of portable, handheld systems capable of simultaneously measuring bilirubin and hemoglobin represents a major step toward the clinical translation of such technologies. These devices enhance accessibility and enable rapid monitoring in both hospital and home settings.[13]

Comparative studies between TcB and the gold standard TSB have shown that optical methods exhibit acceptable accuracy and strong correlation with serum values, making them reliable tools for initial screening and treatment monitoring [14]. Moreover, computational and machine learning models have been employed to analyze neonatal data for the prediction of jaundice severity and therapy planning.[16 ,15]

Various phototherapy systems have also been developed using different illumination techniques, including photometry and spectrophotometry, to reduce serum bilirubin levels in affected neonates [17]. These innovations highlight the increasing potential of optical technologies in both diagnosis and treatment.

Given the limitations of traditional methods and the advantages of photometric approaches, developing portable and efficient devices for transcutaneous bilirubin estimation is a promising direction in neonatal care. In this study, we present the design and evaluation of a portable photometric device aimed at providing an accurate, rapid, and user-friendly solution for neonatal jaundice screening and follow-up.

II. Materials and Methods

A. *Preparation of Skin-Mimicking Phantoms*

To evaluate the accuracy of the bilirubin measurement device under laboratory-simulated conditions, gelatin-based optical phantoms were fabricated to mimic the optical properties of human skin. These phantoms replicate light absorption and scattering behavior in tissue, allowing controlled assessment of the device's response to various bilirubin concentrations. The phantom fabrication method was adapted based on previous studies on optical simulation of neonatal skin [11, 13]. To simulate bilirubin absorption, food-grade dyes with a similar spectral profile were used. This approach offers cost-effectiveness, reproducibility, and standardization across measurements. The phantoms were prepared in three categories:

(a) Control Samples:

To produce phantoms with controlled bilirubin concentrations, a 2% (w/v) gelatin solution was prepared by gradually dissolving gelatin powder into deionized water. The mixture was heated to 60°C and stirred using a magnetic stirrer to ensure homogeneity. Standard dye solutions with concentrations of 0.25, 0.3, and 0.5 mg/dL were prepared by adding 5, 7, and 10 µL of dye, respectively, to the gelatin base. After thorough mixing, the solutions were poured into sterile containers and allowed to solidify at room temperature.

(b) High-Concentration Samples:

To assess device performance at higher bilirubin levels, more concentrated dye solutions were used. Volumes of 100, 150, and 200 µL of concentrated dye were added to 2% gelatin to achieve final concentrations of 2, 3, and 4 mg/dL, respectively. The mixtures were

homogenized using a magnetic stirrer, poured into transparent molds, and left to set at room temperature for two hours until gel formation occurred (Fig. 2).

(c) Dark Skin Model Samples

To simulate the optical properties of dark skin tones more accurately, a coffee solution was used as a background light absorber. A solution with a concentration of 250 mg/dL was prepared and added to the gelatin mixture as a melanin-mimicking agent. Food-grade dye solutions with varying concentrations (as described in previous sections) were added to the coffee-infused phantoms.

To ensure uniform distribution of both the dye and the coffee particles, the mixtures were treated in an ultrasonic bath for 5 minutes. The final solutions were poured into sterile molds and allowed to solidify at room temperature, forming stable gel-based phantoms (Fig. 3).

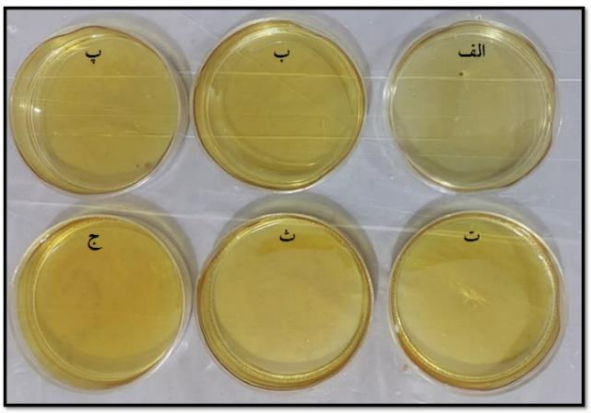

Fig. **2** Phantoms with Different Bilirubin Concentrations. (a) 0.25, (b) 0.3, (c) 0.5, (d) 2, (e) 3, and (f) 4 mg/dL

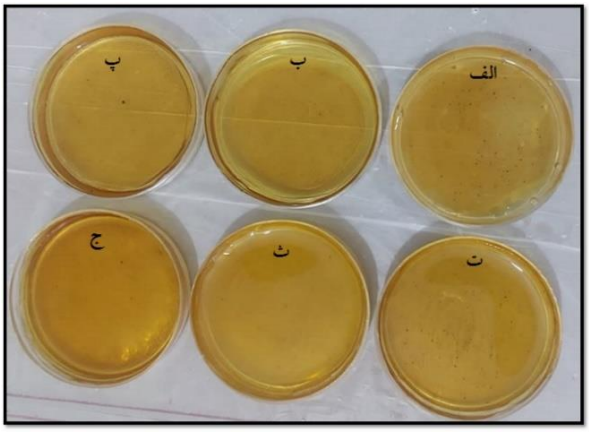

Fig. **3** Coffee-Infused Phantoms with Varying Bilirubin Concentrations. (a) 0.25, (b) 0.3, (c) 0.5, (d) 2, (e) 3, and (f) 4 mg/dL

B. *System Design*

In the proposed device, a constant current power supply was used to drive the LEDs, minimizing intensity fluctuations and ensuring stable illumination. The light emitted from the LEDs is focused using a set of precision lenses and directed onto the surface of the skin or phantom. The optical system is carefully designed to optimize beam direction and intensity while minimizing optical losses.

The lenses used are coated with anti-reflective material to enhance transmission efficiency. The emitted blue light interacts with bilirubin molecules within the skin tissue, and part of it is absorbed. The reflected or transmitted portion of the light is collected and directed toward an optical sensor.

This reflected signal contains spectral information about bilirubin concentration in the superficial skin layers, which is then analyzed by the system for estimation and display.

To ensure accurate measurement of reflected light intensity, a TSL2561 digital light sensor was employed. This sensor offers significant noise reduction as light intensity increases and provides a digital output directly to the microcontroller, eliminating the need for analog-to-digital conversion. To minimize external influences—such as light angle, device-to-skin distance, and applied pressure—a mechanical enclosure was designed with

precise dimensions. A fixed distance of 1.25 cm between the sensor and the skin surface was maintained to ensure measurement consistency. Additionally, the device was fitted with a light-blocking shield to prevent interference from ambient illumination. Fig. 4 illustrates the precise mechanical design used to maintain a fixed distance between the sensor and the skin. This structure helps reduce measurement errors caused by variations in light angle and distance.

The electronic control unit is based on an Arduino Mega 2560 board utilizing an ATmega2560 microcontroller from AVR. This board supports both I2C and SPI communication protocols. The I2C protocol was used to interface with the light sensor, while SPI was utilized for communication with the display module.

The microcontroller processes the incoming digital signals, applies noise filtering algorithms, and computes the estimated bilirubin concentration. To enhance accuracy, multiple consecutive readings under identical conditions were taken, and the average signal was calculated. The device was calibrated using standard bilirubin solutions at various concentrations, simulating real clinical levels. The processed results are displayed numerically on the device screen.

To facilitate portability and usability in clinical environments, the system is powered by a rechargeable lithium battery, which supports approximately 1,800 tests per full charge.

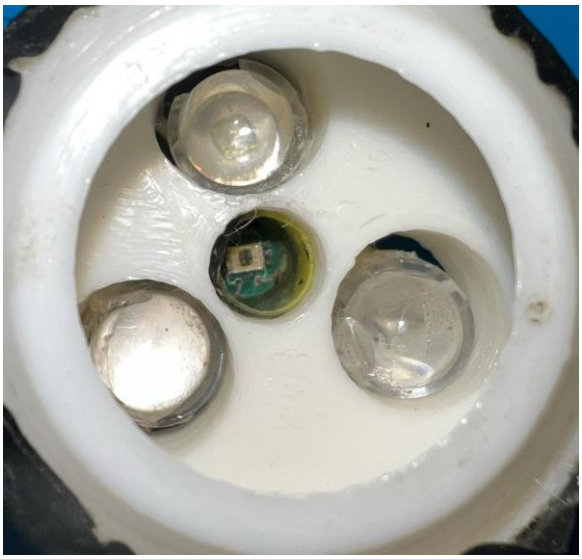

Fig. **4** Custom-Designed Mechanical Fixture for Sensor and LED Placement

III. Discussion

The engineering design of the device aimed to deliver a compact, reliable, and clinically viable solution, with final dimensions of 12 × 8 cm and a weight of 800 grams. Fig. 5 shows the final physical configuration of the fabricated device. During the design process, several critical factors were considered, including ease of use, portability, reliability across various ambient lighting and temperature conditions, and mechanical robustness. Ultimately, an optimized structural configuration was proposed to meet clinical and operational needs for use in real-world medical environments.

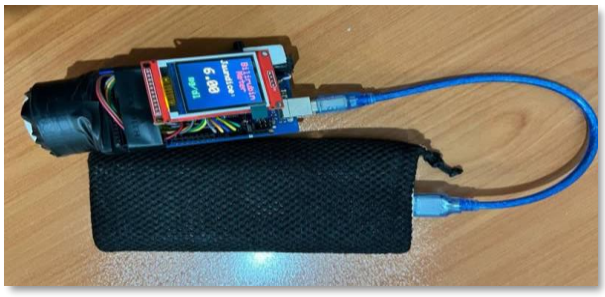

Fig. **5** Physical Structure of the Device

A. *Bilirubin Estimation*

To estimate bilirubin concentration in tissue, the Beer–Lambert law was applied—an essential principle in spectrophotometry that

describes the linear relationship between light absorbance, the concentration of an absorbing substance, and the optical path length.

This relationship is mathematically expressed as Eq. 1.

$$I(\lambda) = I_0(\lambda)F.10^{-K} \quad (1)$$

where $I_0(\lambda)$ is the intensity of the incident light at the wavelength λ, $I(\lambda)$ is the reflected light intensity measured by the sensor, K is the absorption coefficient and F is the attenuation factor that reflects light absorption and scattering within the tissue and depends on bilirubin concentration [19].

Equation 2 relates the absorption coefficient to the concentration of the absorbing substance (C), its molar absorptivity (ϵ), and the optical path length through the tissue (L). This fundamental relationship forms the basis for spectroscopic analysis in biological tissues.

$$K = \epsilon CL \quad (2)$$

In this study, reflectance measurements were taken at three different wavelengths to enhance estimation accuracy. Multi-wavelength analysis allows compensation for spectral interference caused by other chromophores present in the skin, such as hemoglobin and melanin, thereby improving specificity for bilirubin detection.

According to Fig. 1, oxyhemoglobin and bilirubin exhibit similar absorption behavior at a wavelength of 470 nm (blue light). However, bilirubin absorbs significantly less light at 530 nm (green light). By measuring light absorbance at both wavelengths and calculating their difference, the influence of oxyhemoglobin can be minimized, allowing for a more accurate estimation of bilirubin concentration [9].

Another major factor affecting light absorption at 470 nm is melanin, the primary skin pigment. Melanin exhibits relatively uniform absorption across a broad spectrum of wavelengths, particularly between 450 and 700 nm. To reduce melanin's effect on bilirubin measurement, absorption at 450 nm and 630 nm (red light) can be analyzed and computationally corrected.

As a result, utilizing three distinct wavelengths enables the attenuation of interference from both hemoglobin and melanin, thereby enhancing measurement accuracy and specificity.

In this study, the above principles were applied to analyze reflectance data from skin-mimicking phantoms at multiple wavelengths. Bilirubin concentrations were calculated using this approach, which yielded improved precision and repeatability compared to traditional single-wavelength methods. The proposed technique demonstrates potential as a reliable and non-invasive method for bilirubin quantification in biological tissues.

B. *Phantoms with Varying Bilirubin Concentrations*

In both phantom groups (with and without coffee), bilirubin concentration was adjusted at six different levels: 0.25, 0.3, 0.5, 2, 3, and 4 mg/dL. This concentration range was selected to cover clinically relevant values and to evaluate the device's accuracy across different bilirubin levels.

For each phantom sample, reflectance measurements were taken at three distinct surface locations, and three consecutive readings were recorded per location. As a result, a total of 9 reflectance values were obtained for each bilirubin concentration, providing sufficient data for statistical analysis (Fig. 6).

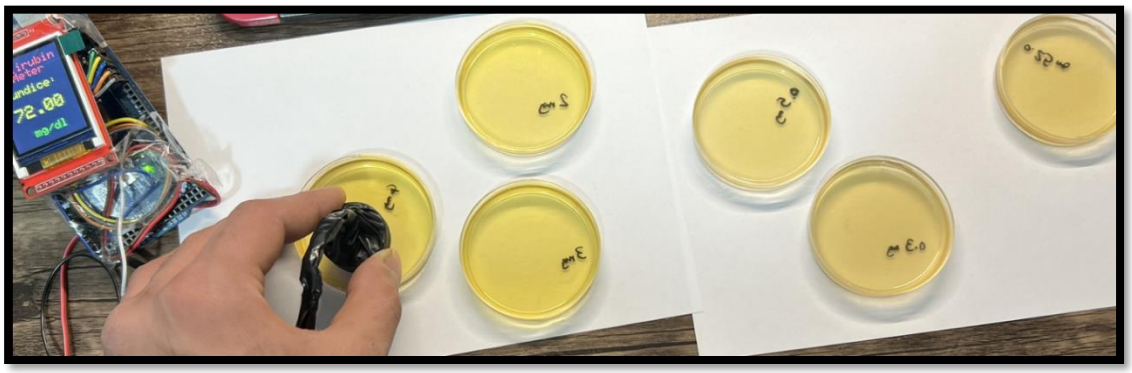

Fig. **6** Device Testing on Phantom Samples

Following data acquisition, the reflectance spectra for each sample were linearly matched against standard reference spectra of chromophores present in the phantom composition (including food dye, coffee, gelatin, and water). This spectral fitting enabled the identification of absorption contributions from each component. Subsequently, the Beer–Lambert law was applied to estimate the concentration of each chromophore, yielding high accuracy in bilirubin quantification.

The detailed measurement results are presented in Tables 1 and 2. In these Tables, "Error" shows the signed difference (±) between measured and actual values, and "Absolute Error (%)" is the absolute percentage error.

The Pearson correlation coefficient (r), which quantifies the strength and direction of a linear relationship between two variables, was calculated as 0.9997 and 0.9976 for Tables 1 and 2, respectively. These values, being very close to +1, indicate a very strong positive correlation between the actual and estimated bilirubin concentrations.

In other words, as the actual bilirubin concentration increases, the estimated concentration also increases in a nearly linear manner. This result confirms the high accuracy and reliability of the proposed method for bilirubin quantification in this study (Figs. 7 and 8).

Table **1:** Reflected Light Intensity at Different Bilirubin Concentrations in Phantoms Without Coffee

Percentage Absolute Error (%)	Error	Estimated Concentration (mg/dL)	Actual Concentration (mg/dL)	Reflected Light Intensity (a.u.)		
				Green	Blue	Red
-3.8400	-0.0096	0.2404	0.25	682	435	408
25.1667	0.0755	0.3755	0.30	680	400	396
1.7000	0.0085	0.5085	0.50	699	380	399
-3.9350	-0.0787	1.9213	2	709	170	380
-6.0000	-0.1800	2.8200	3	700	101	398
-4.1500	-0.1660	3.8340	4	500	42	390
Pearson Correlation Coefficient: $r = 0.9997$						

Table **2** Reflected Light Intensity at Different Bilirubin Concentrations in Coffee-Infused Phantoms

Percentage Absolute Error (%)	Error	Estimated Concentration (mg/dL)	Actual Concentration (mg/dL)	Reflected Light Intensity (a.u.)		
				Green	Blue	Red
-2.2000	-0.0055	0.2445	0.25	341	217	204
25.1667	0.0755	0.3755	0.30	340	200	198
27.8200	0.1391	0.6391	0.50	390	190	170
-3.8250	-0.0765	1.9235	2	355	85	190
-6.3767	-0.1913	2.8087	3	404	56	160
1.3825	0.0553	4.0553	4	388	27	188
Pearson Correlation Coefficient: $r = 0.9976$						

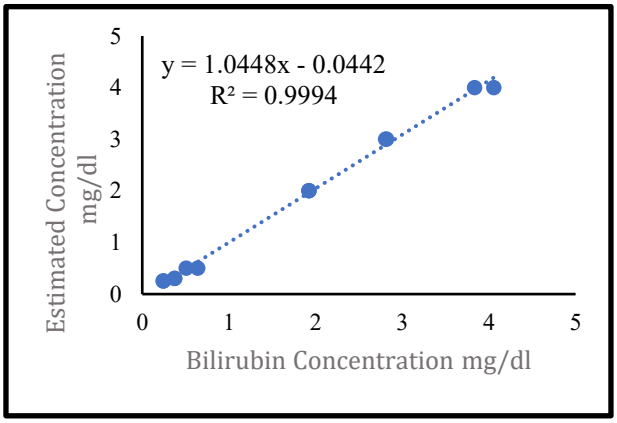

Fig. **7** Estimated Bilirubin Concentrations at Different Actual Levels in Phantoms Without Coffee

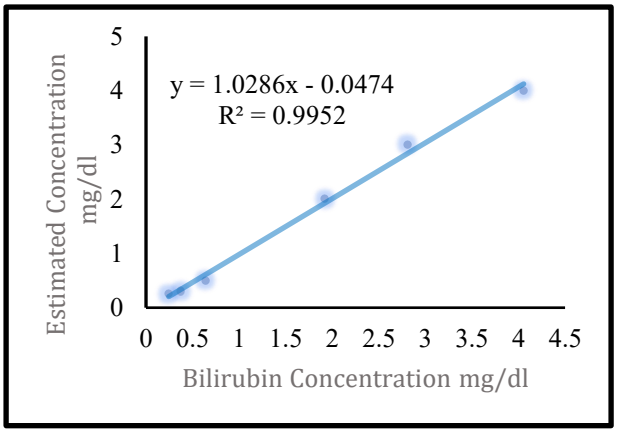

Fig. **8** – Estimated Bilirubin Concentrations at Different Actual Levels in Coffee-Infused Phantoms

In addition to the correlation coefficient, analysis of percentage error is crucial for assessing measurement accuracy. In this study, the percentage error ranged from 1.3825% to 27.8200%**.** The highest error was observed at a bilirubin concentration of 0.5 mg/dL, while the lowest error occurred at 4 mg/dL**.**

This variation in error percentage may result from several factors, including the limited sensitivity of the device at lower concentrations, human errors during measurement, or slight variations in experimental and environmental conditions**.**

IV. Analysis of Experimental Results

The present study was conducted to evaluate the accuracy and effectiveness of a non-invasive method for measuring bilirubin concentration in neonates. To assess the validity and positioning of the proposed approach, the results were compared with those reported in previous studies.

In the study by Surana et al., a Pearson correlation coefficient of 0.69 was reported between the invasive (blood test) and non-invasive (JM-103 device) methods [14], indicating a moderate correlation. Other studies reported correlation values of 0.9997, 0.88, and

0.953, respectively [11–13]. In contrast, the device developed in this study demonstrated a correlation coefficient of over 0.9976, despite its low cost (under 5 million IRR), highlighting its high potential for screening applications.

Measurements were performed based on optical principles using wavelengths directly related to bilirubin absorption. One of the key advantages of the device is its resilience to environmental interferences, such as ambient light and temperature changes. Additionally, through precise calibration and intelligent algorithms, it minimizes the effects of physical variables such as skin thickness and surface moisture.

Another notable strength is the system's ability to compensate for different skin tones. Since melanin can significantly affect light reflection and absorption, the device design incorporates multi-band optical filters and dynamic calibration to adapt to various pigmentation levels. Experimental results confirmed consistent accuracy across light, medium, and dark skin tones.

This feature is particularly important in multi-ethnic clinical environments, where measurement reliability across all patients is crucial. The higher correlation coefficients observed in this study compared to previous works reflect the superior accuracy of the proposed method. This may be attributed to several factors, including advanced hardware design, use of high-sensitivity sensors, complex signal processing algorithms, and robust calibration techniques. Additionally, differences in sample type (phantoms vs. human subjects) may partially explain the variability observed across studies. Although the gelatin-based phantoms closely mimic the optical properties of human skin, their surface is smoother than natural skin. In this study, a thin matte coating was applied to promote uniform light diffusion and minimize the impact of surface smoothness. Additionally, maintaining a fixed distance between the sensor and the sample further reduced surface-related variability

V. Conclusion

This study focused on the design and development of a portable photometric device for the non-invasive measurement of transcutaneous bilirubin levels in neonates. Leveraging advanced optical technologies and digital signal processing, the device demonstrated high accuracy and minimal error, even in the presence of environmental interferences and individual variations such as skin pigmentation.

The integration of stable light sources, precise optical filters, and an intelligent calibration system enabled reliable and repeatable results. Furthermore, the use of gelatin-based phantoms with standardized chromophores provided a suitable model for simulating human skin and assessing the device's performance under controlled laboratory conditions.

With its compact size and low weight, the device offers excellent portability and can serve as an effective tool for early jaundice detection, particularly in clinical and underserved settings. Key advantages include non-invasiveness, rapid measurement, reduced infection risk, and ease of use.

Given the critical importance of timely diagnosis and treatment of neonatal jaundice in preventing serious complications, further development of similar devices with advanced features—such as integration with intelligent systems and real-time data analysis—is highly recommended.

It is worth noting that the device is currently undergoing clinical evaluation, with initial human testing being conducted at a medical facility affiliated with Jahrom University of Medical Sciences, under approved ethical protocols.

References

[1] M. Penhaker, V. Kasik, and B. Hrvolová, “Advanced bilirubin measurement by a photometric method,” Elektronika ir Elektrotechnika, vol. 19, no. 3, pp. 47–50, 2013.

[2] T. Mulquiney and S. Dechert, "Health problems of the newborn," in Wong's Nursing Care of Infants and Children, Australia and New Zealand Edition, E-book for Professionals, 2021, p. 168.

[3] E. I. Obeagu and M. C. Katya, "A systematic review on physiological jaundice: Diagnosis and management of the affected neonates," Madonna Univ. J. Med. Health Sci., vol. 2, no. 3, pp. 25–41, 2022.

[4] C. I. Okwundu et al., "Transcutaneous bilirubinometry versus total serum bilirubin measurement for newborns," Cochrane Database Syst. Rev., no. 5, 2023.

[5] F. A. Dzulkifli, M. Y. Mashor, and K. Khalid, "Methods for determining bilirubin level in neonatal jaundice screening and monitoring: A literature review," J. Eng. Res. Educ., vol. 10, pp. 1–10, 2018.

[6] C. J. Hazarika et al., "Development of non-invasive biosensors for neonatal jaundice detection: A review," Biosensors, vol. 14, no. 5, p. 254, 2024.

[7] J. Chahl, "Non-invasive and non-contact automatic jaundice detection of infants based on random forest," Comput. Methods Biomech. Biomed. Eng. Imaging Vis., vol. 11, pp. 2516–2529, 2023.

[8] L. Zucchini et al., "Optimization of an algorithm for hemoglobin interference compensation on a simple photometer for bilirubin measurement," in Proc. IEEE Int. Symp. Med. Meas. Appl. (MeMeA), Eindhoven, Netherlands, 2024, pp. 1–6.

[9] M. Johnson, Photodetection and Measurement: Maximizing Performance in Optical Systems. New York, NY, USA: McGraw-Hill, 2003.

[10] N. Bint Ali, "ANN-based non-invasive jaundice measurement system using optical technique," M.S. thesis, Univ. Tun Hussein Onn, Malaysia, 2023.

[11] N. Y. Cheng, Y. L. Lin, M. C. Fang, W. H. Lu, C. C. Yang, and S. H. Tseng, "Noninvasive transcutaneous bilirubin assessment of neonates with hyperbilirubinemia using a photon diffusion theory-based method," Biomed. Opt. Express, vol. 10, pp. 2969–2984, 2019.

[12] Y. Y. Chen, S. Y. Tzeng, Y. L. Lin, K. Y. Chu, and S. H. Tseng, "Precisely discerning the bilirubin concentration of turbid samples using diffuse reflectance spectroscopy," Front. Opt., 2016.

[13] N. Y. Cheng, S. Y. Tzeng, M. C. Fang, C. Y. Kuo, W. H. Lu, C. C. Yang, and S. H. Tseng, "Handheld diffuse reflectance spectroscopy system for noninvasive quantification of neonatal bilirubin and hemoglobin concentrations: A pilot study," Biomed. Opt. Express, vol. 14, pp. 467–476, 2023.

[14] A. U. Surana et al., "Comparison of transcutaneous bilirubin with serum bilirubin measurements in neonates at tertiary care center in western part of India," Int. J. Contemp. Pediatr., vol. 4, no. 4, pp. 1445–1449, 2017.

[15] J. H. Chou, "Predictive models for neonatal follow-up serum bilirubin: Model development and validation," JMIR Med. Inform., vol. 8, no. 10, 2020.

[16] G. Koch et al., "Leveraging predictive pharmacometrics-based algorithms to enhance perinatal care—Application to neonatal jaundice," Front. Pharmacol., vol. 13, p. 842548, 2022.

[17] L. Zucchini et al., "A method for compensating hemoglobin interference in total serum bilirubin measurement using a simple two-wavelength reflectance photometer," Sensors, vol. 24, no. 20, p. 6749, 2024.

[18] M. Thomas et al., "Current and emerging technologies for the timely screening and diagnosis of neonatal jaundice," Crit. Rev. Clin. Lab. Sci., vol. 59, no. 5, pp. 332–352, 2022.

[19] D. F. Swinehart, "The Beer–Lambert law," J. Chem. Educ., vol. 39, no. 7, p. 333, 1962.